Small Research Project: Hydrodynamical Modelling of Spherical Gravitational Collapse

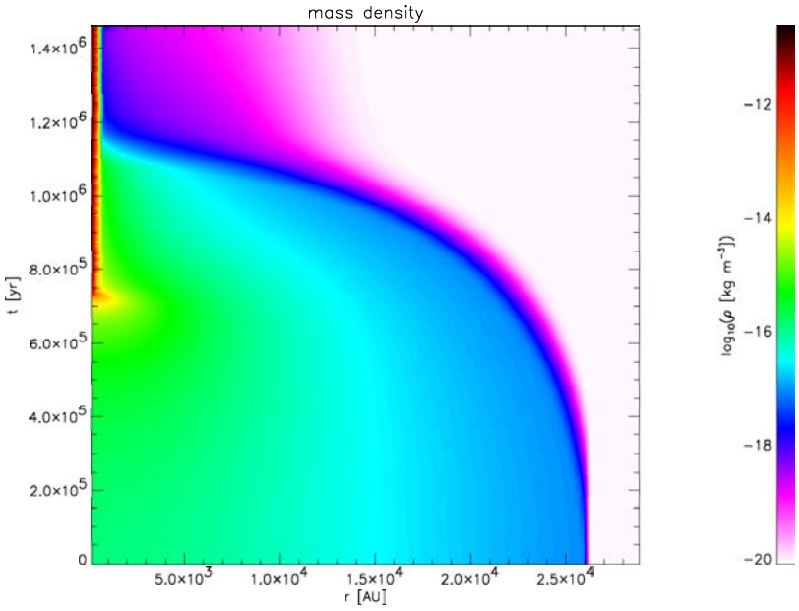

H.T. Intema, Sterrewacht Leiden, studentnr. 0035734
Supervised by Dr. G. Mellema

19th January 2004

Contents

Chapter 1

Introduction

This report is part of the small research project that was performed by the author, as student member of the Theory Group at the Sterrewacht Leiden. The project is one of two that are part of the master curriculum at Leiden University. This project was supervised by Dr. G. Mellema.

Mellema, in collaboration with Eulderink and Icke, developed a numerical solver for hydrodynamical behaviour of gas, governed by the Euler equations. This Roe solver, based on the work of Roe [13], was previously tested on a number of different test problems (see Eulderink&Mellema [4], Chapter 12 and Paardekooper [11], Chapter 5), with excellent results. Only once before, by Paardekooper, was the Roe solver used in combination with gravity, to study the interaction between a planet and a gas disk during the era of planet formation.

The aim of this small research project was to apply the Roe solver to the gravitational collapse of a spherical cloud of gas. By assuming initial spherical symmetry without rotation, the collapse can be simulated in one spatial dimension, namely the radial distance r. This reduces the needed computational power in such a way that the model can be easily run on a single PC.

1.1 Gravitational collapse

The application of the small research project was the gravitational collapse of a cloud of gas in (empty) space. Gravitational collapse is the only known mechanism that is able to create large scale structure in the universe, such as stars, galaxies or galaxy clusters. Gravitational collapse can occur when local fluctuations in gas mass density appear. For gas clouds inside a galaxy, this can be caused by shocks from supernova explosions. Areas with an overdensity, compared to the average mass density, contract under self-gravity, making the mass density contrast even larger. The contracting gas forms a cloud or breaks up in multiple smaller gas clouds. Eventually, the contraction of the gas clouds is slowed down due to the gas pressure (centrifugal forces and magnetic fields may also play an important role). Depending on the mass and the size of the contracted gas cloud, the contraction stops to form a cloud in hydrostatic (mechanic) equilibrium, or it continues into a gravitational collapse to form a very dense point mass (a star or planet).

The problem of gravitational instabilities in gas clouds was studied as early

as the start of the twentieth century by Jeans. He studied the effects of small deviations from hydrostatic equilibrium and formulated his well known Jeans criterion for gravitational stability. In the 1930's, other people like Chandrasekhar and Schwarzschild joined in, trying to find stationary solutions and approximations for the Euler equations of motion, which govern the dynamic motion of gas. This work was mainly focused on the problem of star formation and evolution.

1.2 Numerical modelling

As of the 1960's, the introduction of the computer gave scientists a tool to do extensive numerical research in the field of the dynamics of gravitational collapse and proto-star formation. Around the same time that the theory on stellar evolution advanced by the work of Hayashi and others, Larson [8] was one of the first to build a numerical model for spherical gravitational collapse of a cloud with a constant mass density distribution. In his article on proto-star formation, he found that the mass density ρ of the outer part of the collapsing cloud approaches an r^{-2} distribution (see Figure 1.1). Larson succeeded in finding

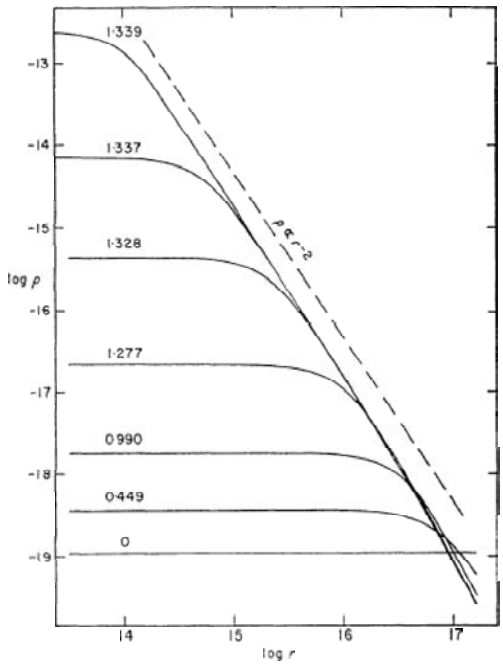

Figure 1.1: The variation with time of the density distribution in the collapsing cloud (CGS units). The curves are labelled with the times in units of 10^{13} s since the beginning of the collapse. Note that the density distribution closely approaches the form $\rho \propto r^{-2}$. (From Larson [8], Figure 1.)

analytical, self-similar solutions to the isothermal Euler equations, in hope to give a mathemathical description of the gas state during gravitational collapse.

Shu [14], Hunter [7] and later Boily&Lynden-Bell [2] extended these solutions, but in general, these solutions only partially match numerical simulations.

Numerical simulations of gravitational collapse were performed by several authors, including Shu [14], Hunter [7] and Foster&Chevalier [6] (see Figure 1.2), for isothermal spheres close to hydrostatic equilibrium. The results did not differ much from the results of Larson, suggesting that the details of the initial setup have a limited impact on the details of the collapse itself. In this sense, the total mass of the cloud, expressed in Jeans masses, seems to be the major feature.

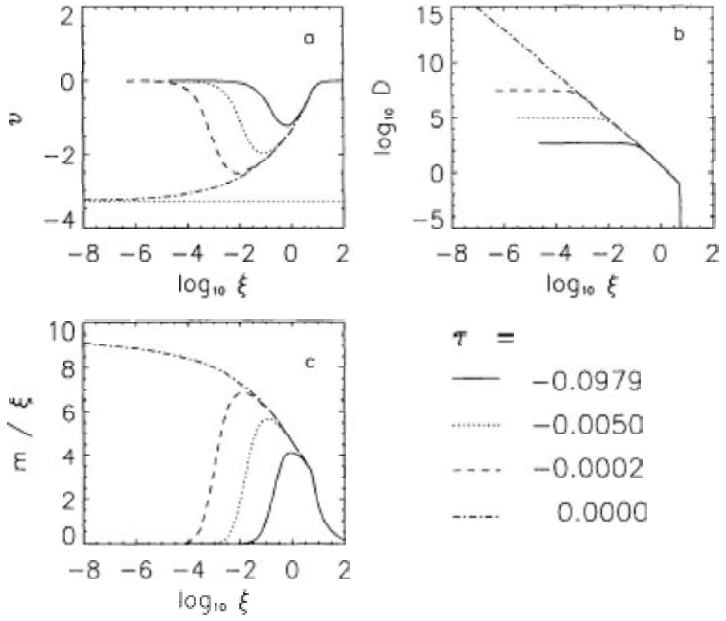

Figure 1.2: Radial profiles of the velocity, density, and enclosed mass over radius for the standard case are presented, at several times prior to core formation. The profiles shown are for a run with 200 zones. The horizontal line in plot *a* represents the Larson-Penston solution at core formation. (From Foster&Chevalier [6], Figure 1. For explanation on the units, see Section 3.2.2.)

From the 1980's on, the collapse models were extended to (mainly) 2 and 3 spatial dimensions, including rotation. This seemed to complicate the results a lot, because fragmentation of the collapsing cloud appears to be highly related to the choice of the initial conditions. Despite the extended observational research of star-forming regions, there is still great uncertainty about the detailed conditions that precede proto-stellar formation.

1.3 Relevance

Although it seems that, in view of modern development of 3-dimensional hydrodynamic codes with adaptive mesh refinement, that 1-dimensional modelling is a trip back into history, there is still some relevance to this project. One of the most important motivations is the actual implementation of the Roe solver for

gravitational collapse, as a test case. If successful, the implementation might be extended into 3 dimensions, including rotation, chemistry, radiative transfer and cooling functions. Another major motivation is the project as a learning experience on hydrodynamics and numerical modelling. These subjects are only poorly covered by the current master curriculum in Leiden. As for the physical relevance, the expected high accuracy of the Roe solver might reveal detail in the gravitational collapse that was not detectable before in any of the earlier models. In any case, confirmation of the features that were observed in earlier models would be a useful result on its own.

1.4 Overview

Chapter 2 contains the physics that was used to construct the model. This includes a mathematical introduction to the Roe method and the numerical methods contained within the Roe solver. In Chapter 3, the simulation results of test problems and gravitational collapses are presented. Chapter 4 contains a summary of the work done, conclusions and a recommendation for future work.

Chapter 2

Method

2.1 Gas physics

On macroscopic scale it is impossible to describe the state and motion of a gas as a collection of individual particles, due to the very large number of particles. Instead, the gas can be treated as a continuous matter distribution, described by macroscopic parameters like mass density ρ, pressure P and temperature T. Statistical physics, thermodynamics and hydrodynamics are areas of physics where the macroscopic behaviour of matter is studied. Some of the resulting equations of these studies are presented in this chapter. From these equations a model is built that, to some extent, mimics the behaviour of a real cloud of gas in space.

In the model, the state of the gas can be expressed using a minimal set of primitive variables. In this paper, the minimal set used consists of the gas mass density ρ, the gas bulk velocity $\vec{v}$ in three spatial dimensions, the pressure P and the gravitational potential Φ. All other macroscopic parameters can be derived from this minimal set. Every macroscopic parameter may vary in space and time, and are therefore functions of the spatial position $\vec{r}$ and time t. In this paper, these dependencies will not be mentioned explicitly (unless to clarify things), so it is assumed that $\rho \equiv \rho(\vec{r}, t)$, $P \equiv P(\vec{r}, t)$, etc.

2.1.1 Gas equation of state

If a gas is assumed to obey the ideal gas law, there is a relation between pressure P, mass density ρ and temperature T at any point in the gas:

$$P = nkT = \frac{k}{\mu m_H}\rho T \tag{2.1}$$

n is the number density of particles in the gas, k is Boltzmann's constant and μm_H is the average particle mass, expressed as the product of the relative mass μ and the mass m_H of the hydrogen atom. Furthermore, when shocks are absent in a local part of space, entropy is assumed to be conserved, which can be expressed in an adiabatic relation between P and ρ:

$$P = \kappa\rho^{\Gamma} \tag{2.2}$$

$\Gamma = c_P/c_V$ is the adiabatic index, the quotient of the heat capacity c_P per particle at constant pressure and the heat capacity c_V per particle at constant volume. The constant κ is a non-global constant and depends on the initial values of ρ and P. c_P and c_V depend on Q, the number of internal degrees of freedom of the gas particles:

$$c_V = (\frac{3}{2} + Q)k, \quad c_P = (\frac{5}{2} + Q)k = c_V + k$$
$$\Rightarrow \quad \Gamma = \frac{c_V + k}{c_V} \quad \Rightarrow \quad c_V = \frac{k}{\Gamma - 1} \tag{2.3}$$

From Equations (2.1) and (2.2) it follows that:

$$P \sim \rho T \sim \rho^{\Gamma} \quad \Rightarrow \quad T \sim \rho^{\Gamma - 1} \tag{2.4}$$

Thus, if $\Gamma \to 1$, T is independent of ρ (and P), making the gas isothermal. According to (2.3), $\Gamma \to 1$ means that $c_V \to \infty$ and $Q \to \infty$. The number of internal degrees of freedom Q goes to infinity. Each degree of freedom can store a certain amount of energy. Thus, the gas' capacity to store energy (or heat) is unlimited, as is implied by $c_V \to \infty$.

The internal energy density of the gas is given by:

$$e_{int} = nc_V T = \frac{nkT}{\Gamma - 1} = \frac{P}{\Gamma - 1} \tag{2.5}$$

Here we used Equations (2.1) and (2.3). If $\Gamma \to 1$, the internal energy will dominate over all other possible forms of energy. (Therefore, any energy equation will become obsolete in this special case.)

2.1.2 Hydrodynamic equations of motion

Because the gas is treated as a continuous matter distribution, it will behave like a compressable fluid, with a state equation given by (2.1). The mass density ρ and pressure P are assumed to be low compared to a real fluid like water, so that viscosity, shear forces and thermal conduction can be neglected. The resulting equations of motion can be found in Shu [15], derived in a very clear and self-consistent manner. These equations are referred to as the Euler equations.

The basic idea behind the Euler equations is conservation of mass, momentum and energy. The first Euler equation of mass yields the mass continuity equation, expressed in cartesian coordinates ($\vec{r} = (x_1, x_2, x_3)$, $\vec{v} = (v_1, v_2, v_3)$):

$$\frac{\partial}{\partial t}(\rho) + \frac{\partial}{\partial x_j}(\rho v_j) = 0 \tag{2.6}$$

The summation convention is used for index $j \in \{1, 2, 3\}$. From here on, summation convention is used for all pairs of equal indices. The second Euler equation of momentum reads:

$$\frac{\partial}{\partial t}(\rho v_i) + \frac{\partial}{\partial x_j}(\rho v_i v_j + P\delta_{ij}) = -\rho \frac{\partial}{\partial x_i}(\Phi) \tag{2.7}$$

This is actually three equations, one for every spatial direction with index $i \in \{1, 2, 3\}$. The gravitational potential Φ might contain self-gravitation of the gas

and gravitational interaction with external mass. The Kronecker delta δ_{ij} is one for $i = j$, else zero. The third Euler equation of energy reads:

$$\frac{\partial}{\partial t}(e) + \frac{\partial}{\partial x_j}([e + P]v_j) = -\rho v_j \frac{\partial}{\partial x_j}(\Phi) \tag{2.8}$$

The energy density e consists of kinetic energy density e_{kin} due to the bulk motion of the gas and internal energy density e_{int} (see (2.5)):

$$e = e_{kin} + e_{int} = \frac{1}{2}\rho v_j v_j + \frac{P}{\Gamma - 1} \tag{2.9}$$

2.1.3 Sound speed

The sound speed c_s is the signal speed at which perturbations in the gas state travel through a volume of gas at rest. The sound speed c_s may vary in space and time and is defined by:

$${c_s}^2 = \frac{\mathrm{d}P}{\mathrm{d}\rho} \tag{2.10}$$

When the change in pressure leads to an adiabatic expansion (or compression) of the gas, (2.2) can be used:

$${c_s}^2 = \frac{\mathrm{d}}{\mathrm{d}\rho}\left(\kappa\rho^\Gamma\right) = \Gamma\kappa\rho^{\Gamma-1} = \frac{\Gamma\kappa\rho^\Gamma}{\rho} = \frac{\Gamma P}{\rho} \quad \Rightarrow$$

$$c_s = \sqrt{\frac{\Gamma P}{\rho}} \tag{2.11}$$

Because ρ and P might vary from place to place, so does c_s. It is therefore better to refer to c_s as the local sound speed.

With the bulk of gas at rest, a perturbation at a single point travels away in all directions with the local sound speed. When considering a moving gas with bulk velocity $v = |\vec{v}| > 0$, the local sound speed is superimposed upon the bulk velocity v. In the direction of $\vec{v}$, the signal speed is given by $v + c_s$, while in the opposite direction the signal speed is $v - c_s$. When comparing v to c_s, three cases are identified:

- Subsonic velocity, which means that $v < c_s$.
- Sonic velocity, which means that $v = c_s$.
- Supersonic velocity, which means that $v > c_s$.

The Mach number $\mathcal{M}$ is defined as:

$$\mathcal{M} = \frac{v}{c_s} \tag{2.12}$$

With subsonic velocity ($\mathcal{M} < 1$), signals due to perturbations at a fixed point in space travel away from this point, regardless of the direction in which the signal travels. With sonic velocity ($\mathcal{M} = 1$), signals in the opposite direction of $\vec{v}$ are at rest relative to the source of perturbations. This tends to enhance the perturbation. With supersonic velocity ($\mathcal{M} > 1$), all signals travel in the direction $\vec{v}$. The transition from subsonic to supersonic gas flow (or reverse) crosses the sonic velocity, at which point enhanced perturbations create a discontinuous transition in the gas state, also called a shock wave.

2.1.4 Gravity

Every particle in a gas interacts with other particles through gravitation. Newton assumed that the force $\vec{F}_n$ on a particle with position $\vec{r}$ and unit mass due to a particle n with position $\vec{r}_n$ and mass m_n is given by:

$$\vec{F}_n = \frac{Gm_n(\vec{r}_n - \vec{r})}{|\vec{r}_n - \vec{r}|^3} \tag{2.13}$$

The total gravitational force $\vec{F}$ on a unit mass particle due to N particles is just a superposition of N forces due to (2.13):

$$\vec{F} = \sum_{n=1}^{N} \vec{F}_n = \sum_{n=1}^{N} \frac{Gm_n(\vec{r}_n - \vec{r})}{|\vec{r}_n - \vec{r}|^3} \tag{2.14}$$

When dealing with a continuous mass distribution ρ, the sum changes to an integral over all of space:

$$\vec{F} = \int \frac{G\rho(\vec{s})(\vec{s} - \vec{r})}{|\vec{s} - \vec{r}|^3} \mathrm{d}^3\vec{s} \tag{2.15}$$

The particle position $\vec{r}_n$ is replaced by the mass distribution position $\vec{s}$. The mass m_n is replaced by the mass element $\rho(\vec{s})\mathrm{d}^3\vec{s}$, the product of the mass density $\rho(\vec{s})$ and a volume element $\mathrm{d}^3\vec{s}$. It is common to write the gravitational force $\vec{F}$ as the negative gradient of the gravitational potential Φ (e.g. see Binney&Tremaine [1], Chapter 2):

$$\vec{F} = -\vec{\nabla}\Phi \quad \Rightarrow \quad \Phi = \int \frac{G\rho(\vec{s})}{|\vec{s} - \vec{r}|} \mathrm{d}^3\vec{s} \tag{2.16}$$

Taking the negative divergence of $\vec{F}$ leads to the Poisson equation of gravity:

$$-\vec{\nabla} \cdot \vec{F} = \vec{\nabla} \cdot \vec{\nabla}\Phi \equiv \nabla^2\Phi = 4\pi G\rho \tag{2.17}$$

Unlike other forces in nature, gravitation is a long range force. This means that mass outside the boundaries of the gas must also be taken into account when evaluating the integral in (2.16). Because Φ is linear in ρ, it can be split into two parts: the gravitational potential Φ_{sg} due to the mass density ρ_{sg} of the gas itself (self-gravitation) and the gravitational potential Φ_{ext} due to all mass density ρ_{ext} outside the gas:

$$\begin{aligned} \Phi &= \int \frac{G\left[\rho_{sg}(\vec{s}) + \rho_{ext}(\vec{s})\right]}{|\vec{s} - \vec{r}|} \mathrm{d}^3\vec{s} = \int \frac{G\rho_{sg}(\vec{s})}{|\vec{s} - \vec{r}|} \mathrm{d}^3\vec{s} + \int \frac{G\rho_{ext}(\vec{s})}{|\vec{s} - \vec{r}|} \mathrm{d}^3\vec{s} \\ &\equiv \Phi_{sg} + \Phi_{ext} \end{aligned} \tag{2.18}$$

This idea works exactly the same for the gravitational force $\vec{F}$:

$$\begin{aligned} \vec{F} &= -\vec{\nabla}\Phi = -\vec{\nabla}\left[\Phi_{sg} + \Phi_{ext}\right] = -\vec{\nabla}\Phi_{sg} - \vec{\nabla}\Phi_{ext} \\ &\equiv \vec{F}_{sg} + \vec{F}_{ext} \end{aligned} \tag{2.19}$$

From electromagnetism it is known that the signal speed of electromagnetic interactions is finite, namely the speed of light c. Relativity theory says this

is the same for gravitational interactions. When the mass density $\rho = \rho(\vec{s})$ is constant in time, all formulas above are still valid. However, when $\rho = \rho(\vec{s}, t)$ changes with time t, formulas (2.15) and (2.16) are replaced by:

$$\vec{F} = \int \frac{G\rho(\vec{s}, t_r)(\vec{s} - \vec{r})}{|\vec{s} - \vec{r}|^3} \mathrm{d}^3\vec{s} \tag{2.20}$$

$$\Phi = \int \frac{G\rho(\vec{s}, t_r)}{|\vec{s} - \vec{r}|} \mathrm{d}^3\vec{s} \tag{2.21}$$

The time $t_r = t - \frac{|\vec{s}-\vec{r}|}{c}$ is called the retarded time. The time difference $\Delta t = t - t_r = \frac{|\vec{s}-\vec{r}|}{c}$ is the time it takes for the gravitational signal to travel from the source (mass element) at position $\vec{s}$ to the observer at position $\vec{r}$. When Δt is very small compared to the dynamical time scale t_{dyn} at which $\rho(\vec{r}, t)$ changes significantly ($\Delta t \ll t_{dyn}$), Δt can be ignored and t_r can be replaced by t in (2.20) and (2.21). This results in Equations (2.15) and (2.16).

2.2 Model description

The model starts with a simplified version of a contracted cloud of gas, at rest with respect to the local centre of mass, surrounded by a lower mass density environment. It is assumed that the size L of the cloud, including its local environment, is small compared to the distance D to any external mass distribution, so $L \ll D$. As a consequence, the cloud and its local environment are freefalling in the external gravitational potential Φ_{ext} and tidal forces can be ignored. When a coordinate system is used that has its origin fixed at the local centre of mass, the influence of Φ_{ext} can be ignored altogether (so $\Phi_{ext} = 0$ and $\vec{F}_{ext} = \vec{0}$, see Section 2.1.4).

Furthermore, it is a priori assumed that in this model the dynamical time scale t_{dyn} on which the mass density ρ changes significantly is much larger than the maximum travel time $\Delta t \sim L/c$ of gravitational interactions. The conditions under which this is true are examined in Section 2.2.4. As a consequence, the gravitational force and gravitational potential can be calculated from the current mass density distribution with (2.15) and (2.16).

All the gas in the model is assumed to be (and to stay) neutral atomic hydrogen, so $\mu = 1$ (see (2.1)). No magnetic fields are produced by the gas and it is assumed that externally generated magnetic fields are too weak to influence the gravitational collapse. As the focus of this research project is more on the dynamical aspects of the collapse than the chemical, it is assumed that no chemical reactions, ionisations or excitations take place. This makes the gas perfectly transparent for radiation. All radiative energy that might be generated in the process of gravitational collapse is assumed to be transmitted away from the cloud without being absorbed (this is probably the biggest oversimplification of the problem). The neutral atomic hydrogen is assumed to have no internal degrees of freedom, so $Q = 0$ and $\Gamma = 5/3$ (see (2.3)).

2.2.1 Spherical symmetry

For simplicity, the initial contracted cloud of gas is assumed to have a spherically symmetric mass density at rest relative to the origin at the centre of mass. The

low mass density environment can be modeled as a constant mass density ρ_{env} that extends over all of space outside the contracted cloud. An example of such a mass density distribution is shown in Figure 2.1. The density ρ can be thought of as a superposition of a homogeneous mass density ρ_{env} (dotted line) and an mass density excess $\rho_{cl} \equiv \rho - \rho_{env}$ due to the contracted cloud. Changing from

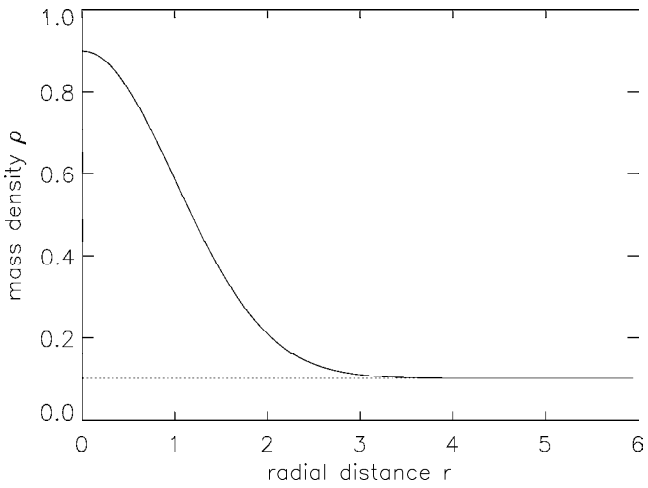

Figure 2.1: Example of a mass density distribution of a denser cloud embedded in a less dense environment (dotted line). The axis-units for r and ρ are arbitrary.

cartesian coordinates $\vec{r} = (x, y, z)$ to spherical (polar) coordinates $\vec{r} = (r, \theta, \phi)$ is an obvious choice, because the mass densities ρ and ρ_{cl} are both spherically symmetric around the origin and ρ_{env} is spherically symmetric around all points in space.

Based on the same superposition principle used in Section 2.1.4, the self-gravitational force $\vec{F}_{sg}$ of the mass density ρ can be split into a contribution from ρ_{env} and ρ_{cl}:

$$\vec{F}_{sg} = \vec{F}_{env} + \vec{F}_{cl} \tag{2.22}$$

From symmetry considerations, it is easy to see that $\vec{F}_{env} = \vec{0}$. In a homogeneous medium, the gravitational pull of any mass element at some position $\vec{r}$ on a unit mass at the origin is cancelled by the gravitational pull of an equal mass element at position $-\vec{r}$. So the integral in (2.15) over all mass elements in space gives zero. Because ρ_{env} is spherically symmetric around all points in space, the origin can be placed at any point in space without changing the result of the integral, so $\vec{F}_{env} = \vec{0}$ for all $\vec{r}$. From (2.16) it follows that $\Phi_{env} = constant$. For simplicity, we choose $\Phi_{env} = 0$.

A common approach in spherically symmetric mass density distributions is to divide it into spherical shells with radius r and infinitesimal thickness $\mathrm{d}r$, all centered around the common origin at $r = 0$. The mass (excess) $\mathrm{d}M(r)$ of a shell at radius r is given by:

$$\mathrm{d}M(r) = 4\pi r^2 \rho_{cl}(r)\mathrm{d}r \tag{2.23}$$

The mass excess $M(r)$ enclosed within a radius r is given by:

$$M(r) = \int_0^r \mathrm{d}M(s) = 4\pi \int_0^r s^2 \rho_{cl}(s)\mathrm{d}s \tag{2.24}$$

The total mass excess M is given by:

$$M \equiv M(\infty) = 4\pi \int_0^\infty s^2 \rho_{cl}(s)\mathrm{d}s \tag{2.25}$$

Calculating $\vec{F}_{cl}$ is simplified by using the spherically symmetric version of (2.15) (e.g. see Binney&Tremaine [1], (2-23a&b)):

$$\vec{F}_{cl} = -\frac{GM(r)\vec{r}}{r^3} \tag{2.26}$$

From (2.26) it can be seen that $\vec{F}_{cl}$ only acts in the radial direction. Any acceleration of matter due to self-gravity is also directed radially and thus the spherical symmetry of the mass density distribution is conserved. Conservation of angular momentum makes sure that the initially non-rotating cloud will not start rotating due to self-gravity. With the additional assumption that the initial gas pressure is also spherically symmetric, the whole model becomes and stays spherically symmetric.

Because none of the macroscopic gas parameters depend on θ or ϕ (or v_θ or v_ϕ) any more, these coordinates become obsolete and can be left out. The number of spatial dimensions in the model is then reduced from three to one. All spatial vectors can be reduced to scalars, like the gravitational force:

$$F = F_{ext} + F_{sg} = F_{env} + F_{cl} = -\frac{GM(r)}{r^2} \tag{2.27}$$

From (2.16) it follows that (see Binney&Tremaine [1], (2-22)):

$$F = -\frac{\partial \Phi}{\partial r} \quad \Rightarrow \quad \Phi = -4\pi G \left[\frac{1}{r}\int_0^r s^2 \rho_{cl}(s)\mathrm{d}s + \int_r^\infty s\rho_{cl}(s)\mathrm{d}s\right] \tag{2.28}$$

The Poisson equation of gravity (Eq.(2.17)) becomes:

$$\frac{1}{r^2}\frac{\partial}{\partial r}\left(r^2 \frac{\partial \Phi}{\partial r}\right) = 4\pi G \rho_{cl} \tag{2.29}$$

In Appendix A the Euler equations are derived in case of spherical symmetry. The mass continuity equation is given by:

$$\frac{\partial}{\partial t}\left(r^2\rho\right) + \frac{\partial}{\partial r}\left(r^2 \rho v_r\right) = 0 \tag{2.30}$$

The equation of momentum is:

$$\frac{\partial}{\partial t}\left(r^2 \rho v_r\right) + \frac{\partial}{\partial r}\left(r^2\left[\rho {v_r}^2 + P\right]\right) = r^2\left[\frac{2P}{r} - \rho\frac{\partial \Phi}{\partial r}\right] \tag{2.31}$$

And the equation of energy is:

$$\frac{\partial}{\partial t}\left(r^2 e\right) + \frac{\partial}{\partial r}\left(r^2\left[e + P\right]v_r\right) = -r^2 \rho v_r \frac{\partial \Phi}{\partial r} \tag{2.32}$$

Here, e is the total energy density, similar to (2.9):

$$e = e_{kin} + e_{int} = \frac{1}{2}\rho {v_r}^2 + \frac{P}{\Gamma - 1} \tag{2.33}$$

2.2.2 Homogeneous sphere

The concept of spherical shells can be used to construct any spherically symmetric mass density distribution. Constructing means adding shells on top of each other, starting with a shell at $r = 0$. Any new shell is moved in from $r = \infty$ to $r = r$, therefore losing potential energy in the gravitational potential of the already present mass excess $M(r)$. The gravitational potential energy $\mathrm{d}E_{pot}(r)$ lost to put one mass shell on top of underlying shells is given by (e.g. see Caroll&Ostlie [3], Section 10.3):

$$\mathrm{d}E_{pot}(r) = -\frac{GM(r)}{r}\mathrm{d}M(r) = -4\pi G r M(r)\rho_{cl}\mathrm{d}r \tag{2.34}$$

Constructing a complete spherically symmetric mass density distribution leads to the total gravitational potential energy E_{pot}:

$$E_{pot} = \int_0^\infty \mathrm{d}E_{pot}(s) = -4\pi G \int_0^\infty sM(s)\rho_{cl}(s)\mathrm{d}s \tag{2.35}$$

A simple model of a cloud of gas with a spherically symmetric mass density is a homogeneous sphere, or 'top-hat', with radius R:

$$\rho(r) = \begin{cases} \rho_{env} + \rho_0 & r \leq R \\ \rho_{env} & r > R \end{cases} \tag{2.36}$$

Both ρ_0 and ρ_{env} are constants. From (2.24) and (2.36) it follows that:

$$M(r) = \begin{cases} \frac{4}{3}\pi\rho_0 r^3 & r \leq R \\ \frac{4}{3}\pi\rho_0 R^3 & r > R \end{cases} \tag{2.37}$$

The total mass excess M follows from (2.25):

$$M = M(R) = \frac{4}{3}\pi\rho_0 R^3 \quad \Leftrightarrow \quad \rho_0 = \frac{3M}{4\pi R^3} \tag{2.38}$$

And the total gravitational potential energy E_{pot} is given by:

$$\begin{aligned} E_{pot} &= -4\pi G \int_0^R sM(s)\rho_0\mathrm{d}s = -\frac{16}{3}\pi^2 G{\rho_0}^2 \int_0^R s^4\mathrm{d}s \\ &= -\frac{3}{5}\frac{GM^2}{R} \end{aligned} \tag{2.39}$$

Here, (2.38) was used.

For a gas cloud that is gravitationally bound and stable (not collapsing nor expanding), the virial theorem applies (e.g. see see Caroll&Ostlie [3], Section 2.4):

$$2E_{int} = -E_{pot} \tag{2.40}$$

E_{int} is the total internal energy of the cloud. Basically, (2.40) decribes the mechanical balance (hydrostatic equilibrium) between self-gravity ($\sim E_{pot}$) and pressure ($\sim E_{int}$). When the cloud collapses, self-gravity dominates over pressure, so that:

$$2E_{int} \ll -E_{pot} \tag{2.41}$$

When the cloud is isothermal, E_{int} is similar to (2.5):

$$E_{int} = \frac{NkT}{\Gamma - 1}, \quad N = \frac{M}{\mu m_H} \tag{2.42}$$

N is the total number of particles in the cloud.

Suppose that the 'top-hat'-cloud has the same temperature T everywhere and is stable and gravitationally bound, so the cloud neither expands nor collapses. Combining (2.39), (2.38), (2.40) and (2.42) gives:

$$M \equiv M_J = \sqrt{\frac{3}{4\pi\rho_0}} \left(\frac{10kT}{(\Gamma - 1)3G\mu m_H} \right)^{\frac{3}{2}} \tag{2.43}$$

M_J is called the Jeans mass. When a 'top-hat'-cloud with constant mass density excess ρ_0 and constant temperature T has a total mass excess M that exceeds M_J, (2.41) is true and the cloud collapses. So M_J is the critical mass above which the 'top-hat'-cloud collapses. Even for non-top-hat clouds, the Jeans mass M_J can be used as an critical mass indicator, using average values of the macroscopic gas parameters in the calculation of M_J. Using (2.1), the Jeans mass can also be expressed in terms of constant mass density excess ρ_0 and constant pressure P:

$$\frac{kT}{\mu m_H} = \frac{P}{\rho_0} \quad \Rightarrow \quad M_J = \sqrt{\frac{3}{4\pi\rho_0}} \left(\frac{10P}{(\Gamma - 1)3G\rho_0} \right)^{\frac{3}{2}} \tag{2.44}$$

The Jeans radius R_J is the maximum radius of a 'top-hat'-cloud with constant mass density excess ρ_0 and constant temperature T (or constant pressure P) for which the mass excess M equals the Jeans mass M_J:

$$\begin{aligned} &M_J = \frac{4}{3}\pi R_J^3 \rho_0 \quad \Rightarrow \\ &R_J = \sqrt{\frac{10kT}{(\Gamma - 1)4\pi G\rho_0 \mu m_H}} = \sqrt{\frac{10P}{(\Gamma - 1)4\pi G{\rho_0}^2}} \end{aligned} \tag{2.45}$$

2.2.3 Hydrostatic equilibrium

The homogeneous sphere of Section 2.2.2 does not seem to be a very likely mass density distribution for a real cloud of gas in space. A mass density distribution which is probably much closer to reality is a spherical distribution in hydrostatic equilibrium. In this situation, the self-gravitational force of the gas that is directed inwards is balanced by the pressure gradient of the gas that is directed outwards. As a result, the (radial) velocity v_r of the gas is zero in space and time and all other macroscopic gas parameters are constant in time (and thus functions of r only). The equation of hydrostatic equilibrium can be retrieved from Eq. (2.31) (with $v_r = 0$):

$$\frac{\partial}{\partial r}\left(r^2 P\right) = r^2 \left[\frac{2P}{r} - \rho \frac{\partial \Phi}{\partial r} \right] \quad \Rightarrow \quad \frac{\partial P}{\partial r} = -\rho \frac{\partial \Phi}{\partial r} = \rho F \tag{2.46}$$

Here, (2.28) was used. Hydrostatic equilibrium states are a subgroup of the stationary solutions, derived in Section B.2 (with $D = 0$).

2.2.4 Free-fall

A cloud with a mass that is larger the Jeans mass cannot maintain hydrostatic equilibrium and will collapse. During the first part of the collapse, the gravitational force dominates over the pressure gradient (compare (2.46)):

$$\frac{\partial P}{\partial r} \ll \rho F \tag{2.47}$$

The mass of the cloud enters a free-fall motion towards the origin at $r = 0$. This results in a fairly simple equation of motion for a unit mass at radius r:

$$\frac{\partial^2 r}{\partial t^2} = F = -\frac{GM(r)}{r^2} \tag{2.48}$$

Suppose now that (2.47) is true for the whole collapse. This is not such a bad assumption, because in most cases the pressure gradient will become significant again only at small r. Then (2.48) can be integrated to find r as a function of t. This is done in Carroll&Ostlie [3], Section 12.2, for a top-hat-cloud with mass density ρ_0 and radius R (similar to the top-hat-cloud in Section 2.2.2) that is initially at rest. From this result, it can be calculated how long it takes for the mass at $r = R$ to reach $r = 0$. This is called the free-fall time t_{ff} and is given by:

$$t_{ff} = \sqrt{\frac{3\pi}{32 G \rho_0}} \tag{2.49}$$

Even for non-top-hat clouds, the free-fall time t_{ff} can be used as an indicator for the time of collapse, using average values of the macroscopic gas parameters in the calculation of t_{ff}.

The free-fall time t_{ff} can be used as an order estimate for the dynamical time scale t_{dyn} on which the mass density ρ changes significantly. Furthermore, the Jeans radius R_J can be used as an order estimate for the size L of the cloud including its local environment. Examining the conditions under which $\Delta t \ll t_{dyn}$ leads to:

$$\begin{aligned} &\Delta t \sim \frac{L}{c} \sim \frac{R_J}{c} \sim \frac{1}{c}\sqrt{\frac{P}{G{\rho_0}^2}}, \\ &t_{dyn} \sim t_{ff} \sim \sqrt{\frac{1}{G\rho_0}} \\ &\Delta t \ll t_{dyn} \quad \Rightarrow \quad \sqrt{\frac{P}{\rho_0}} \ll c \end{aligned} \tag{2.50}$$

According to (2.11), $c_s \sim \sqrt{P/\rho_0}$, so that (2.50) is similar to $c_s \ll c$. Thus, for $\Delta t \ll t_{dyn}$ to be true, the sound speed c_s within the gas cloud should be much smaller than the speed of light c. This is in general true for classical, non-relativistic mechanics (because then $P \ll \rho c^2$, see Appendix A).

2.3 Roe method

To determine the dynamic behaviour of the collapsing cloud of gas, it is necessary to solve the three partial differential equations (Eqs. (2.30)-(2.32)) that make

up the Euler equations. As these three equations all have the same layout, the following vector notation can be introduced:

$$\mathbf{W} = r^2 \begin{pmatrix} \rho \\ \rho v_r \\ e \end{pmatrix}, \quad \mathbf{F} = r^2 \begin{pmatrix} \rho v_r \\ \rho {v_r}^2 + P \\ [e + P]\, v_r \end{pmatrix}, \quad \mathbf{S} = r^2 \begin{pmatrix} 0 \\ \frac{2P}{r} - \rho \frac{\partial \Phi}{\partial r} \\ -\rho v_r \frac{\partial \Phi}{\partial r} \end{pmatrix} \tag{2.51}$$

The Euler equations become:

$$\frac{\partial \mathbf{W}}{\partial t} + \frac{\partial \mathbf{F}}{\partial r} = \mathbf{S} \tag{2.52}$$

The state vector $\mathbf{W}$ represents the state of the gas (density, momentum and energy) within a infinitely thin spherical shell at radius r. The flux vector $\mathbf{F}$ represents the flux (of density, momentum and energy) through the surface of the shell that might change the gas state. The source vector $\mathbf{S}$ represents sources (of density, momentum and energy) within the shell that might change the gas state.

With the exception of a very few cases, it is not possible to find analytical solutions for (2.52). However, it is possible to find approximate solutions for local parts of space over a limited time interval. Roe [13] developed an approximate Riemann-solver (see Section 2.3.3) for Cartesian grids, which performs excellent compared to other methods. Eulderink&Mellema [4] developed a generalised version of the Roe method, applicable for both relativistic and non-relativistic cases through the use of general coordinates. In this method, the (self-)gravitional potential enters the (Euler) equations of motion through the metric of space-time, opposed to adding the gravitational force manually as a source term. The method used in this report is copied from the application of the Roe method on planetary nebulae in Mellema et al. [9] with some small adjustments. In this section, some of the basic theory of this method are discussed. Section 2.4 continues on the numerical details.

Solving Equation (2.52) numerically is difficult to perform at once. It is more convenient to split up this equation into parts which can be solved or approximated. Therefore, a technique called operator splitting is used. With this technique, Equation (2.53) is split into three separate vector equations:

$$\frac{\partial \mathbf{W}}{\partial t} + \frac{\partial \mathbf{F}}{\partial r} = 0 \tag{2.53}$$

$$\frac{\partial \mathbf{W}}{\partial t} = \mathbf{S} \tag{2.54}$$

$$\frac{\partial \mathbf{F}}{\partial r} = \mathbf{S} \tag{2.55}$$

It can be shown (see Eulderink&Mellema, Appendix C) that numerically solving these equations after each other yields a second order accurate solution. Integrating (2.55) is equal to finding stationary solutions, see Section B.2.

2.3.1 Hyperbolic equations

Equations of the form (2.53) are called hyperbolic equations. Two properties of a hyperbolic equation are that signals of state changes travels at a finite velocities and that discontinuities (or jumps) in the state variables are allowed. In this

case, the signal velocity represents the sound speed in (2.11), superimposed upon the velocity of the gas. A discontinuity represents a shock in the gas, a transistion between a subsonic gas flow and a supersonic gas flow.

At a fixed position r and time t, the flux $\mathbf{F}$ can be expressed as a function of the state $\mathbf{W}$ only. Then (2.53) can be written as:

$$\frac{\partial \mathbf{W}}{\partial t} + \frac{\partial \mathbf{F}}{\partial r} = \frac{\partial \mathbf{W}}{\partial t} + \frac{\partial \mathbf{F}}{\partial \mathbf{W}} \cdot \frac{\partial \mathbf{W}}{\partial r} \equiv \frac{\partial \mathbf{W}}{\partial t} + \mathbb{A}\frac{\partial \mathbf{W}}{\partial r} = 0 \tag{2.56}$$

The Jacobian $\mathbb{A} = \partial \mathbf{F}/\partial \mathbf{W}$ is also a function of $\mathbf{W}$. For very small variations in r and t, $\mathbb{A}$ is roughly constant. With a constant $\mathbb{A}$, a small change in $\mathbf{W}$ causes an approximately linear change in $\mathbf{F}$:

$$\Delta \mathbf{F} \approx \mathbb{A}\Delta \mathbf{W} \quad \Rightarrow \quad \mathbf{F} + \Delta \mathbf{F} \approx \mathbf{F} + \mathbb{A}\Delta \mathbf{W} \tag{2.57}$$

The Jacobian $\mathbb{A}$ can be represented by a matrix, with elements $A_{ab} = \partial F_a/\partial W_b$ $(a, b \in \{1, 2, 3\})$. Because the determinant of this matrix is non-zero, the eigenvectors $\mathbf{e}_c$ $(c \in \{1, 2, 3\})$ belonging to the eigenvalues λ_c are a complete set. This means that $\Delta \mathbf{F}$ and $\Delta \mathbf{W}$ can be expressed in terms of these eigenvectors:

$$\begin{aligned}
&\Delta \mathbf{W} = \sum_{c=1}^{3} a_c \mathbf{e}_c \\
&\Delta \mathbf{F} = \sum_{c=1}^{3} b_c \mathbf{e}_c \approx \mathbb{A}\Delta \mathbf{W} = \mathbb{A}\sum_{c=1}^{3} a_c \mathbf{e}_c = \sum_{c=1}^{3} \lambda_c a_c \mathbf{e}_c \quad \Rightarrow \\
&b_c \approx \lambda_c a_c
\end{aligned} \tag{2.58}$$

The eigenvalues and eigenvectors of the Jacobian are derived in Section B.1:

$$\lambda_1 = v_r, \qquad \lambda_2 = v_r + c_s, \qquad \lambda_3 = v_r - c_s \tag{2.59}$$

$$\mathbf{e}_1 = \begin{pmatrix} 1 \\ \lambda_1 \\ \frac{1}{2}{v_r}^2 \end{pmatrix}, \quad \mathbf{e}_2 = \begin{pmatrix} 1 \\ \lambda_2 \\ \frac{e+P}{\rho} + v_r c_s \end{pmatrix}, \quad \mathbf{e}_3 = \begin{pmatrix} 1 \\ \lambda_3 \\ \frac{e+P}{\rho} - v_r c_s \end{pmatrix} \tag{2.60}$$

The sound speed c_s is given by (2.11).

The following matrix notation is introduced:

$$\mathbb{E} = \begin{pmatrix} | & | & | \\ \mathbf{e}_1 & \mathbf{e}_2 & \mathbf{e}_3 \\ | & | & | \end{pmatrix}^{\mathrm{T}}, \qquad \mathbf{a} = \begin{pmatrix} a_1 \\ a_2 \\ a_3 \end{pmatrix}, \qquad \mathbf{b} = \begin{pmatrix} b_1 \\ b_2 \\ b_3 \end{pmatrix} \tag{2.61}$$

The coefficients a_c and b_c are now given by:

$$\begin{aligned}
&\Delta \mathbf{W} = \mathbb{E}\mathbf{a} \quad \Rightarrow \quad \mathbf{a} = \mathbb{E}^{-1}\Delta \mathbf{W} \quad \Rightarrow \\
&a_1 = \frac{\Gamma - 1}{{c_s}^2}\left(\left[\frac{e+P}{\rho} - {v_r}^2\right]\Delta W_1 + v_r \Delta W_2 - \Delta W_3\right) \\
&a_2 = \frac{\Gamma - 1}{2{c_s}^2}\left(\frac{1}{2}{v_r}^2 \Delta W_1 - v_r \Delta W_2 + \Delta W_3\right) + \frac{1}{2c_s}\left(v_r \Delta W_1 - \Delta W_2\right) \\
&a_3 = \frac{\Gamma - 1}{2{c_s}^2}\left(\frac{1}{2}{v_r}^2 \Delta W_1 - v_r \Delta W_2 + \Delta W_3\right) - \frac{1}{2c_s}\left(v_r \Delta W_1 - \Delta W_2\right)
\end{aligned} \tag{2.62}$$

$$\Delta\mathbf{F} = \mathbb{E}\mathbf{b} \quad \Rightarrow \quad \mathbf{b} = \mathbb{E}^{-1}\Delta\mathbf{F} \quad \Rightarrow$$
$$b_1 = \frac{\Gamma-1}{{c_s}^2}\left(\left[\frac{e+P}{\rho} - {v_r}^2\right]\Delta F_1 + v_r\Delta F_2 - \Delta F_3\right)$$
$$b_2 = \frac{\Gamma-1}{2{c_s}^2}\left(\frac{1}{2}{v_r}^2\Delta F_1 - v_r\Delta F_2 + \Delta F_3\right) + \frac{1}{2c_s}\left(v_r\Delta F_1 - \Delta F_2\right)$$
$$b_3 = \frac{\Gamma-1}{2{c_s}^2}\left(\frac{1}{2}{v_r}^2\Delta F_1 - v_r\Delta F_2 + \Delta F_3\right) - \frac{1}{2c_s}\left(v_r\Delta F_1 - \Delta F_2\right) \qquad (2.63)$$

(Note that in Mellema et al. [9], formula (A.5) contains a factor $\gamma - 1$ too much. This should read:

$$b_1 = \frac{\gamma-1}{2s^2}(\ldots) - \frac{1}{2s}\left(\Delta_2 - V_r\Delta_1\right)$$
$$b_2 = \frac{\gamma-1}{2s^2}(\ldots) + \frac{1}{2s}\left(\Delta_2 - V_r\Delta_1\right)$$

)

Feeding a small state perturbation $\Delta\mathbf{W}$ into (2.56) gives:

$$\frac{\partial\Delta\mathbf{W}}{\partial t} + \frac{\partial\Delta\mathbf{F}}{\partial r} = 0 \quad \Rightarrow$$
$$\frac{\partial}{\partial t}\left(\sum_{c=1}^{3} a_c\mathbf{e}_c\right) + \frac{\partial}{\partial r}\left(\sum_{c=1}^{3}\lambda_c a_c\mathbf{e}_c\right) \approx 0 \quad \Rightarrow$$
$$\frac{\partial a_c}{\partial t} + \lambda_c\frac{\partial a_c}{\partial r} \approx 0 \qquad (2.64)$$

These are three wave equations with solutions $a_c(r,t) = a_c(r-\lambda_c t)$. From this it follows that small changes in the state propagate through local space at limited signal velocities, equal to the eigenvalues of the Jacobian. The paths that are traveled by these waves through space-time are named characteristics. Like light cones in relativity theory, the characteristics mark a region of influence in space-time.

2.3.2 CFL-condition

The idea of state changes traveling through space at limited velocities is in general true, also for large state changes and a non-zero source vectors. When considering a short travel time Δt, a state change will only influence the gas within a small distance Δr from its starting point, because of the limited signal velocities. When assuming that the signal velocities are roughly constant during this short time interval, the maximum distance that a signal can travel is given by:

$$\Delta r_{max} \approx \lambda_{max}\Delta t \qquad (2.65)$$

Here, λ_{max} is the maximum of the absolute values of the eigenvalues λ_c.

When attempting to solve a hyperbolic equation locally, this limited range of influence can be used to put a constraint on the maximum time step over which the hyperbolic equation can be integrated. For a given small distance Δr, the maximum time step must satisfy:

$$\Delta t_{max} \lesssim \frac{\Delta r}{\lambda_{max}} \qquad (2.66)$$

This so-called CFL-condition is named after its inventors, Courant, Friedrichs and Lewy. To choose a suitable Δt, the following equation can be used:

$$\Delta t = \zeta \frac{\Delta r}{\lambda_{max}} \tag{2.67}$$

A value of $\zeta = 1/\sqrt{2}$ is often used. To be on the safe side, $\zeta = \frac{1}{2}$ is used in this report.

2.3.3 Riemann problem

The Riemann problem is one of the configurations for which there exists an analytical solution. The one-dimensional setup consists of two stationary flows on both sides of an interface, on which there exists a state discontinuity. Both flows extend to infinity. The Roe method is based on numerically approximating the Riemann problem, locally around the discontinuity, to second order accuracy. Because of the CFL-condition, only a limited distance around every interface needs to be taken into account, when using a small enough time interval. The Roe method (based on the earlier work by Godunov (1959)) divides an arbitrary hydrodynamical configuration into many local stationary flows, separated by state discontinuities. Only when the number of divisions could reach infinity, would the Roe method yield perfect accuracy. In practice this is not true, but still the performance of the Roe method on an approximated hydrodynamical configuration is remarkable.

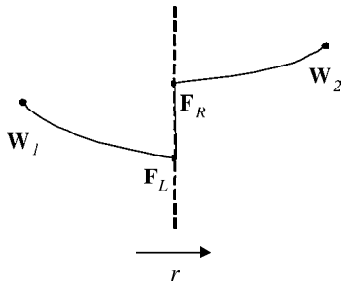

Figure 2.2: Schematic overview of the Riemann problem.

Figure 2.2 shows a schematic overview of the Riemann problem. Left and right of the interface (dashed line), two different stationary flows are present, depicted as curved lines. At some point in space on each side of the interface, the state is known ($\mathbf{W}_1$ and $\mathbf{W}_2$). By means of stationary extrapolation (determining the stationary flow, see Section B.2), the states immediately left and right of the interface ($\mathbf{W}_L$ and $\mathbf{W}_R$) can be determined, from which the fluxes immediately left and right of the interface ($\mathbf{F}_L$ and $\mathbf{F}_R$) can be determined.

To calculate how this configuration develops in time, the true flux $\mathbf{F}$ through the interface needs to be approximated to first order, which yields second order accurate states. Roe found a form which gives an exact solution if the Rankine-Hugoniot jump conditions are valid over the discontinuity (e.g. see Shu [15],

Chapter 15):

$$\mathbf{F} = \frac{1}{2}\left(\mathbf{F}_L + \mathbf{F}_R - \sum_{c=1}^{3} \sigma_c \lambda_c a_c \mathbf{e}_c\right) \tag{2.68}$$

Here, λ_c and $\mathbf{e}_c$ are the eigenvalues and eigenvectors of the Jacobian at the interface. a_c are the projection coefficients of the state difference $\Delta\mathbf{W} = \mathbf{W}_R - \mathbf{W}_L$. σ_c indicates the sign of λ_c:

$$\sigma_c = \begin{cases} +1 & \lambda_c \geq 0 \\ -1 & \lambda_c < 0 \end{cases} \tag{2.69}$$

The equations for λ_c (Eq. (2.59)), $\mathbf{e}_c$ (Eq. (2.60)) and a_c (Eq. (2.62)) cannot be used in their current form, because the state at the interface is undefined due to the discontinuity. Roe suggests using a weighted average of state variables left and right of the interface (indicated by sub-indices $_L$ and $_R$). For the spherically symmetric case, the weight factors K are defined by $K^2 = W_0 = r^2\rho$. The averages of the velocity v_r and the enthalpy $H = \frac{e+P}{\rho}$ are given by:

$$\begin{aligned} v_r \to \widetilde{v_r} &\equiv \frac{K_L v_{r,L} + K_R v_{r,R}}{K_L + K_R} \\ H \to \widetilde{H} &\equiv \frac{K_L H_L + K_R H_R}{K_L + K_R} \end{aligned} \tag{2.70}$$

The averaged sound speed $\widetilde{c_s}$ is defined by:

$$\widetilde{c_s}^2 = (\Gamma - 1)(\widetilde{H} - \frac{1}{2}\widetilde{v_r}^2) \tag{2.71}$$

In practice, the a_c coefficients are not calculated directly from (2.62), but are approximated from the b_c coefficients, using (2.58). The b_c coefficients, which are calculated using (2.63), are not discontinuous on the interface, while the a_c coefficients are. In the approximation for a_c, special care must be taken for the case that $\lambda_c = 0$. The projection coefficients a_c can be calculated from b_c, using:

$$a_c = \frac{b_c}{\lambda_i + \epsilon} \tag{2.72}$$

The very small number ϵ prevents a division by zero.

Equation (2.68) becomes more transparant when realising that:

$$\begin{aligned} \mathbf{F} &= \frac{1}{2}\left(\mathbf{F}_L + \mathbf{F}_R) + \sum_{c=1}^{3}(-\sigma_c)\lambda_c a_c \mathbf{e}_c\right) \\ \sum_{c=1}^{3} \lambda_c a_c \mathbf{e}_c &= \Delta\mathbf{F} = \mathbf{F}_R - \mathbf{F}_L \end{aligned} \tag{2.73}$$

The true interface flux is generated out of projections of either $\mathbf{F}_L$ or $\mathbf{F}_R$ onto the eigenvectors $\mathbf{e}_c$, where σ_c acts as the switch. When $\lambda_c > 0$ ($\sigma_c = +1$), the signal wave travels in positive direction (to the right), so the flow is coming in from the left. In this case, $\mathbf{F}_L$ is projected onto $\mathbf{e}_c$. When $\lambda_c < 0$ ($\sigma_c = -1$), the signal wave travels in negative direction (to the left), so the flow is coming in from the right. In this case, $\mathbf{F}_R$ is projected onto $\mathbf{e}_c$.

2.3.4 Flux limiter

When using a limited number of stationary flows and interfaces to model a real hydrodynamical system, an approximate Riemann solver tends to induce and preserve state discontinuities at the interfaces, even when in reality the state changes gradually. It that case, a linear interpolation would be a better mechanism to use. For that reason, Roe proposed an additional flux limiter for his approximate Riemann solver, by replacing (2.68) with:

$$\mathbf{F} = \frac{1}{2}\left(\mathbf{F}_L + \mathbf{F}_R - \sum_{c=1}^{3}(\sigma_c - (\sigma_c - \nu_c)\psi_c)\lambda_c a_c \mathbf{e}_c\right) \tag{2.74}$$

For $\psi_c = 0$, this equation reduces to Eq. (2.68). For $\psi_c = 1$, the equation yields:

$$\mathbf{F} = \frac{1}{2}\left(\mathbf{F}_L + \mathbf{F}_R + \sum_{c=1}^{3}\nu_c\lambda_c a_c \mathbf{e}_c\right) \tag{2.75}$$

Compared to (2.68), $-\sigma_c$ is replaced by ν_c, which is defined by:

$$\nu_c = \frac{\lambda_c}{\Delta r/\Delta t} \tag{2.76}$$

The CFL-condition makes sure that $|\lambda_c| < \Delta r/\Delta t$, so ν_c can take on any value between -1 and $+1$, depending on the relative strength of λ_c compared to $\Delta r/\Delta t$.

Through the parameter ψ_c, the flux limiter compares the state difference at an interface to the state difference at the neighbouring interface upwind (from where the flow is coming), using their projection coefficients a_c. If $a_c(0)$ is the projection coefficient on the central interface, $a_c(-1)$ the one on the left interface and $a_c(+1)$ the one on the right interface, the ratio χ_c can be defined as:

$$\chi_c = \frac{a_c(-\sigma_c)}{a_c(0)} \tag{2.77}$$

The dependence of ψ_c on χ_c determines the character of the flux limiter. A general form is given by:

$$\psi_c(\chi_c) = \begin{cases} 0 & \chi_c < 0 \\ \min(1, p_1 r) & 0 \le \chi_c \le 1 \\ \min(p_2, r) & \chi_c > 1 \end{cases} \tag{2.78}$$

The function min() determines the minimum value of its arguments. Based on numerical experience, Roe suggests using 'Superbee', which means that $p_1 = p_2 = 2$ (see Figure 2.3). This means that ψ_c can vary between 0 and 2. In this report, the values $p_1 = p_2 = 1.5$ of Paardekooper [11] are used, which tends to surpress very steep gradients a little more to prevent overshoots.

2.4 Numerical method

In this section, the numerical techniques and procedures are discussed that were used to perform the simulations for this report. All relevant parameters

that describe the macroscopic conditions of the spherical gas cloud are functions of the radius r and the time t. To numerically solve the spatial and temporal behaviour of the gas cloud, it is necessary to quantise both r and t.

The basic layout of each simulation is similar:

1. A limited number of spatial grid points are chosen to represent space.
2. At simulation time $t = 0$, for each grid point a primitive set of gas parameters ρ, P and v_r is chosen which represent the initial gas state.
3. The following steps are repeated until the final conditions of the simulation are reached.
   (a) The gravitational force is calculated from the mass density distribution on the grid.
   (b) At the grid points on the edge of the grid the boundary conditions are set.
   (c) The simulation time step Δt is determined.
   (d) The Euler equations are integrated over space and time to determine the change of state.
   (e) The gas state is updated.
   (f) The simulation time t is increased with Δt.

2.4.1 Grid model

The central part of the simulation is a fixed grid of N cells, covering a limited part of the domain of r. Each cell is identified by a lower index i, which runs from 1 to N. Figure 2.4 shows how the cells are positioned in real space. The cells are thin, spherical shells around a common origin. The N cells cover a radial distance from r_{min} to r_{max}, with $r_{min} < r_{max}$. A more mathematical approach is shown in Figure 2.5, where the same spherical cells are depicted as rectangular blocks on a straight line.

The simplest way to define the spatial layout of the grid is to divide the range from r_{min} to r_{max} into N cells with equal width Δr:

$$\Delta r = \frac{r_{max} - r_{min}}{N} \tag{2.79}$$

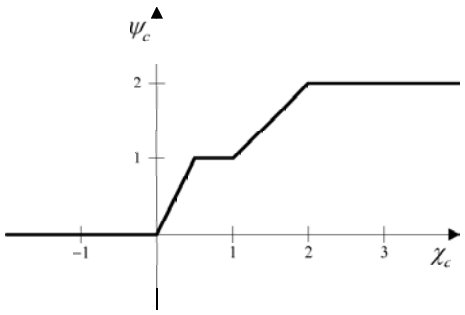

Figure 2.3: Transfer function of Superbee flux limiter.

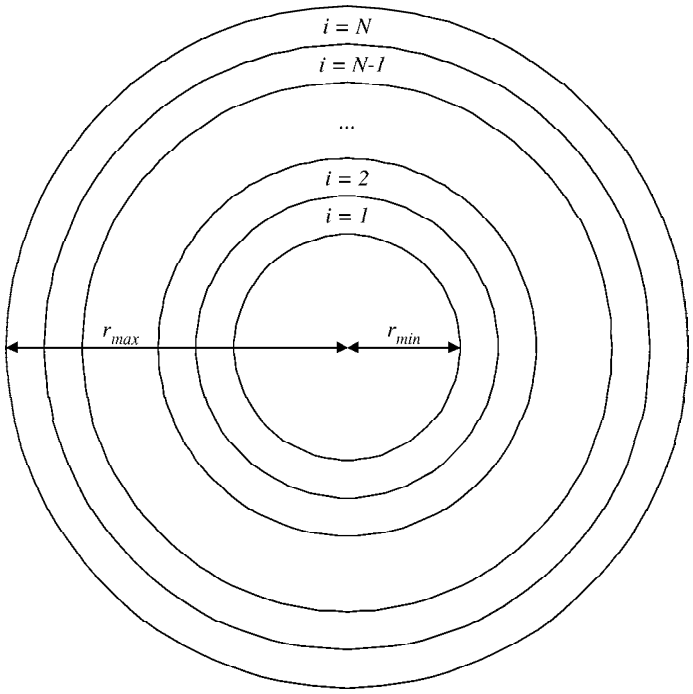

Figure 2.4: Spatial overview of N spherical cells around a common origin.

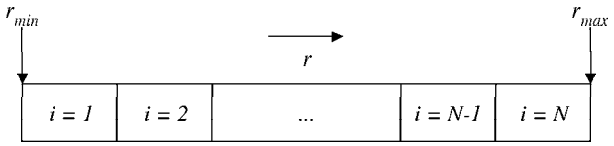

Figure 2.5: Schematic overview of the same N cells along a straight line.

The subscripted radius r_i is defined as the radius in the centre of cell i:

$$r_i = r_{min} + (i - \frac{1}{2})\Delta r \tag{2.80}$$

From this it follows that $r_{i-\frac{1}{2}}$ is the inner boundary and $r_{i+\frac{1}{2}}$ the outer boundary of cell i (thus $r_{\frac{1}{2}} = r_{min}$ and $r_{N+\frac{1}{2}} = r_{max}$).

It is assumed that the cells are so small (or thin) that the mass density ρ_i, pressure P_i and velocity $v_{r,i}$ change only little within each cell. It is common to look at ρ_i, pressure P_i, $v_{r,i}$ as the average state over the whole of cell i:

$$\begin{aligned}
\rho_i \approx \langle\rho\rangle_i &= \frac{1}{\Delta r}\int_{r_{i-\frac{1}{2}}}^{r_{i+\frac{1}{2}}} \rho \mathrm{d}r \\
P_i \approx \langle P\rangle_i &= \frac{1}{\Delta r}\int_{r_{i-\frac{1}{2}}}^{r_{i+\frac{1}{2}}} P \mathrm{d}r \\
v_{r,i} \approx \langle v_r\rangle_i &= \frac{1}{\Delta r}\int_{r_{i-\frac{1}{2}}}^{r_{i+\frac{1}{2}}} v_r \mathrm{d}r
\end{aligned} \tag{2.81}$$

The grid represents the state of the gas at one single instant of time t. To update the state one time step Δt later, the Euler equations need to be numerically integrated. The only requirement on Δt is that it satisfies the CFL-condition (see Section 2.3.2) for all cells(!). In general, Δt is not a constant time step. A superscripted t^n indicates the time after n state updates. The mass density in cell i after state update n is noted as ρ_i^n, etc.

2.4.2 Initial configurations

Every simulation starts with setting an initial configuration of the grid, which represents the gas state at simulation time $t = t^0 = 0$. It is the initial gas state that gets developed in time by the numerical model, by integration of the Euler equations. By choosing an initial configuration, the scope of the simulation is determined. Although the cell contents should be averages over the whole cell, the initial values are chosen to be the gas states in the centre of the cells at $r = r_i$, which is a reasonable approximation. In this report, three types of initial configurations are used.

The top-hat cloud is the most simple initial configuration. It simulates a high mass density cloud in a low mass density environment. Both the cloud and the environment are in pressure equilibrium and in rest relative to the origin at $r = 0$. Because of its simplicity, many authors have used this configuration in their gravitational collapse models, although it is very artificial. The top-hat cloud is expected to collapse during simulation, or at least move from its initial configuration, because it is far from hydrostatic equilibrium. The grid is split into two parts, depending on the radius of the cloud and the additional radius of the environment. On the inner part, the cloud cells are all set to the high mass density ρ_h, together with the global pressure P and velocity $v_r = 0$. The radius is usually set to (a multiple of) the Jeans radius, or is determined by choosing a total mass of the cloud. On the outer part, the cloud cells are all set to the low mass density ρ_l, together with the same global P and $v_r = 0$. The three main reasons for the presence of an environment is to define an outer boundary for

the cloud, to specify its mass density, to provide the cloud with some space to possibly expand into and to define an environment into which pressure waves can travel radially outward (after which they leave the grid).

Hydrostatic equilibrium is an initial configuration which is a bit more complicated to set up. With a cloud in hydrostatic equilibrium at all points in the cloud, the gravitational force inwards is counteracted by the (negative) pressure gradient outwards. The hydrostatic equilibrium is expected to remain stationary during simulation. Many authors use hydrostatic equilibrium as an initial configuration, after which they perturb the system by increasing the cloud mass density and pressure or the external pressure by some factor (often $\sim 10\%$). This will make the cloud move, possibly collapse. Hydrostatic equilibrium is set up by choosing a central mass density ρ_c and pressure P_c for the innermost cell of the grid, while central velocity $v_{r,c} = 0$. Using these values with the method described in Section 2.4.7 yields a hydrostatic equilibrium. This way, it is not possible to specify a fixed cloud mass beforehand. This can only be done by trial and error.

The stationary flow is an initial configuration which is also a bit complicated to set up, although very similar to the hydrostatic equilibrium. A stationary flow is expected to remain stationary during simulation. The stationary flow is set up by choosing a central mass density ρ_c, pressure P_c and central velocity $v_{r,c} \neq 0$ for the innermost cell of the grid. Using these values with the method described in Section 2.4.7 yields a stationary flow. Again, it is not possible to specify a total mass beforehand. This can only be done by trial and error.

2.4.3 Boundary conditions

Because the grid is limited in spatial dimensions, it is necessary to specify the behaviour of the grid at the boundaries r_{min} and r_{max}. It is common practice to add one or more so-called ghost cells at each boundary, which provide some desired boundary behaviour during simulation. For this report, one ghost cell is added at both r_{min} and r_{max}, indexed with $i = 0$ and $i = N + 1$. Two types of boundary conditions are used.

The outer boundary should allow for mass and waves to leave the grid without reflection, while inflow of matter should also be allowed. This type of boundary condition is called an inflow/outflow boundary condition. According to Paardekooper [11], Section 4.4, this is done by simply rewriting the initial boundary state into the ghost cell at every time step of the simulation.

For simulations with $r_{min} = 0$, it is prohibited for matter to flow through the boundary at $i = \frac{1}{2}$, because at $r = 0$ the surface area ($\sim r^2$) of the boundary is zero. Any matter trying to pass should reflect back onto the grid, so a reflecting boundary condition is needed. This can be done by making cell 0 a mirror copy of cell 1. All scalar state parameters, like mass density and pressure (and gravitational potential), are copied directly. All vector state parameters, like velocity and gravitational force, are copied with a minus sign. Special care must be taken in the Roe solver to handle $r = 0$ correctly. The net flux through the boundary at $i = \frac{1}{2}$ must always be zero (this can be hard-coded in the Roe solver).

For simulations with $r_{min} \geq 0$, an inflow boundary condition can be used on the boundary at $i = \frac{1}{2}$. This could mimic a central object (e.g. a star) which injects mass onto the grid (e.g. a stellar wind). As above, this is done by simply

rewriting the initial boundary state into the ghost cell at every time step of the simulation. However, it should be noted that any waves that run backwards towards the centre do not get reflected, which is unphysical behaviour. Therefore, it is best to make the outflow supersonic, so that all signal (wave) velocities are greater than zero. Whether this is realistic is not discussed in this report, as the supersonic wind is only used as a test case for model functionality, not for simulating true stellar winds.

2.4.4 Integration of the Euler equations

When the grid is defined and initialised, the boundary conditions are set and the time step is determined, it is time for the Euler equations to be integrated. For this, the Roe method in Section 2.3 is used. The cell boundaries are the interfaces, while inside each cell, a stationary flow is assumed. The use of the grid fixes the location of all (cell) interfaces in space. As a consequence, a shock (state discontinuity) can only appear at a cell boundary.

Using the Roe method means numerical integration of Equations (2.53)-(2.55). Before giving the steps how to do this, a final bit of theory is needed.

Gauss theorem

Using the Gauss theorem on (2.53), it follows that over any space-time interval $\Delta r, \Delta t$ the following must be true:

$$\oint_{\Delta r, \Delta t} (\mathbf{W} \mathrm{d}r + \mathbf{F} \mathrm{d}t) = 0 \tag{2.82}$$

Applying this to one grid cell during one time step, following the direction of

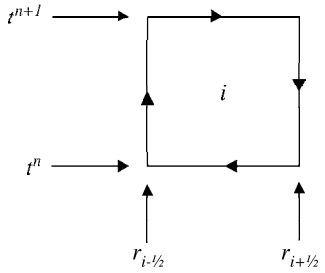

Figure 2.6: Schematic overview of one grid cell during one state update in space-time.

integration in Figure 2.6, gives:

$$\int_{r_{i-\frac{1}{2}}}^{r_{i+\frac{1}{2}}} \mathbf{W}(r, t^{n+1}) \mathrm{d}r - \int_{r_{i-\frac{1}{2}}}^{r_{i+\frac{1}{2}}} \mathbf{W}(r, t^n) \mathrm{d}r + \int_{t^n}^{t^{n+1}} \mathbf{F}(r_{i-\frac{1}{2}}, t) \mathrm{d}t - \int_{t^n}^{t^{n+1}} \mathbf{F}(r_{i+\frac{1}{2}}, t) \mathrm{d}t = 0 \tag{2.83}$$

The state in cell i at time n is an approximate average over space, just like (2.81):

$$\mathbf{W}_i^n \approx \langle \mathbf{W}^n \rangle_i = \frac{1}{\Delta r} \int_{r_{i-\frac{1}{2}}}^{r_{i+\frac{1}{2}}} \mathbf{W}^n \mathrm{d}r \tag{2.84}$$

In the same manner, the flux at cell boundary $i + \frac{1}{2}$ at time $n + \frac{1}{2}$ can be seen as an approximate average over time:

$$\mathbf{F}_{i+\frac{1}{2}}^{n+\frac{1}{2}} \approx \langle \mathbf{F}_{i+\frac{1}{2}} \rangle^{n+\frac{1}{2}} = \frac{1}{\Delta t} \int_{t^n}^{t^{n+1}} \mathbf{F}_{i+\frac{1}{2}} \mathrm{d}t \tag{2.85}$$

Using (2.84) and (2.85), (2.83) can be approximated by:

$$\begin{aligned} &\Delta r \left(\mathbf{W}_i^{n+1} - \mathbf{W}_i^n \right) + \Delta t \left(\mathbf{F}_{i-\frac{1}{2}}^{n+\frac{1}{2}} - \mathbf{F}_{i+\frac{1}{2}}^{n+\frac{1}{2}} \right) \approx 0 \quad \Rightarrow \\ &\mathbf{W}_i^{n+1} \approx \mathbf{W}_i^n - \frac{\Delta t}{\Delta r} \left(\mathbf{F}_{i+\frac{1}{2}}^{n+\frac{1}{2}} - \mathbf{F}_{i-\frac{1}{2}}^{n+\frac{1}{2}} \right) \end{aligned} \tag{2.86}$$

This equation basically says that the new state is equal to the old state plus the amount that is transported in or out by the net flux through the boundaries. This is the signature of a conservative numerical scheme.

Roe solver

The Roe solver is the central part of the hydrodynamical model. It calculates approximations for the time-averaged cell boundary fluxes $\mathbf{F}_{i+\frac{1}{2}}^{n+\frac{1}{2}}$ and $\mathbf{F}_{i-\frac{1}{2}}^{n+\frac{1}{2}}$, based on the Roe method in Section 2.3, so that a state update can be calculated from the former state $\mathbf{W}_i^n$ by using (2.86).

Following the Roe method, the first step is to integrate (2.55) from the cell centre at r_i to the cell boundaries at $r_{i-\frac{1}{2}}$ and $r_{i+\frac{1}{2}}$ using stationary extrapolation (finding the stationary solution). This yields the states $[\mathbf{W}_L]_{i+\frac{1}{2}}^n, [\mathbf{W}_R]_{i+\frac{1}{2}}^n$ left and right of each boundary $i + \frac{1}{2}$ (excluding the outer boundaries of the ghost cells). From these the fluxes $[\mathbf{F}_L]_{i+\frac{1}{2}}^n, [\mathbf{F}_R]_{i+\frac{1}{2}}^n$ are determined.

The second step is to determine for each boundary the weighted averages of the velocity $\widetilde{v_r}_{i+\frac{1}{2}}^n$ and the enthalpy $\widetilde{H}_{i+\frac{1}{2}}^n$. Then the eigenvalues $[\lambda_c]_{i+\frac{1}{2}}^n$, eigenvectors $[\mathbf{e}_c]_{i+\frac{1}{2}}^n$ and projection coefficients $[a_c]_{i+\frac{1}{2}}^n$ and $[b_c]_{i+\frac{1}{2}}^n$ can be calculated.

The third step is using (2.75) to determine the approximate boundary flux $\mathbf{F}_{i+\frac{1}{2}}^{n+\frac{1}{2}}$ for each boundary. After following these steps, the state $\mathbf{W}_i^n$ is updated to a new state $[\mathbf{W}_1]_i^{n+1}$ using (2.86).

Source term integration

Until now, the integration of the source term in (2.54) did not receive any attention, but it cannot be left out. The updated state $[\mathbf{W}_1]_i^{n+1}$ from the section above needs to be corrected for this. The following correction is accurate to second order (see Eulderink&Mellema, Appendix C):

$$[\mathbf{W}_2]_i^{n+1} = [\mathbf{W}_1]_i^{n+1} + \Delta t \; \mathbf{S}_i^n \tag{2.87}$$

$$\mathbf{W}_i^{n+1} = [\mathbf{W}_1]_i^{n+1} + \frac{\Delta t}{2} \left(\mathbf{S}_i^n + [\mathbf{S}_2]_i^{n+1} \right) \tag{2.88}$$

First, the source term $\mathbf{S}_i^n$ needs to be determined from the former state $\mathbf{W}_i^n$. Logically, this needs to be done before the state gets updated in the Roe solver. Next, an approximation $[\mathbf{W}_2]_i^{n+1}$ of the new state is calculated by integrating $\mathbf{S}_i$ to first order (2.87). The source term $[\mathbf{S}_2]_i^{n+1}$, calculated from $[\mathbf{W}_2]_i^{n+1}$ approximates the new source term. The final step is to average the source terms $\mathbf{S}_i$ and $[\mathbf{S}_2]_i^{n+1}$ and integrate the average to yield a second order accurate state update $\mathbf{W}_i^{n+1}$ (2.88).

Alternative stationary extrapolation

Because stationary extrapolation is computationally expensive, a less expensive method was implemented in the Roe solver. Instead of finding a stationary solution, (2.53) is integrated directly to first order to find the interface fluxes:

$$\begin{aligned}[\mathbf{F}_L]_{i+\frac{1}{2}}^n &= \mathbf{F}_i^n + \frac{\Delta r}{2}\mathbf{S}_i^n \\ [\mathbf{F}_R]_{i-\frac{1}{2}}^n &= \mathbf{F}_i^n - \frac{\Delta r}{2}\mathbf{S}_i^n \end{aligned} \tag{2.89}$$

These first order accurate fluxes will still yield a second order accurate state.

However, by direct integration of 2.53), the interface states $\mathbf{W}_L, \mathbf{W}_R$ are no longer available. Instead, the central states $\mathbf{W}_i^n$ are used for calculation of the weighted averages of the velocity and the enthalpy. This approximation amounts to the assumption that the cell contains a stationary flow.

2.4.5 Radial coordinate transformation

During a gravitational collapse, the inner part of the grid will be the most interesting part to examine. Assuming that $r_{min} = 0$ is a valid option, the gas parameters are expected to change the most when approaching $r = 0$. It is therefore useful to have narrower cells on the inner part of the grid, while the outer part might do with larger, but fewer cells. This can be done by transforming the radial coordinate r into a new 'distance' coordinate ℓ:

$$r \to \ell = \ell(r) \quad \Leftrightarrow \quad \ell \to r = r(\ell) \tag{2.90}$$

The inverse transformation from ℓ to r must also exist, for this defines a unique relation between r and ℓ. Thus, $\ell(r)$ should be a continuous, differentiable, and strictly monotonic function on the domain of r. The function $\ell(r)$ can be chosen freely, as long as it meets these requirements. For practical purposes, it is easiest to choose a function $\ell(r)$ which increases when r increases, so that $\ell_{min} \equiv \ell(r_{min}) < \ell_{max} \equiv \ell(r_{max})$. Note that, although $r(\ell)$ can be expressed in *meters* or some related distance units, ℓ can not (in general). The cell width is now given by:

$$\Delta\ell = \frac{\ell_{max} - \ell_{min}}{N} \tag{2.91}$$

The distance ℓ_i is defined as the the value of ℓ in the middle of cell i:

$$\ell_i = \ell_{min} + (i - \frac{1}{2})\Delta\ell \quad \Rightarrow \quad r_i \equiv r(\ell_i) \tag{2.92}$$

The radius r_i is no longer defined by (2.80), unless $\ell(r) = r$. The width Δr of any cell i is no longer a constant (unless $\ell(r) = r$), but is given by:

$$\Delta r_i = r_{i+\frac{1}{2}} - r_{i-\frac{1}{2}} \tag{2.93}$$

From differential calculus it follows that:

$$\mathrm{d}r = \mathrm{d}r(\ell) = \frac{\mathrm{d}r(\ell)}{\mathrm{d}\ell}\mathrm{d}\ell \equiv r'(\ell)\mathrm{d}\ell \quad \Rightarrow \tag{2.94}$$

$$\frac{\partial}{\partial r} = \frac{1}{r'(\ell)}\frac{\partial}{\partial \ell}, \tag{2.95}$$

$$v_r = \frac{\partial r(\ell)}{\partial t} = r'(\ell)\frac{\partial \ell}{\partial t} = r'(\ell)v_\ell \tag{2.96}$$

Here, $r'(\ell)$ is short notation for the first derivative of $r(\ell)$ to ℓ. Short notation for the second derivative is $r''(\ell)$, etc. Again, note that, although $v_r(\ell)$ can be expressed in *meters per second* or some related velocity units, v_ℓ can not (in general). From (2.95), an approximation can be made for Δr_i:

$$\Delta r_i \approx r'(\ell_i)\Delta\ell \equiv r'_i\Delta\ell \tag{2.97}$$

Using the transformation rules above, all equations containing r can be rewritten in terms of ℓ.

Because of the generalised Roe method by Eulderink&Mellema [4], the steps taken to solve the Euler equations do not change, only the formulas concerning the Roe solver will be modified slightly. In Section A.4, the Euler equations are given in terms of the new radial coordinate ℓ:

$$\frac{\partial}{\partial t}\left(r^2r'\rho\right) + \frac{\partial}{\partial \ell}\left(r^2r'\rho v_\ell\right) = 0 \tag{2.98}$$

$$\frac{\partial}{\partial t}\left(r^2r'\rho v_\ell\right) + \frac{\partial}{\partial \ell}\left(r^2r'\left[\rho {v_\ell}^2 + \frac{P}{r'^2}\right]\right) = r^2r'\left[\frac{2P}{rr'} - \frac{r''}{r'}\left\{\rho {v_\ell}^2 + \frac{P}{r'^2}\right\} - \frac{\rho}{r'}\frac{\partial\Phi}{\partial r}\right] \tag{2.99}$$

$$\frac{\partial}{\partial t}\left(r^2r'e\right) + \frac{\partial}{\partial \ell}\left(r^2r'\left[e+P\right]v_\ell\right) = -r^2r'\rho r' v_\ell\frac{\partial\Phi}{\partial r} \tag{2.100}$$

The total energy density e of the gas is given by:

$$e = \frac{1}{2}\rho r'^2 {v_\ell}^2 + \frac{P}{\Gamma - 1} \tag{2.101}$$

Using the vector notation from Section 2.3, the state, flux and source vectors become:

$$\mathbf{W} = r^2r'\begin{pmatrix}\rho\\ \rho v_\ell\\ e\end{pmatrix}, \quad \mathbf{F} = r^2r'\begin{pmatrix}\rho v_\ell\\ \rho {v_\ell}^2 + \frac{P}{r'^2}\\ \left[e+P\right]v_\ell\end{pmatrix},$$

$$\mathbf{S} = r^2r'\begin{pmatrix}0\\ \frac{2P}{rr'} - \frac{r''}{r'}\left\{\rho {v_\ell}^2 + \frac{P}{r'^2}\right\} - \frac{\rho}{r'}\frac{\partial\Phi}{\partial r}\\ -\rho r' v_\ell\frac{\partial\Phi}{\partial r}\end{pmatrix} \tag{2.102}$$

The new eigenvalues and eigenvectors of the Jacobian (see Section 2.3.1) are derived in Section B.1 and take the following form:

$$\lambda_1 = v_\ell, \qquad \lambda_2 = v_\ell + \frac{c_s}{r'}, \qquad \lambda_3 = v_\ell - \frac{c_s}{r'} \tag{2.103}$$

$$\mathbf{e}_1 = \begin{pmatrix} 1 \\ \lambda_1 \\ \frac{1}{2} r'^2 {v_\ell}^2 \end{pmatrix}, \quad \mathbf{e}_2 = \begin{pmatrix} 1 \\ \lambda_2 \\ \frac{e+P}{\rho} + r' v_\ell c_s \end{pmatrix}, \quad \mathbf{e}_3 = \begin{pmatrix} 1 \\ \lambda_3 \\ \frac{e+P}{\rho} - r' v_\ell c_s \end{pmatrix} \tag{2.104}$$

The sound speed c_s is still given by (2.11). The new projection coefficients b_c are:

$$\begin{aligned} b_1 &= \frac{\Gamma - 1}{{c_s}^2} \left(\left[\frac{e+P}{\rho} - r'^2 {v_\ell}^2 \right] \Delta F_1 + r'^2 V_\ell \Delta F_2 - \Delta F_3 \right) \\ b_2 &= \frac{\Gamma - 1}{2{c_s}^2} \left(\frac{1}{2} r'^2 {v_\ell}^2 \Delta F_1 - r'^2 v_\ell \Delta F_2 + \Delta F_3 \right) + \frac{r'}{2c_s} \left(v_\ell \Delta F_1 - \Delta F_2 \right) \\ b_3 &= \frac{\Gamma - 1}{2{c_s}^2} \left(\frac{1}{2} r'^2 {v_\ell}^2 \Delta F_1 - r'^2 v_\ell \Delta F_2 + \Delta F_3 \right) - \frac{r'}{2c_s} \left(v_\ell \Delta F_1 - \Delta F_2 \right) \end{aligned} \tag{2.105}$$

For λ_c, $\mathbf{e}_c$ and b_c, r' needs to be evaluated at the interface. The weight factor K for the Roe averages is now defined by $K^2 = r^2 r' \rho$. The CFL-condition has the following form:

$$\Delta t = \zeta \frac{\Delta \ell}{\lambda_{max}} \tag{2.106}$$

The interpolation parameters ν_c are given by:

$$\nu_c = \frac{\lambda_c}{\Delta \ell / \Delta t} \tag{2.107}$$

For this report, the used transformation is a power law:

$$r(\ell) = \ell^{1 \,|\, \alpha} \quad \Leftrightarrow \quad \ell(r) = r^{\frac{1}{1+\alpha}}, \quad \alpha \geq 0 \tag{2.108}$$

Choosing this form prevents the introduction of some intrinsic distance scale. Differentiating r to ℓ gives:

$$r'(\ell) = (1+\alpha)\ell^\alpha, \quad r''(\ell) = \alpha(1+\alpha)\ell^{\,1 \,|\, \alpha} \tag{2.109}$$

Assuming $\ell_{min} = \Delta\ell/2$, so that $\ell_i = i\Delta\ell$, the ratio ξ_i of radial sizes Δr_i to Δr_1 is approximated by:

$$\begin{aligned} \xi_i \equiv \frac{\Delta r_i}{\Delta r_1} \approx \frac{r'_i \Delta \ell}{r'_1 \Delta \ell} = \frac{(1+\alpha) {l_i}^\alpha}{(1+\alpha) {l_1}^\alpha} = \left(\frac{l_i}{l_1} \right)^\alpha = \left(\frac{i\Delta\ell}{\Delta\ell} \right)^\alpha = i^\alpha \quad \Rightarrow \\ \alpha \approx \frac{\ln(\xi_i)}{\ln(i)} \end{aligned} \tag{2.110}$$

This shows that the radial size of the cells increases with increasing i.

2.4.6 Gravitational force and potential

Calculation of the gravitational force F_i is simple with the use of the numerical analogons of (2.24) and (2.27). First, the enclosed mass excess M_i is calculated by using:

$$\begin{aligned} M_1 &= 0, \\ M_i &= \sum_{a=1}^{i-1} 4\pi r_a^2[\rho_a - \rho_{N+1}]\Delta r_a = \sum_{a=1}^{i-1} 4\pi r_a^2[\rho_a - \rho_{N+1}]r'_a\Delta\ell \end{aligned} \tag{2.111}$$

Here, (2.97) was used. The mass density ρ_{N+1} in the outer boundary cell of the grid is taken to be the mass density ρ_{env} of the environment. Basically, M_i contains the sum of the mass within cells 1 to $i-1$, so M_1 must be zero. Next, the gravitational force F_i is calculated by using:

$$F_i = -\frac{GM_i}{{r_i}^2} \tag{2.112}$$

According to (2.28), numerical integration of F_i gives the gravitational potential Φ_i:

$$\begin{aligned} \Phi_{N+1} &= -\frac{GM_{N+1}}{r_{N+1}}, \\ \Phi_i &= \Phi_{N+1} + \sum_{a=i}^{N} F_a\Delta r_a = \Phi_{N+1} + \sum_{a=i}^{N} F_a r'_a\Delta\ell \end{aligned} \tag{2.113}$$

Integration of Φ_{N+1} can be done analytically, because $M = M_{N+1}$ for $r \geq r_{N+1}$ (it is assumed that $\rho = \rho_{env} = \rho_{N+1}$ for $r \geq r_{N+1}$).

2.4.7 Stationary solutions

According to Appendix B.2, it is (in theory) possible to find a configuration of gas parameters that stays constant in time. In other words, when starting out with a special set of functions $\rho(r, t = 0)$, $P(r, t = 0)$ and $v_r(r, t = 0)$ that together form a stationary solution, these functions do not change as a function of time, so $\rho(r, t = T) = \rho(r, t = 0)$, $P(r, t = T) = P(r, t = 0)$ and $v_r(r, t = T) = v_r(r, t = 0)$ for any value of T.

Appendix B.2 contains the derivation of a set of three parameters, $\{D, B, \kappa\}$, that are constants in both space and time. The mass flux D is given by:

$$D = r^2 r' \rho v_\ell = r^2 \rho v_r \tag{2.114}$$

Bernoulli's constant B is the sum of the enthalpy H and the gravitational potential Φ and is given by:

$$B = H + \Phi = \frac{e+P}{\rho} + \Phi = \frac{1}{2} r'^2 {v_\ell}^2 + \frac{\Gamma}{\Gamma - 1}\frac{P}{\rho} + \Phi \tag{2.115}$$

The total energy density e is defined in (2.33). The constant κ gives the adiabatic relation between ρ and P:

$$\kappa = \frac{P}{\rho^\Gamma} \tag{2.116}$$

It is easy to see that for a physical solution ($\rho > 0$, $P > 0$ and v_r any real value), it follows that $H = B - \Phi > 0$ and $\kappa > 0$ must be true, while D can have any real value.

All stationary solutions have a unique set of values for $\{D, B, \kappa\}$. However, not all sets $\{D, B, \kappa\}$ lead to possible solutions (see Eulderink&Mellema [4], Section 6.3). One way to check whether any solution exists for a given set $\{D, B, \kappa\}$, and to find this solution, is to combine (2.114), (2.115) and (2.116) into a single function f:

$$f \equiv \frac{D^2}{2r^4} + \frac{\Gamma\kappa}{\Gamma - 1}\rho^{\Gamma+1} - (B - \Phi)\rho^2 = 0 \tag{2.117}$$

Here, P and v_r are eliminated in favour of ρ. The problem has now been transformed into finding the roots of f. Algebraic expressions for the roots of f can only be found when $D = 0$ (equivalent with $v_r = 0$). In that case:

$$\begin{aligned} f &= \left(\frac{\Gamma\kappa}{\Gamma - 1}\rho^{\Gamma-1} - (B - \Phi)\right)\rho^2 = 0 \quad \Rightarrow \\ \rho &= \left(\frac{\Gamma - 1}{\Gamma}\frac{B - \Phi}{\kappa}\right)^{\frac{1}{\Gamma-1}} \equiv \rho_{D=0} \end{aligned} \tag{2.118}$$

Note that $\rho = 0$ is also a solution, but lies outside the domain $\rho > 0$.

Examining f for $D \neq 0$, it follows that $f \to D^2/(2r^4)$ for $\rho \to 0$ and $f \to +\infty$ for $\rho \to \infty$. Both limits are greater than zero, so if any roots are to be found, the minimum of f must be less than or equal to zero. The minimum of f is found using:

$$\begin{aligned} \frac{\partial f}{\partial \rho} &= \frac{\Gamma(\Gamma + 1)\kappa}{\Gamma - 1}\rho^{\Gamma} - 2(B - \Phi)\rho = 0 \quad \Rightarrow \\ \rho &= \left(\frac{2(\Gamma - 1)}{\Gamma(\Gamma + 1)}\frac{B - \Phi}{\kappa}\right)^{\frac{1}{\Gamma-1}} \equiv \rho_{min} \end{aligned} \tag{2.119}$$

With $D \neq 0$, $f(\rho_{min}) < 0$ corresponds to two roots, $f(\rho_{min}) = 0$ with one root and $f(\rho_{min}) > 0$ with zero roots. Eulderink&Mellema [4] (Section 6.3) state that a single root corresponds to a solution with exact sonic velocity ($|v_r| = c_s$). With two roots, the lower value corresponds with a supersonic solution ($|v_r| > c_s$) while the higher value corresponds to a subsonic solution ($|v_r| < c_s$). They also state that a stationary solution cannot contain a transition from a subsonic flow to a supersonic flow or reverse. At such a transition, the sonic point is crossed and a shockwave appears. This makes κ no longer a constant (see Section 2.1.1).

For testing purposes, it is best to stay away from the sonic point and limit the search for stationary solutions to pure supersonic or subsonic solutions. The special case $D = 0$ is clearly a subsonic solution, for $v_r = 0$ for all r. For $D \neq 0$, it can be shown that the supersonic root ρ_{sup} and the subsonic root ρ_{sub} are limited to the following domains:

$$0 < \rho_{sup} < \rho_{min} < \rho_{sub} < \rho_{D=0} \tag{2.120}$$

When ρ, P, v_r and Φ are known at some radius r, (2.114), (2.115) and (2.116) can be used to determine $\{D, B, \kappa\}$. The next step would be calculating the roots of f for new values of r, which gives ρ at the new r. After that, (2.114) and (2.116) gives v_r and P at the new r. However, there are several things which make this approach more difficult:

- Φ is the gravitational potential and includes self-gravity. Therefore, Φ depends on the actual value of ρ at all r. So, ρ should be known before ρ can be calculated.
- Even if Φ is known beforehand, there exists no algebraic expression for the roots of f when $D \neq 0$.
- It follows that f can have zero, one or two roots. With two roots, a correct choice must be made between the two possible values of ρ.

The following numerical procedure was used to handle these difficulties and find a self-consistent stationary solution:

1. Choose ρ_1, P_1 and $v_{r,1}$ at radius r_1. Calculate the sound speed c_s from ρ_1 and P_1 using (2.11). Check whether $v_{r,1}$ is subsonic or supersonic, as this will be the sonic state for the whole stationary solution.
2. Choose some initial mass density distribution ρ_i which includes the point $\{r_1, \rho_1\}$. (For this report, a $\rho \sim r^{-2}$ distribution was used.) Calculate the gravitational potential Φ_i from r_i and ρ_i using (2.111)-(2.113).
3. Calculate D, B and κ from r_1, ρ_1, P_1, $v_{r,1}$ and Φ_1 using (2.114)-(2.116).
4. Iterate towards a self-consistent mass density distribution ρ_i. This is done by repeating the following steps (for this report 200 times):
   (a) For each i, calculate the correct root of f using D, B, κ, r_i, Φ_i and the sonic state information found in step 1. This gives a new mass density ρ_i. The iteration procedure for finding the root follows below.
   (b) For each i, update the mass density ρ_i by taking an weighted average of the new mass density just found and the previous mass density. (For this report, the update used was $\rho = (\rho_{new} + 7\rho_{old})/8$.) This slows down the iteration, but makes it more stable.
   (c) For each i, update P_i and $v_{r,i}$ from D, κ, r_i and the updated ρ_i using (2.114) and (2.116).
   (d) Update Φ_i from r_i and the updated ρ_i using (2.111)-(2.113).
   (e) Update B from r_1 and the updated ρ_1, P_1, $v_{r,1}$ and Φ_1 using (2.115).

The following numerical procedure was used to find the correct root of f in step 4a above:

1. Check if $B - \Phi_i > 0$. If not, the iteration towards a self-consistent mass density distribution failed.
2. Check if $D = 0$. If so, calculate the root ρ_i directly using (2.118) and skip the steps below.
3. Otherwise, calculate ρ_{min} from B, κ and Φ_i using (2.119). Calculate f from D, B, κ, r_i, ρ_{min} and Φ_i using (2.117). Check if $f < 0$. If not, the iteration towards a self-consistent mass density distribution failed.

4. Iterate towards the correct root of f using the bisection method (e.g. see Press et al. [12], Section 9.1). (For this report, 100 bisection steps were performed for each root.) Good starting values are $\rho_1 = 0$ and $\rho_2 = \rho_{min}$ when the flow is supersonic or $\rho_1 = \rho_{min}$ and $\rho_2 = \rho_{D=0}$ when the flow is subsonic.

Bisection might be slow compared to other methods, but very stable. The Newton-Raphson method (Press et al. [12], Section 9.4) was also tried, but proved to be too unstable.

Chapter 3

Results

3.1 Test results

In this section, the results of three test problems are presented. These test problems are performed to gain some insight in the stability and accuracy of the model.

3.1.1 Pressure equilibrium without gravity

In this test problem the time evolution of a top-hat mass density distribution in rest is simulated. Special for this test problem is that both the gravitational force and potential are both set to zero and that the mass density distribution is in pressure equilibrium. Because there are no physical mechanisms to induce movement in the gas, it is expected that the simulated mass density distribution will stay in rest over many free-fall times. However, due to limited numerical precision and limited precision of the numerical method used, the simulation will inevitably introduce changes in the configuration away from the initial setup. Preferably, these changes will be small and will lead to a stable configuration.

The basic setup is a dense cloud of 1 Jeans mass with temperature 1 K, embedded in a less dense environment with temperature 10^4 K. The pressure is 3.50×10^3 cm^{-3} $K = 4.83 \times 10^{-14}$ N m^{-2} everywhere. These values are close to values measured for a protostellar cloud in the interstellar medium. The top-hat cloud is by no means a stable mass density distribution in the presence of self-gravity. Because of the top-hat cloud, there is a mass density discontinuity at $r = R_J$. The grid runs from 0-2 Jeans radii, divided into 100 cells with $\alpha = 0$. On the inner boundary a reflective boundary condition is set, while on the outer bounday an in/outflow boundary condition is set. The simulation time

is 2 free-fall times. A summary of the relevant simulation parameters:

$$\Gamma = \frac{5}{3}, \qquad \mu = 1$$
$$N = 250, \qquad \alpha = 0$$
$$M_J = 1.56\ M_\odot, \qquad R_J = 3.36 \times 10^4\ AU$$
$$t_{ff} = 8.70 \times 10^5\ yr, \qquad t_{sim} = 1.74 \times 10^6\ yr$$
$$R_{min} = 0\ AU, \qquad R_{max} = 2.01 \times 10^5\ AU$$
$$R_{cl} = 3.36 \times 10^4\ AU, \qquad R_{cl} = 6.71 \times 10^4\ AU$$
$$\rho_{cl} = 5.86 \times 10^{-18}\ kg\ m^{-3}, \qquad \rho_{env} = 5.86 \times 10^{-22}\ kg\ m^{-3}$$
$$P_{cl} = 4.83 \times 10^{-14}\ N\ m^{-2}, \qquad P_{env} = 4.83 \times 10^{-14}\ N\ m^{-2}$$
$$v_{r,cl} = 0\ m\ s^{-1}, \qquad v_{r,env} = 0\ m\ s^{-1}$$

During the simulation of 2 free-fall times, there was no detectable change in the mass density ρ or the pressure P within a factor of 10^{-5} of the initial value over the whole grid. The velocity v_r fluctuates around zero with a largest deviation of less than $10^{-11}\ m\ s^{-1}$, which seems to make the velocity fluctuations insignificant. Figure 3.1 shows the velocity deviation Δv_r from initial conditions during the simulation. From this figure, it can be seen that the low mass density area $r > R_{cl}$ shows relatively more numerical fluctuations than the high mass density area $r < R_{cl}$. Around the discontinuity $r = R_{cl}$, numerical diffusion starts a small mass flow outwards. Because the small velocity deviations do not induce significant changes in the mass density or the pressure, it seems that these effects can be ignored.

A second test run was performed with the same simulation parameters, except that the number of cells was increased to $N = 250$. This means that the width of all grid cells is 2.5 times as small as before. The results are quite different from the simulation with $N = 100$. In the innermost cells near $r = 0$, ρ, P and v_r change significantly. Immediately after the simulation starts, in the innermost cell, ρ and P drop to $\sim 73\%$ and $\sim 61\%$ of their initial values, while v_r increases to $\sim 60\ m\ s^{-1}$. A few neighbouring cells are effected as well in ρ, P and v_r, but far less than the innermost cell. Considering the rest of the grid, the largest velocity deviation is $\sim 0.1\ m\ s^{-1}$. Figures 3.2-3.4 show the deviations in mass density $\Delta\rho$, pressure ΔP and velocity Δv_r from initial conditions during the simulation, excluding the 10 innermost grid cells. From this figure, it can be seen that some flow is bouncing between the boundaries of the high mass density area $r < R_{cl}$. The mass density is also showing a deviation around the discontinuity $r = R_{cl}$, probably caused by diffusion into the low mass density area. Both these effects change the gas state on the grid up to a few percent in ρ and P and $\sim 1\ m\ s^{-1}$, which is significantly less than the deviations on the most inner part of the grid.

A third test run was performed to see how the introduction of a new radial coordinate ℓ (with $r(\ell) = \ell^{1+\alpha}$) effects the results above. The simulation parameters are the same as the first run, except that $\alpha = \ln(10)/\ln(N)$. This means that the most inner cell of the grid is 10 times as small as the most outer cell (see (2.110)). The results are very similar to the results of $N = 250$ and $\alpha = 0$. The innermost cell shows the largest deviations in ρ, P and v_r, while some wave is bouncing the high mass density area $r < R_{cl}$. Also, the diffusion

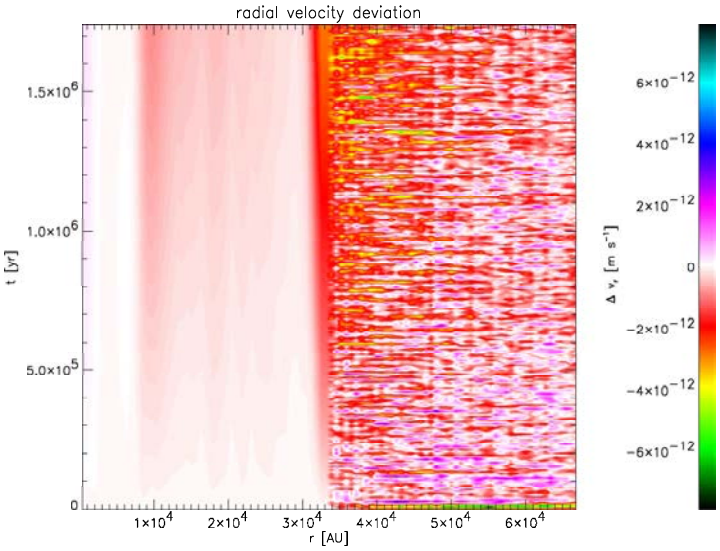

Figure 3.1: Velocity deviation Δv_r from initial pressure equilibrium configuration (without self-gravity) during simulation with $N = 100$ and $\alpha = 0$.

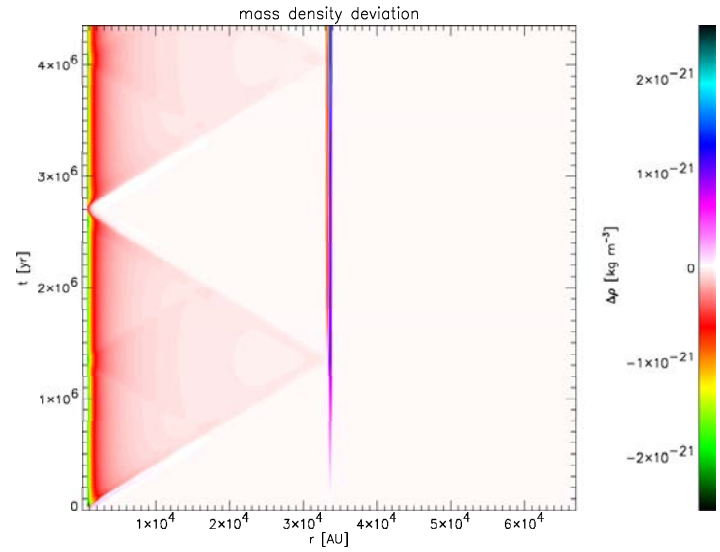

Figure 3.2: Mass density deviation $\Delta\rho$ from initial pressure equilibrium configuration (without self-gravity) during simulation with $N = 250$ and $\alpha = 0$.

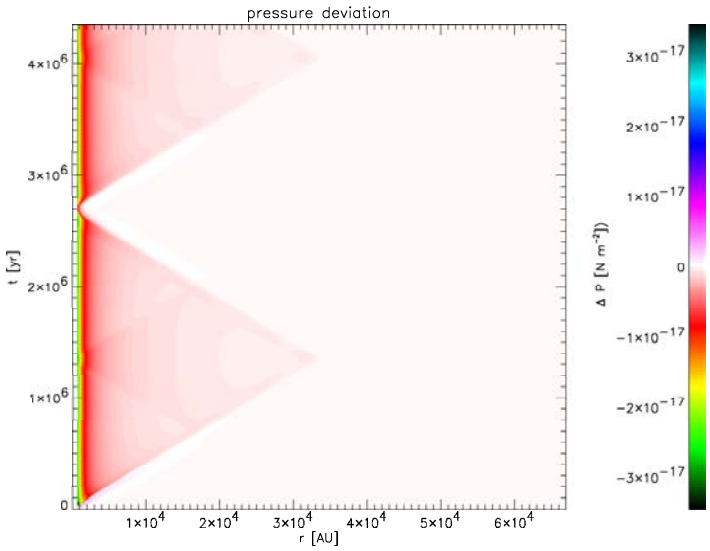

Figure 3.3: Pressure deviation ΔP from initial pressure equilibrium configuration (without self-gravity) during simulation with $N = 250$ and $\alpha = 0$.

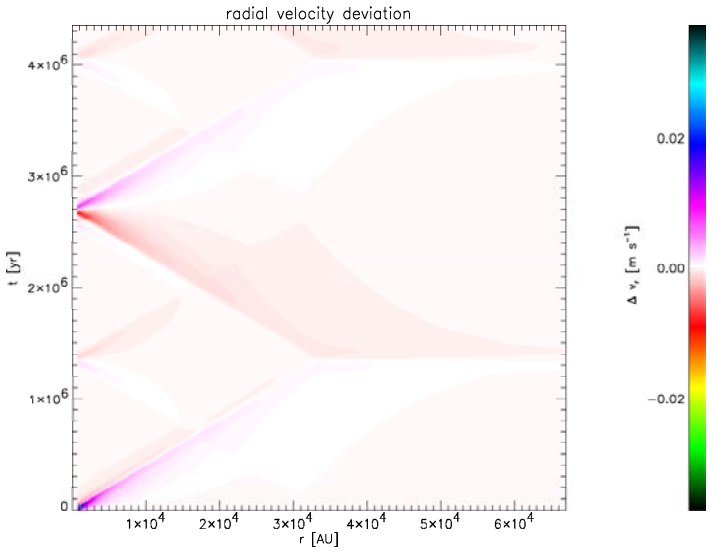

Figure 3.4: Velocity deviation Δv_r from initial pressure equilibrium configuration (without self-gravity) during simulation with $N = 250$ and $\alpha = 0$.

around $r = R_{cl}$ is present.

These test runs show that a grid with $N = 100$ and $\alpha = 0$ performs well when keeping a top-hat mass density without self-gravity in pressure equilibrium. Increasing resolution (smaller cells) in the inner part of the grid, by increasing N or α, seems to introduce some artefacts in the numerical method. An unphysical flow is generated at $r = 0$ and travels outwards over the grid. Furthermore, the discontinuity at $r = R_{cl}$ triggers a numerical diffusion into the low mass density area. Possible sources of error are given at the end of Section 3.1.3. Considering these problems, the grid with $N = 100$ and $\alpha = \ln(10)/\ln(N)$ does not perform worse than the grid with $N = 250$ and $\alpha = 0$. An unexpected side-effect of these test runs is that the inner boundary condition got tested on reflection of waves running inwards. As expected, these waves were reflected and bounce back onto the grid.

3.1.2 Hydrostatic equilibrium

In this test problem the time evolution of a hydrostatic equilibrium is simulated (including gravity), which is basically a stationary solution with $v_r = 0$ everywhere. It is expected (see Section B.2) that the hydrostatic equilibrium will stay stationary over many free-fall times. However, due to limited numerical precision and limited precision of the numerical method used, the simulation will inevitably introduce changes in the configuration away from the initial setup. Preferably, these changes will be small and will lead to a new, hydrostatic equilibrium configuration.

The basic setup is a dense cloud core with central temperature 1 K and central pressure $4.83 \times 10^{-14}\ N\ m^{-2}$, so that the central mass density is $5.86 \times 10^{-18}\ kg\ m^{-3}$ (same as in Section 3.1.1). The core is in hydrostatic equilibrium, thus the pressure gradient outwards balances the gravitational pull inwards. Using the method in Section 2.4.7, the hydrostatic equilibrium is calculated for the whole grid. The grid runs from $0 - 1.45$ Jeans radii (the method in Section 2.4.7 wouldn't allow a larger radius), divided into 100 cells with $\alpha = 0$. On the inner boundary a reflective boundary condition is set, while on the outer bounday an in/outflow boundary condition is set. The simulation time is 2 free-fall times. A summary of the relevant simulation parameters:

$\Gamma = \frac{5}{3}$,	$\mu = 1$
$N = 100$,	$\alpha = 0$
$M_J = 1.56\ M_\odot$,	$R_J = 3.36 \times 10^4\ AU$
$t_{ff} = 8.70 \times 10^5\ yr$,	$t_{sim} = 1.74 \times 10^6\ yr$
$R_{min} = 0\ AU$,	$R_{max} = 4.82 \times 10^4\ AU$
$\rho_c = 5.86 \times 10^{-18}\ kg\ m^{-3}$,	$P_c = 4.83 \times 10^{-14}\ N\ m^{-2}$
$v_r = 0\ m\ s^{-1}$	

The calculation of the Jeans mass, Jeans radius and free-fall time is based on the central mass density ρ_c and central pressure P_c.

Figures 3.5-3.7 show the initial mass density, pressure and velocity profiles that result from the hydrostatic equilibrium calculation. Both the mass den-

sity and the pressure decrease with increasing radius and the velocity is zero everywhere, as expected.

Figures 3.8-3.10 show the deviations in mass density $\Delta\rho$, pressure ΔP and velocity $\Delta v = \Delta v_r$ from the initial hydrostatic equilibrium during simulation. The maps of $\Delta\rho$ and ΔP are similar, with the largest deviations halfway the simulation near the centre to $\sim 3\%$ of the initial values. The velocity has its largest deviation increasing towards the end of the simulation at the outer edge of the grid to $\sim 2\ m\ s^{-1}$. This increasing deviation in velocity at the outer boundary indicates a slightly non-stable configuration, for this represents a mass outflow off the grid. During the simulation, the total mass excess of the cloud $M = 0.89\ M_\odot$ stays practically constant.

A second test run was performed with the same simulation parameters, except that the number of cells was increased to $N = 250$. The results are almost similar to the results of the first test run, except that the largest deviations $\Delta\rho$ and ΔP are $\sim\ 1\%$ of the initial values. The velocity has its largest deviation at $\sim 1\ m\ s^{-1}$. The total mass excess of the cloud is $M = 0.87\ M_\odot$, slightly less than in the first test run, stays constant.

A third test run was performed with $N = 100$ and $\alpha = \ln(10)/\ln(N)$. The results for ρ, P and v_r are very similar to the results of the first and second test run. However, in this test run, the deviations $\Delta\rho$, ΔP and Δv_r are dominated by a large deviation at the innermost cell. This effect seems similar to the observed artefacts in the test runs of Section 3.1.1. The largest deviations $\Delta\rho$ and ΔP are now $\sim 30 - 50\%$ of the initial values. The largest deviation of Δv_r is also found at the inner boundary at $\sim 60\ m\ s^{-1}$. The total mass excess of the cloud is $M = 0.90\ M_\odot$, slightly more than in the first and second test run, stays constant.

These test runs show that a grid with $N = 100$ and $\alpha = 0$ performs well when keeping a hydrstatic equilibrium configuration in equilibrium. The deviations are small compared to the actual state values and the small mass outflow does not seem to influence the configuration. Increase in the number of cells to $N = 250$ results in an even better performance of the model. Additional testing shows that this improves even more with $N = 500$. Using the grid with $\alpha = \ln(10)/\ln(250)$ and $N = 100$ introduces an unphysical artefact at the innermost part of the grid. This seems similar to the observed artefacts in the test runs of Section 3.1.1, although they are not present for the $\alpha = 0$ test runs. Possible sources of error are given at the end of Section 3.1.3.

3.1.3 Supersonic stationary flow

In this test problem the time evolution of a stationary flow is simulated, including gravity. Because of its nature (see Section B.2), it is expected that the stationary flow will stay the same over many free-fall times. However, due to limited numerical precision and limited precision of the numerical method used, the simulation will inevitably introduce changes in the configuration away from the initial setup. Preferably, these changes will be small and will lead to a new, stationary configuration.

The basic setup is a dense cloud core with central temperature $1\ K$ and central pressure $4.83 \times 10^{-14}\ N\ m^{-2}$, so that the central mass density is $5.86 \times 10^{-18}\ kg\ m^{-3}$. A wind is blowing radially outwards from this core at a central supersonic velocity of Mach $\mathcal{M} = 2.0$. Using the method in Section 2.4.7, the

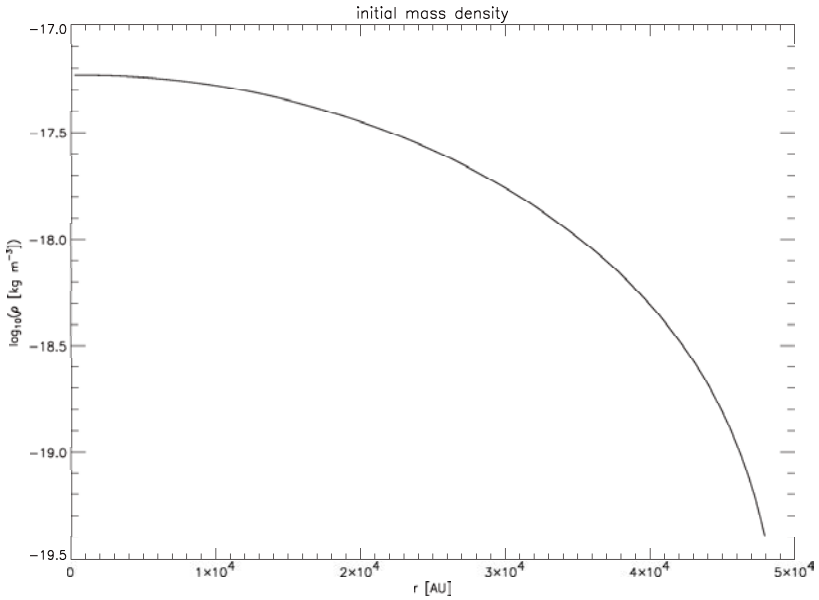

Figure 3.5: Calculated mass density ρ of hydrostatic equilibrium at the beginning of the simulation.

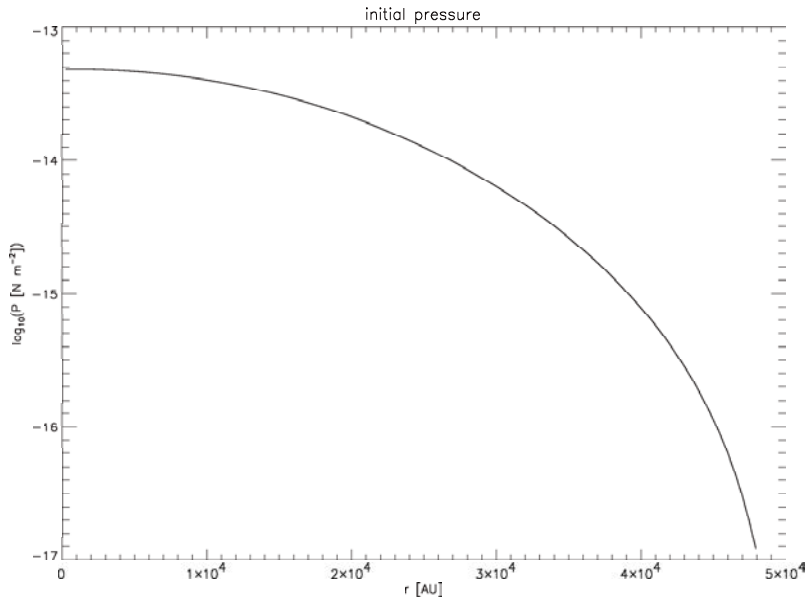

Figure 3.6: Calculated pressure P of hydrostatic equilibrium at the beginning of the simulation.

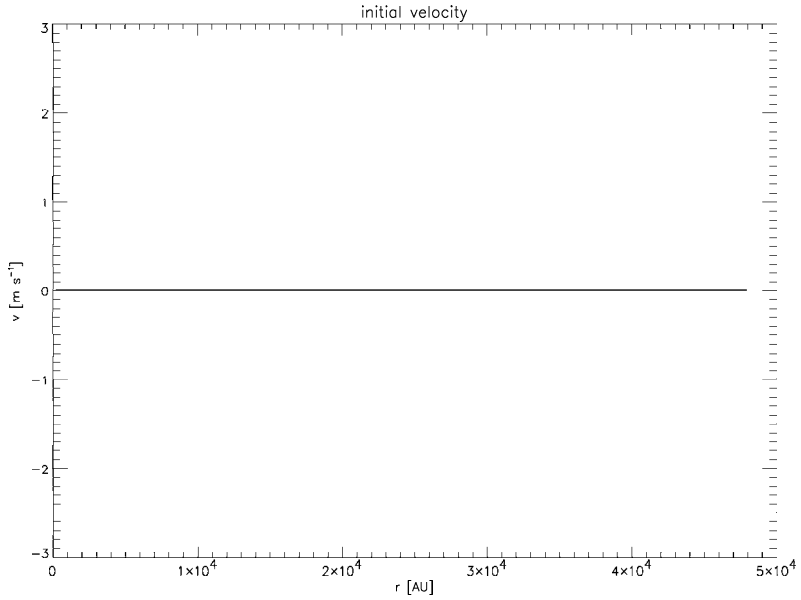

Figure 3.7: Calculated velocity v_r of hydrostatic equilibrium at the beginning of the simulation.

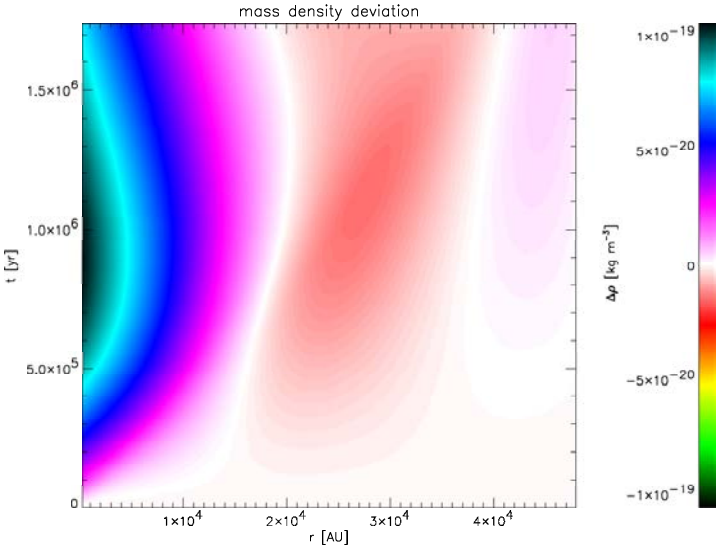

Figure 3.8: Mass density deviation $\Delta\rho$ from initial hydrostatic equilibrium configuration during simulation with $\alpha = 0$.

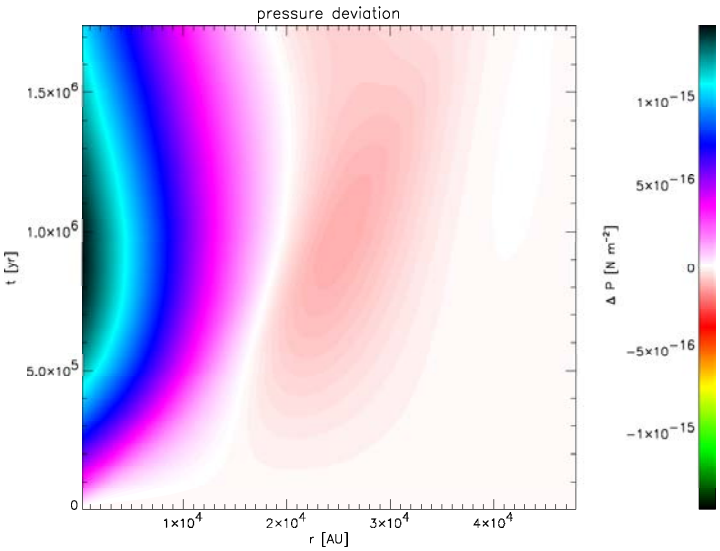

Figure 3.9: Pressure deviation ΔP from initial hydrostatic equilibrium configuration during simulation with $\alpha = 0$.

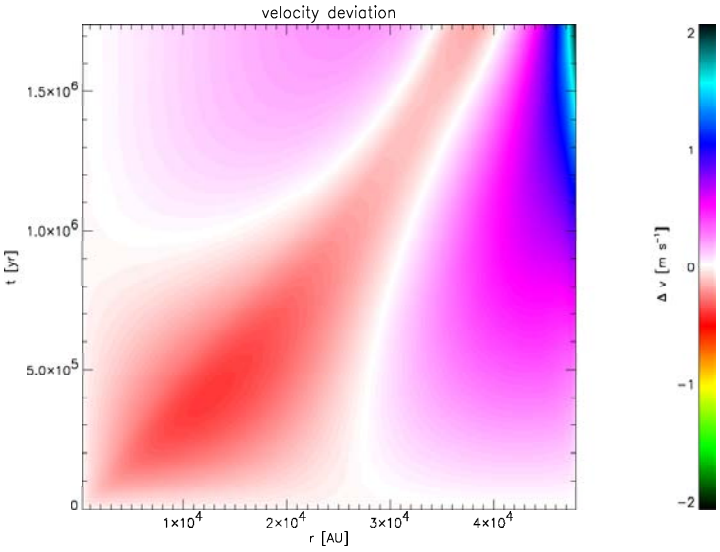

Figure 3.10: Velocity deviation Δv_r from initial hydrostatic equilibrium configuration during simulation with $\alpha = 0$.

stationary flow is calculated for the whole grid. This method did not give solutions for $r_{min} = 0$, so the 2 innermost cells of the grid were skipped. The grid consists of 100 cells (+2) with $\alpha = 0$. On both the inner and outer boundary, an in/outflow boundary condition was set. The simulation time is 10 free-fall times (based on the central gas state). A summary of the relevant simulation parameters:

$$\Gamma = \frac{5}{3}, \qquad \mu = 1$$
$$N = 100(+2), \qquad \alpha = 0$$
$$M_J = 1.56\ M_\odot, \qquad R_J = 3.36 \times 10^4\ AU$$
$$t_{ff} = 8.70 \times 10^5\ yr, \qquad t_{sim} = 4.35 \times 10^7\ yr$$
$$R_{min} = 1.66 \times 10^4\ AU, \qquad R_{max} = 8.47 \times 10^5\ AU$$
$$\rho_c = 5.86 \times 10^{-18}\ kg\ m^{-3}, \qquad P_c = 4.83 \times 10^{-14}\ N\ m^{-2}$$
$$c_s = 1.17 \times 10^2\ m\ s^{-1}, \qquad v_{r,c} = 2.34 \times 10^2\ m\ s^{-1}$$

Figures 3.11-3.13 show the mass density, pressure and velocity profiles that result from determining the stationary flow. Both the mass density and the pressure peak in the centre and drop at increasing radius. The velocity however, peaks just off centre.

Figures 3.14-3.16 are maps of the mass density ρ, pressure P and velocity v_r as functions of space and time. From these figures, it can be seen that some sort of wave is running from the inner boundary outwards over the outer boundary. This is probably an adjustment within the first few cells just after the start of the simulation, which propagates outwards. It looks like ρ and v_r do not change when the wave passes through, but P is slightly decreased. The simulation is continued for some time after the wave runs off the grid, but no more changes are visible. The second test run, with $N = 250$ (+2), gives similar results. The third test run with $N = 100$ and $\alpha = \ln(10)/\ln(250)$ also shows a propagating wave from the centre, but now P is slightly increased afterwards.

The three test runs show that none of the grids is able to keep the supersonic stationary flow in its initial form. All grids suffer from a deviation at the innermost part of the grid, which propagates as a wave outwards. This wave changes the gas state over the whole grid. This new state appears to be a true stationary solution for the grid used, as it doesn't seem to be changing anymore. Converging to a new stationary state instead of diverging can be seen as an indication of stability of the model. An unexpected side-effect of these test runs is that the outer boundary condition gets tested on non-reflection of waves running outwards. As expected, these waves run off the grid without reflection.

3.1.4 Summary

When considering the pressure equilibrium results, increasing the number of cells on the inner grid (by increasing N or α) did not improve the accuracy. On the contrary, a relatively large deviation in the gas state was detected at the innermost cells of the grid. This deviation induced waves upon the grid, thereby also influencing the gas state on other parts of the grid. When considering the hydrostatic equilibrium results, increasing N made the deviations smaller, thus improving the accuracy. The accuracy decreased when α was increased, because

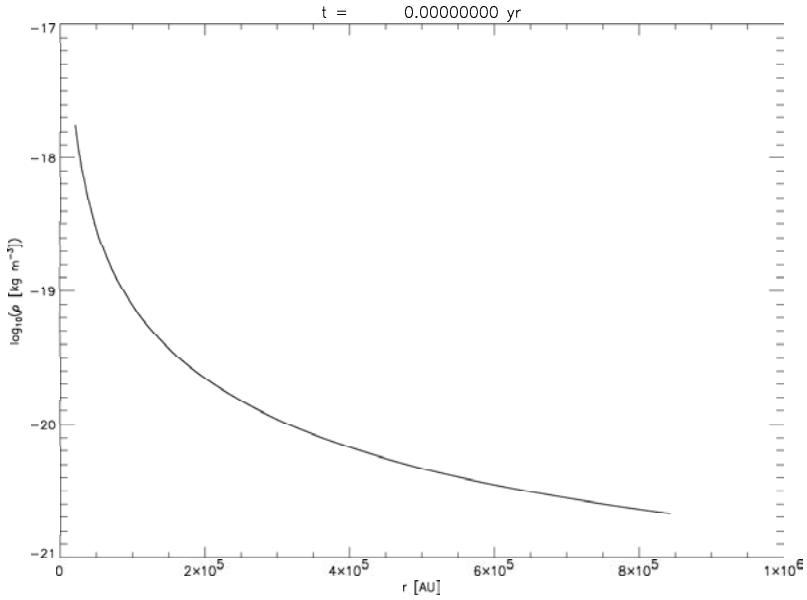

Figure 3.11: Calculated mass density ρ of supersonic stationary flow at the beginning of the simulation.

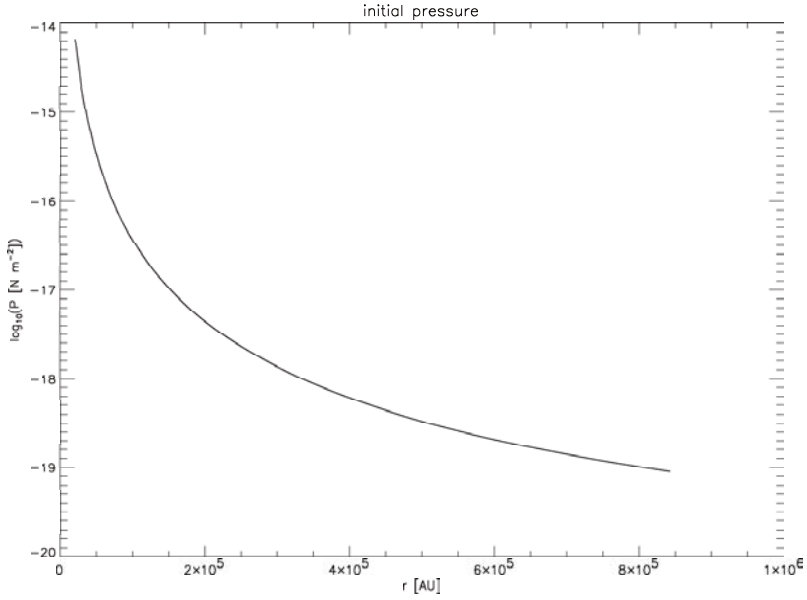

Figure 3.12: Calculated pressure P of supersonic stationary flow at the beginning of the simulation.

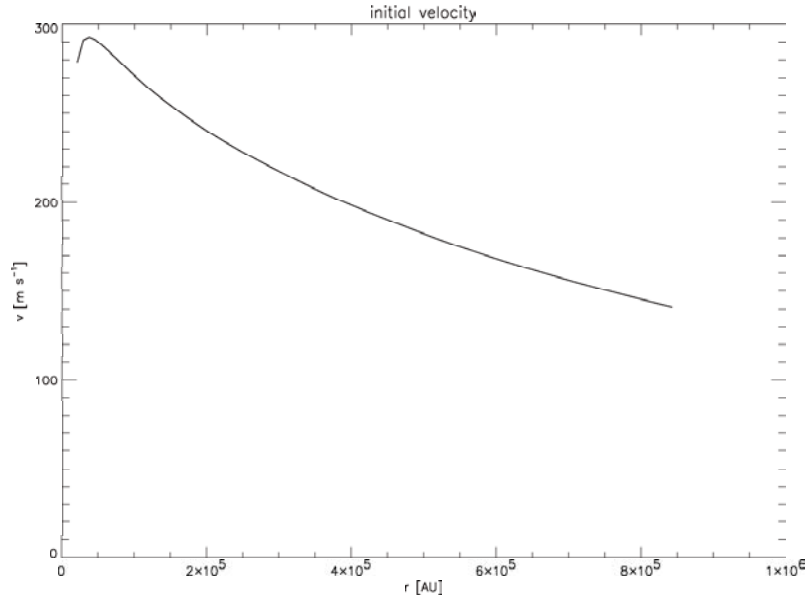

Figure 3.13: Calculated velocity v_r of supersonic stationary flow at the beginning of the simulation.

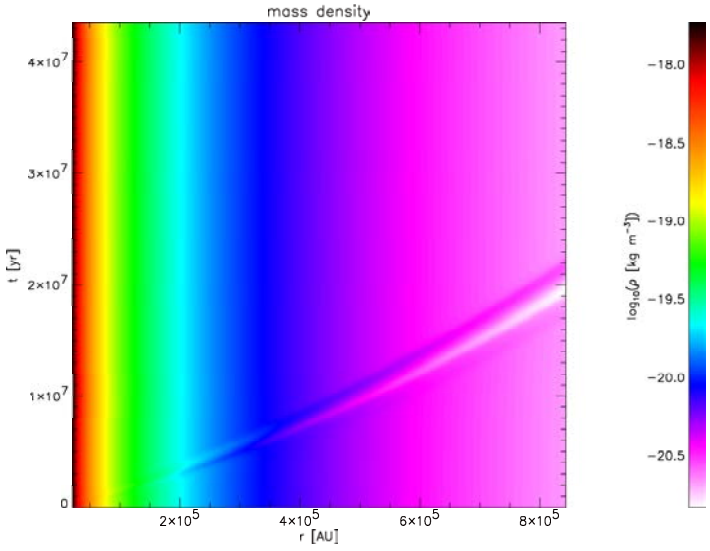

Figure 3.14: Mass density ρ during simulation with $N = 100$ and $\alpha = 0$.

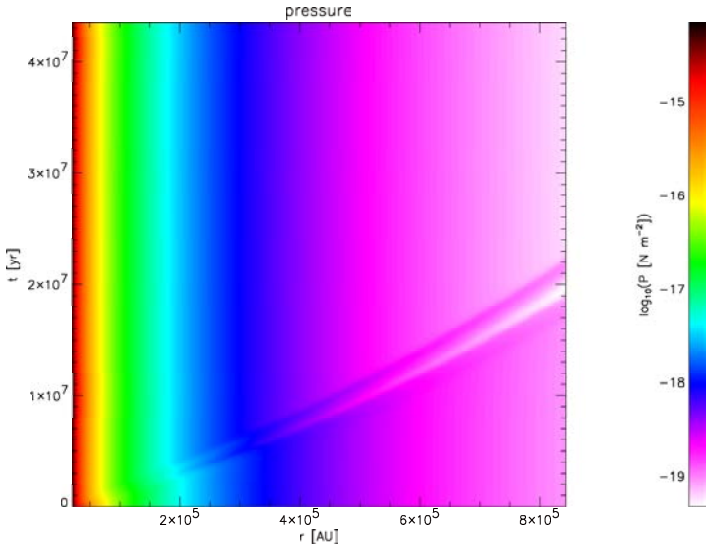

Figure 3.15: Pressure P during simulation with $N = 100$ and $\alpha = 0$.

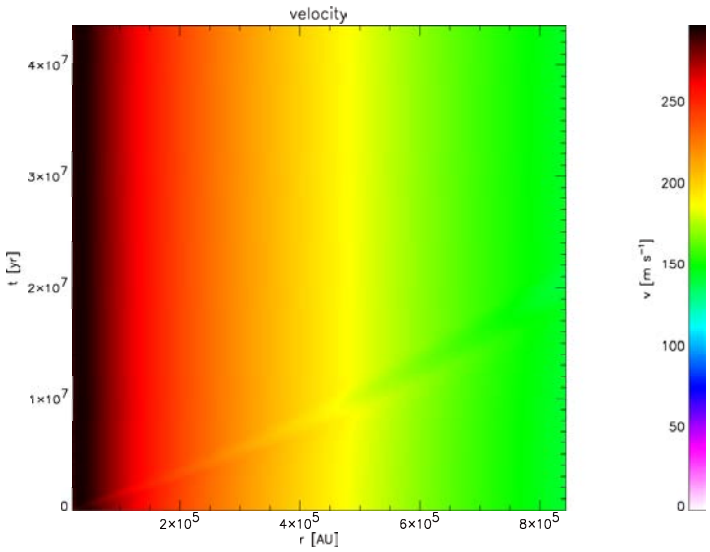

Figure 3.16: Velocity v_r during simulation with $N = 100$ and $\alpha = 0$.

of a large deviation at the inner cells. When considering the stationary flow results, it is seen that all grids re-adjust the initial gas state from the inside out, to gain a new stationary state.

The thing that is common in the results of all three test problems is the unpredictable performance of the innermost part of the grid. A possible cause of the effects seen, is the fact that near the origin, the radial coordinate ℓ becomes comparable to the cell size $\Delta\ell$. At these radii, the volume term ${r_i}^2 {r_i}' \Delta\ell$ (that shows up in numerical integration of the Euler equations and the gravitational force) is a poor (too large) approximation for the true volume term $\frac{1}{3}\left({r_{i+\frac{1}{2}}}^3 - {r_{i-\frac{1}{2}}}^3\right)$. Another possible cause is the fact that in some test runs the gradients of ρ, P and v_r are largest near the centre. As a result, these gas state parameters tend to vary the most within the boundaries of the innermost cells. When these cells are too wide, the average state of these cells might not be representative for the whole cell (see Section 2.4.1). Both explanations are plausible, when addressing the fact that in both test runs the deviations from the stationary solution are largest near the centre. And there is also a possibility that the computer model contains bugs, which generates behaviour of the grid that differs from the intended model behaviour.

Although it is hard to draw any hard conclusions, it is advisable, on the basis of the results above, not to use a high cell count N or use an $\alpha \neq 0$ unless it is absolutely necessary.

3.2 Simulation results

In this section, the results of two simulations with different initial conditions are presented. The first simulation comprises the gravitational collapse of an isothermal top-hat mass distribution, while the second simulation comprises the gravitational collapse of a mass distribution just off hydrostatic equilibrium. Both simulations were performed by other authors as well, so it is easier to verify the results.

3.2.1 Larson's isothermal collapsing sphere

Larson [8] was one of the first to use numerical hydrodynamical models to simulate collapsing proto-stars. His model consists of a spherically symmetric, top-hat mass density distribution, with no rotation, magnetic fields and turbulent motions. His model does include simple radiative and convective energy transfer. During the first stages of the gravitational collapse of his model, Larson assumes that the cloud is optically transparent, so that all radiation is transmitted away without heating the gas. He therefore assumes an isothermal collapse.

Larson starts out with a 1 $M_\odot$ cloud with temperature $T = 10\ K$, mass density $\rho = 1.10 \times 10^{-16}\ kg\ m^{-3}$ and relative particle mass $\mu = 2.46$ (which includes dust). In this section, the isothermal part of Larson's collapse is re-simulated up to $4.44 \times 10^5\ yr$, the time at which Larson's model formed a dense core. The isothermal behaviour is imitated by choosing Γ close to one. Larson's model does not include a low mass density environment, but that seems a bit artificial. Here, the environment is set to $\rho = 1.10 \times 10^{-19}\ kg\ m^{-3}$. A summary

of the relevant simulation parameters:

$\Gamma = 1.001,$	$\mu = 2.46$
$N = 100,$	$\alpha = 0$
$M_J = 5.14\ M_\odot,$	$R_J = 4.05 \times 10^5\ AU$
$t_{ff} = 2.01 \times 10^5\ yr,$	$t_{sim} = 4.44 \times 10^5\ yr$
$R_{min} = 0.0\ AU,$	$R_{max} = 1.21 \times 10^4\ AU$
$R_{cl} = 1.09 \times 10^4\ AU,$	$M_{cl} = 1.00\ M_\odot$
$\rho_{cl} = 1.10 \times 10^{-16}\ kg\ m^{-3},$	$\rho_{env} = 1.10 \times 10^{-19}\ kg\ m^{-3}$
$P_{cl} = P_{env} = 3.72 \times 10^{-12}\ N\ m^{-2},$	$v_{r,cl} = v_{r,env} = 0\ m\ s^{-1}$

The resulting simulated mass density distribution is shown in Figure 3.17. It is observed that the dense core forms in half the time of Larson's model, namely $\sim 2.2 \times 10^5\ yr$. This is in good agreement with the calculated free-fall time. Larson claims that the free-fall time of his model is strongly affected by the absence of the low mass density environment.

To make a better comparison with Larson's results, the simulation was repeated with a higher resolution ($N = 500$) and shorter simulation time $t_{sim} = 1.2\ t_{ff} = 2.41 \times 10^5\ yrs$. The results are presented in Figures 3.18-3.23. During the collapse, the mass density and the pressure show an enormous increase by a factor $10^4 - 10^6$, strongly peaked at the centre of the cloud. It is at this time that the model becomes increasingly unphysical, because the extreme situation in the centre will lead to an increase of all sorts of gas interactions, like chemical reactions and (de-)excitation and (de-)ionisation of gas particles. The opacity of the central core will increase, trapping radiation within, causing the temperature of the core to rise. This behaviour is not incorporated in the model.

The simulation results can be expected to be valid until first core formation. The core formation time is defined as the time at which the central velocity over sound speed ratio reaches its first (negative) peak. At that time ($\sim 2.19 \times 10^5\ yr = 1.09\ t_{ff}$), already $\sim 90\%$ of the mass is within 50% of the cloud's initial radius. The outer boundary of the cloud only moves slowly towards the centre. Within the boundary of the cloud, the temperature stays constant at $\sim 10\ K$, as can be expected of an isothermal cloud.

Figure 3.24 shows a reproduction of Figure 1 from Larson [8] (see Figure 1.1). This shows an $\rho \sim r^{-2}$ dependence for the mass density on the outer boundary of the collapsing cloud. Apart from a different time scale, there is a good match between both figures, although Larson is able to simulate closer to $r = 0$. The presence or absence of an environment appears not to influence the observed $\rho \sim r^{-2}$ dependence.

As can be seen in Figure 3.24, the mass density plots only run until $r \sim 10^{14.75}\ cm$ on the inside of the grid, which equals the centre of the innermost grid cell. To get closer to zero, the number of grid cells near $r = 0$ needs to be increased even more. This can be done by increasing the number of grid cells N or by increasing α. Multiple simulations were performed with larger N and/or $\alpha \neq 0$. However, all of these simulations ended prematurely, because of negative pressure at the centre grid cell.

Problems with negative pressure arise when the mass density in the centre

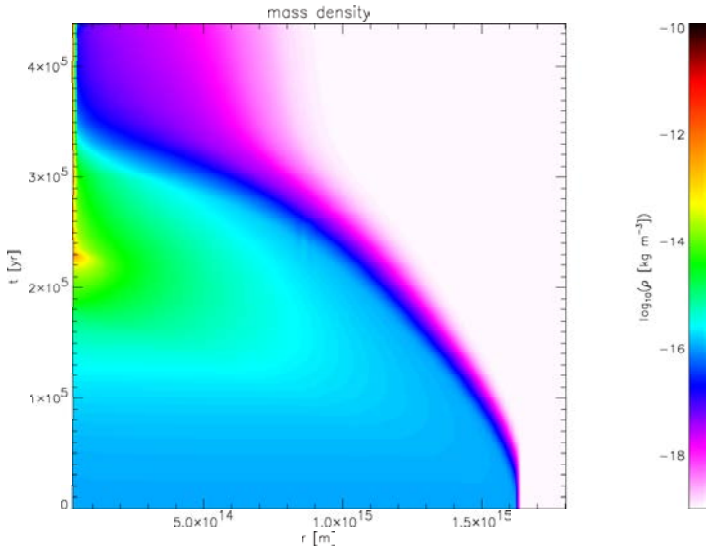

Figure 3.17: Simulated mass density ρ during an isothermal top-hat collapse with $N = 100$ and $\alpha = 0$.

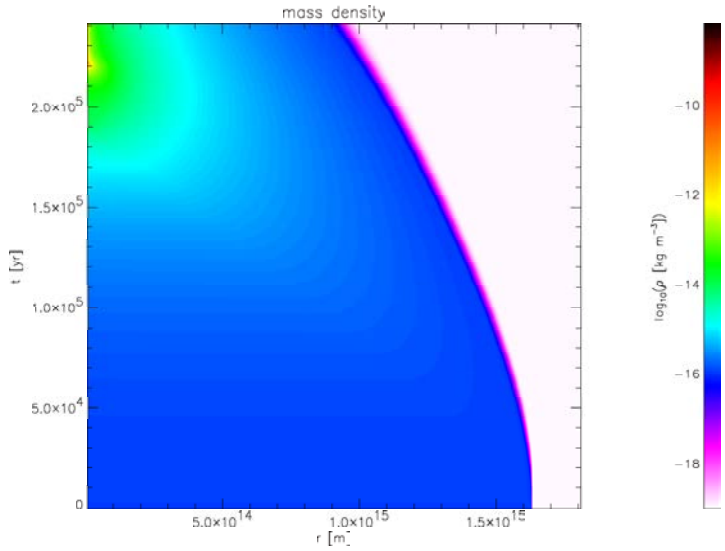

Figure 3.18: Simulated mass density ρ during an isothermal top-hat collapse with $N = 500$ and $\alpha = 0$.

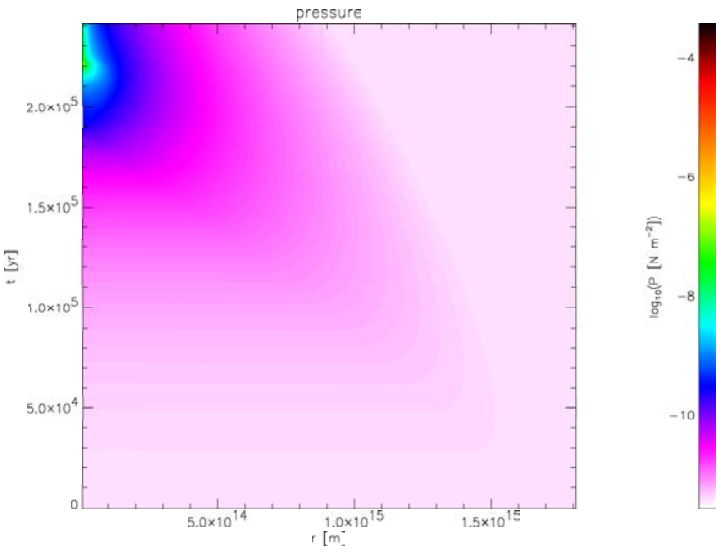

Figure 3.19: Simulated pressure P during an isothermal top-hat collapse with $N = 500$ and $\alpha = 0$.

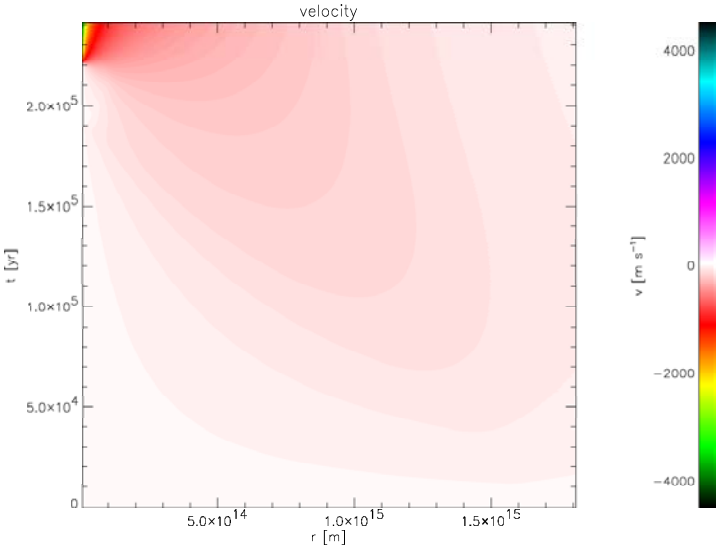

Figure 3.20: Simulated velocity v_r during an isothermal top-hat collapse with $N = 500$ and $\alpha = 0$.

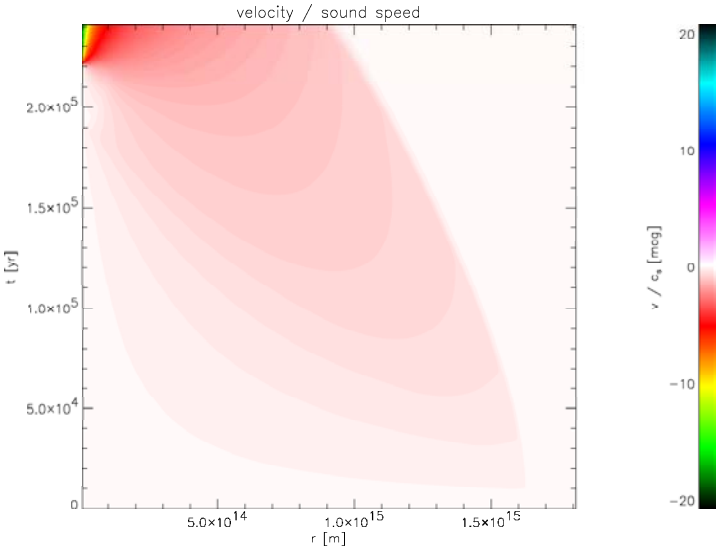

Figure 3.21: Simulated (radially signed) Mach number $\mathcal{M} = v_r/c_s$ during an isothermal top-hat collapse with $N = 500$ and $\alpha = 0$.

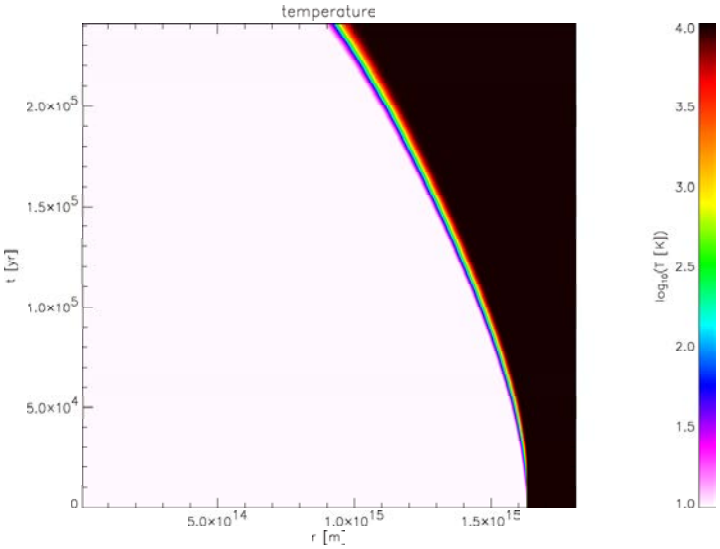

Figure 3.22: Simulated temperature T during an isothermal top-hat collapse with $N = 500$ and $\alpha = 0$.

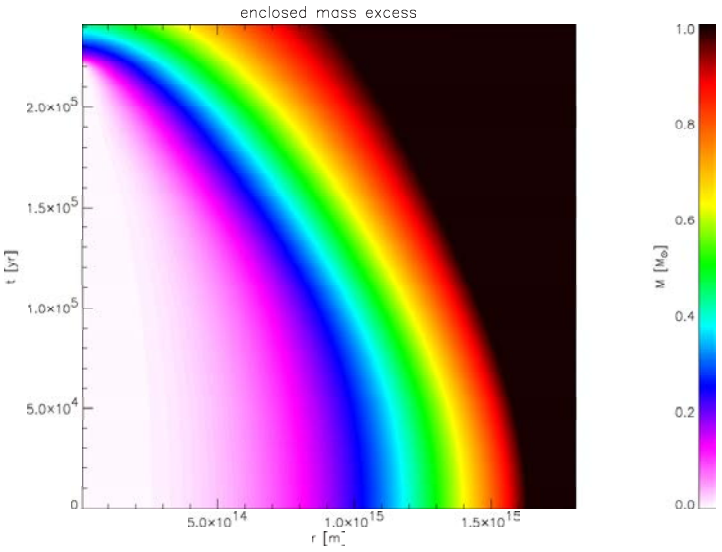

Figure 3.23: Simulated enclosed mass excess $M(r)$ during an isothermal top-hat collapse with $N = 500$ and $\alpha = 0$.

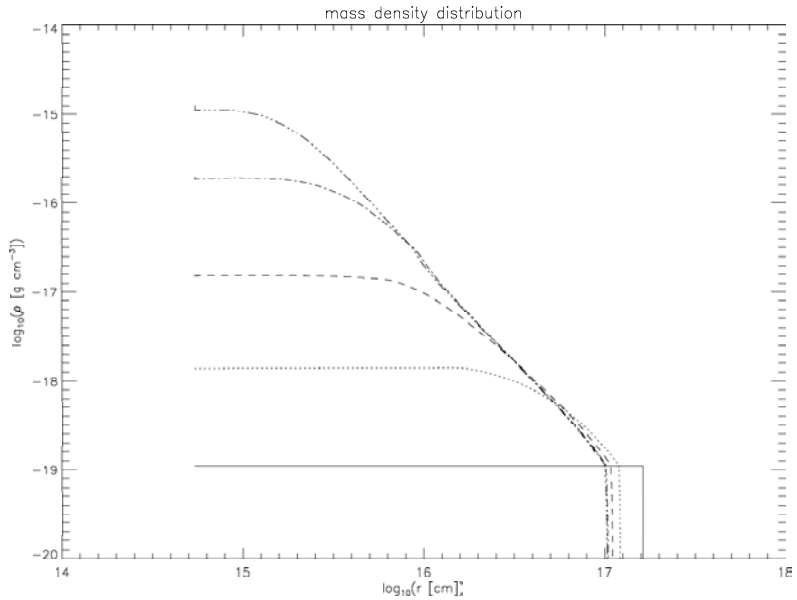

Figure 3.24: Reproduction of the mass density dependence $\rho \sim r^{-2}$ found by Larson (the units are comparable to Larson [8], Figure 1). From bottom to top, the simulation times are 0.00, 1.72, 2.00, 2.15 and 2.18×10^5 yr.

cell gets too high. In this case, having a larger centre cell helps to smear out a high mass density gradient over a larger volume, which results in a lower average mass density. In this case, a decrease in resolution near $r = 0$ actually helps to make the simulations more stable.

3.2.2 Foster & Chevalier's marginally stable sphere

Foster&Chevalier [6] performed similar simulations as Larson (see Section 3.2.1), but their initial mass density distribution is that of a dense cloud, close to hydrostatic equilibrium, embedded in a low mass density environment. They introduce dimensionless parameters to make the whole problem scalable:

$$D = \frac{\rho}{\rho_c}, \qquad \tau = \sqrt{4\pi G\rho_c}\, t$$
$$u = \frac{v_r}{c_s}, \qquad \xi = \sqrt{4\pi G\rho_c}\, \frac{r}{c_s} \tag{3.1}$$

Foster&Chevalier do not take the beginning of the simulation, but the core formation time as $\tau = 0$.

By solving the hydrostatic equilibrium problem with these parameters, Foster&Chevalier reduce the number of free parameters of the model to one: the outer boundary ξ_{cl} of the cloud. The environment is in pressure balance with the cloud boundary, but has a mass density which is a factor 10^{-6} less. They make the collapse of a marginally stable sphere their standard test case, which has $\xi_{cl} = 6.451$. To make the cloud collapse, the gas state is perturbed by enhancement of the mass density and pressure of the whole setup by 10%. Foster&Chevalier [6] found that it takes $\Delta\tau = 11.2$ from the start of the simulation for the outer part of the cloud to collapse to the centre.

In this section, the isothermal collapse of the marginally stable cloud is re-simulated. To give the simulation some physical relevance, the central properties of the cloud are taken from Larsons's top-hat cloud in Section 3.2.1. With central mass density $\rho_c = 1.10 \times 10^{-16}\ kg\ m^{-3}$ and central pressure $P_c = 3.72 \times 10^{-12}\ N\ m^{-2}$, it follows from (3.1) that $\tau = 1$ corresponds to $t = 1.04 \times 10^5\ yr$ $(= 0.520\ t_{ff})$ and $\xi = 1$ to $r = 4.03 \times 10^3\ AU$ $(= 1.00 \times 10^{-2}\ R_J)$. From these, a hydrostatic equilibrium is calculated with the method in Section 2.4.7, up to a cloud radius of $R_{cl} = 2.61 \times 10^4\ AU$ (which equals $\xi_{cl} = 6.451$). The environment pressure and mass density are constant and are derived from the gas state at the cloud boundary. After the 10% enhancement, this results in a cloud of 2.68 $M_\odot$. The simulation time is set to $\Delta\tau = 14.0$ which corresponds to $1.46 \times 10^6\ yr$. A summary of the relevant simulation parameters:

$\Gamma = 1.001$, $\mu = 2.46$
$N = 100$, $\alpha = 0$
$M_J = 5.14 \times 10^4\ M_\odot$, $R_J = 4.05 \times 10^4\ AU$
$t_{ff} = 2.01 \times 10^5\ yr$, $t_{sim} = 1.46 \times 10^6\ yr$
$R_{min} = 0\ AU$, $R_{max} = 2.90 \times 10^4\ AU$
$\rho_c = 1.10 \times 10^{-16}\ kg\ m^{-3}$, $P_c = 3.72 \times 10^{-12}\ N\ m^{-2}$
$v_{r,cl} = v_{r,env} = 0\ m\ s^{-1}$

The calculation of the Jeans mass, Jeans radius and free-fall time is based on the central mass density ρ_c and central pressure P_c.

The resulting simulated mass density distribution is shown in Figure 3.25. It is observed that the dense core forms in $\sim 7.3 \times 10^5\ yr$, that is $\sim 3.6\ t_{ff}$ or $\Delta\tau = 7.00$. Note that the value of t_{ff} is based on central values of ρ and P, not on their average values, so this might explain why the core formation takes more than $1\ t_{ff}$.

The simulation was repeated with a higher resolution ($N = 500$) and shorter simulation time $t_{sim} = 4.3\ t_{ff} = 8.63 \times 10^5\ yrs$, corresponding to $\Delta\tau = 8.27$. The results are presented in Figures 3.26-3.31 When considering the general behaviour of the cloud, the collapse looks very similar to Larson's collapsing top-hat cloud. The mass density and the pressure show a central increase by a factor $10^4 - 10^6$, while the temperature stays constant within the cloud's boundary. At core formation time, ($t = 7.28 \times 10^5\ yr$), $\sim 70\%$ of the mass is within 50% of the cloud's initial radius. Compared to Larson's collapsing top-hat cloud, the mass flow inwards is slower. This might well be explained by the fact that Larson's collapsing top-hat cloud is initially much farther from hydrostatic equilibrium than Foster&Chevalier's enhanced marginally stable sphere.

Figures 3.32-3.33 are reproductions of Figures 1(a) and 1(b) from Foster& Chevalier [6] (see Figure 1.2), expressed in the dimensionless units of (3.1). Figure 3.32 shows an $\xi \sim \rho \sim r^{-2}$ dependence for the mass density on the outer boundary of the collapsing cloud, similar to Larson's top-hat collapse. Apart from a different time scale, there is a good match between both figures, except for the result at $\tau = 0.00$. The mass density deviates upwards, where it should still follow the $\rho \sim r^{-2}$ law. Figure 3.33 shows the time development of the velocity to sound speed ratio u. Again, apart from a different time scale, the figure matches the results of Foster&Chevalier, except for the result at $\tau = 0.00$. Where u should gradually converge to Mach -3.3 inwards along a smooth curve connecting the plots on the outside, it shows an enormous deviation to much lower values of u.

As can be seen in Figures 3.32-3.33, both plots only run until $\xi \sim 10^{-2.12}$ on the inside of the grid, which equals the centre of the innermost grid cell. This is far less than Foster&Chevalier, who reach $\xi \sim 10^{-8}$. Multiple simulations were performed with larger N and $\alpha \neq 0$. However, all of these simulations ended premature, because of negative pressure at the centre grid cell.

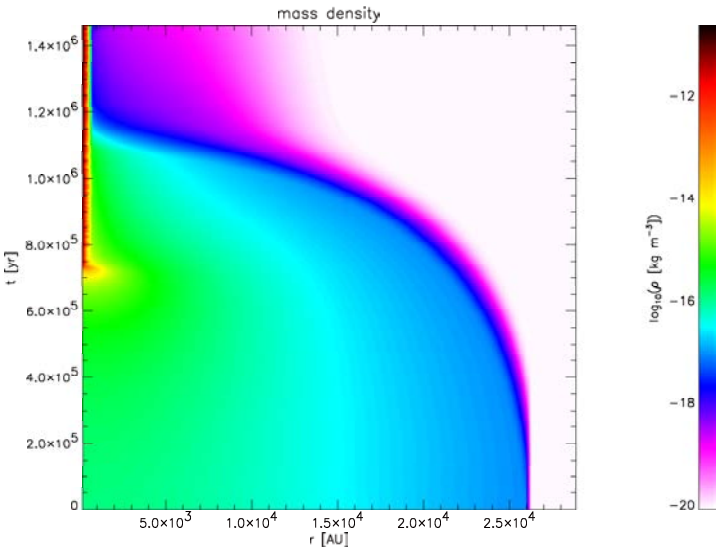

Figure 3.25: Simulated mass density ρ during the isothermal collapse of an enhanced hydrostatic cloud with $N = 100$ and $\alpha = 0$.

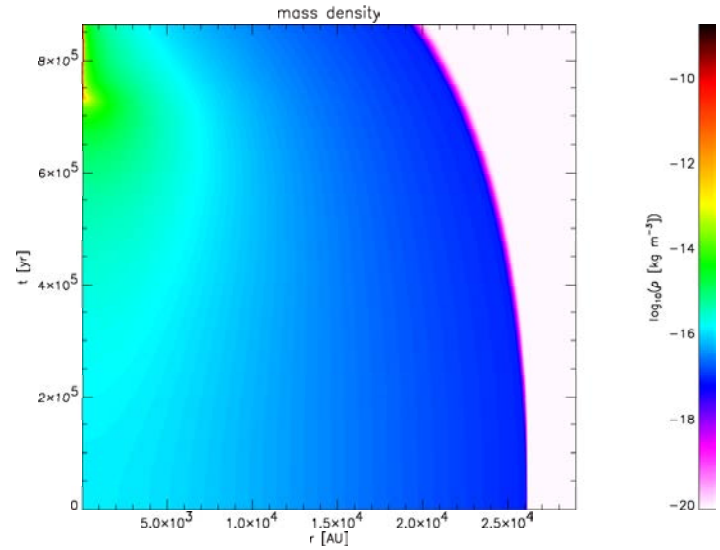

Figure 3.26: Simulated mass density ρ during the isothermal collapse of an enhanced hydrostatic cloud with $N = 500$ and $\alpha = 0$.

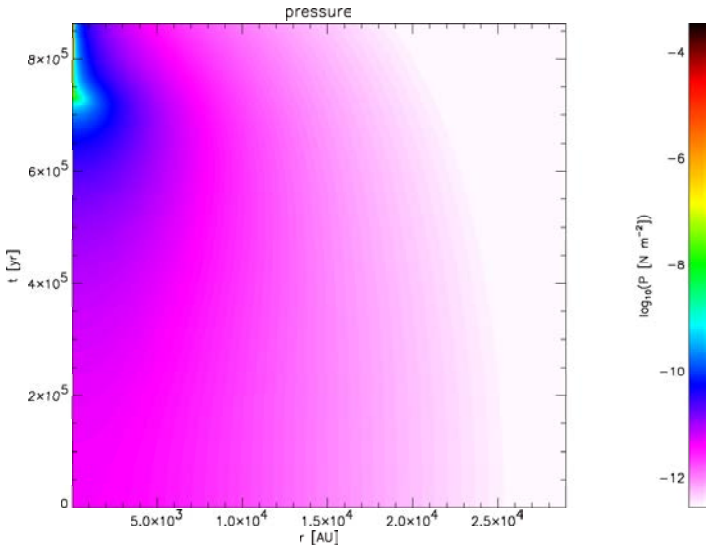

Figure 3.27: Simulated pressure P during the isothermal collapse of an enhanced hydrostatic cloud with $N = 500$ and $\alpha = 0$.

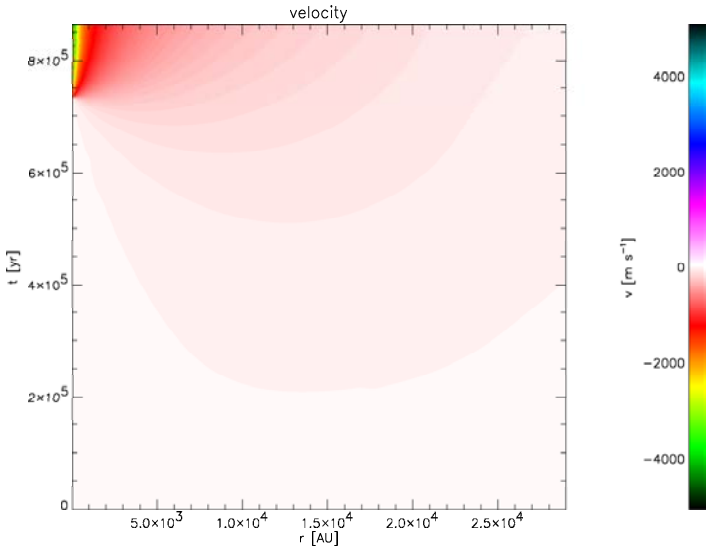

Figure 3.28: Simulated velocity v_r during the isothermal collapse of an enhanced hydrostatic cloud with $N = 500$ and $\alpha = 0$.

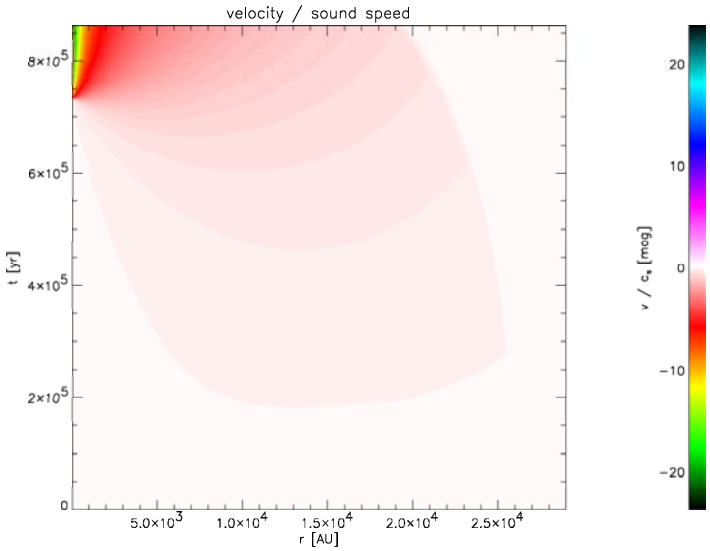

Figure 3.29: Simulated (radially signed) Mach number $\mathcal{M} = v_r/c_s$ during the isothermal collapse of an enhanced hydrostatic cloud with $N = 500$ and $\alpha = 0$.

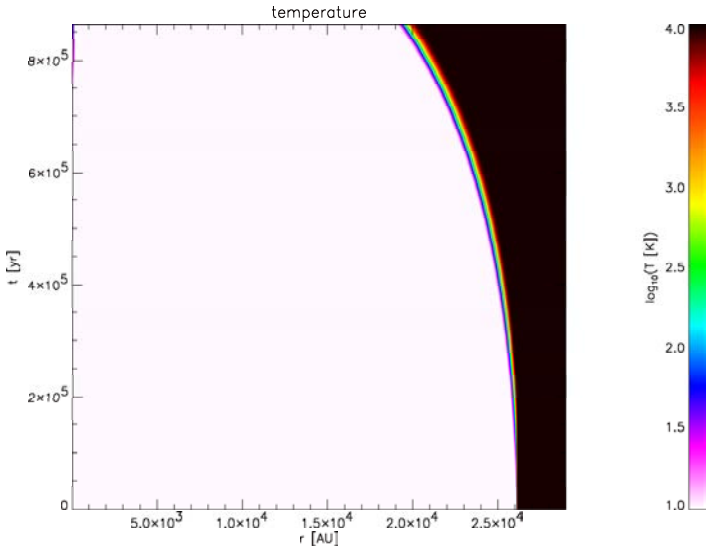

Figure 3.30: Simulated temperature T during the isothermal collapse of an enhanced hydrostatic cloud with $N = 500$ and $\alpha = 0$.

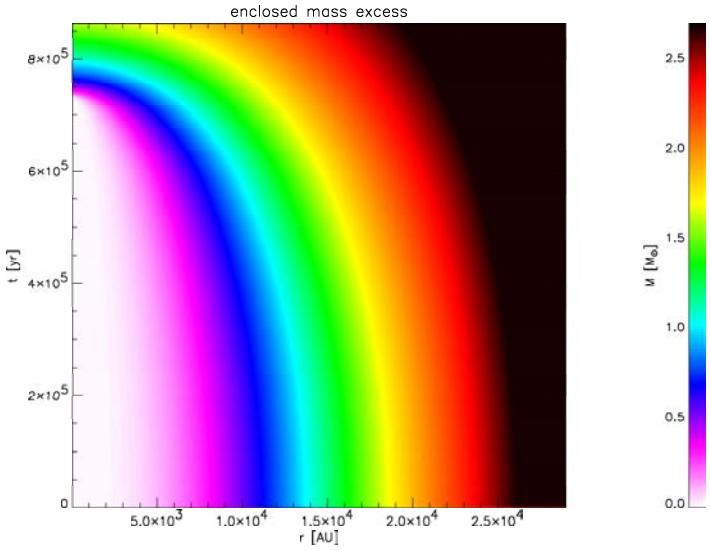

Figure 3.31: Simulated enclosed mass excess $M(r)$ during the isothermal collapse of an enhanced hydrostatic cloud with $N = 500$ and $\alpha = 0$.

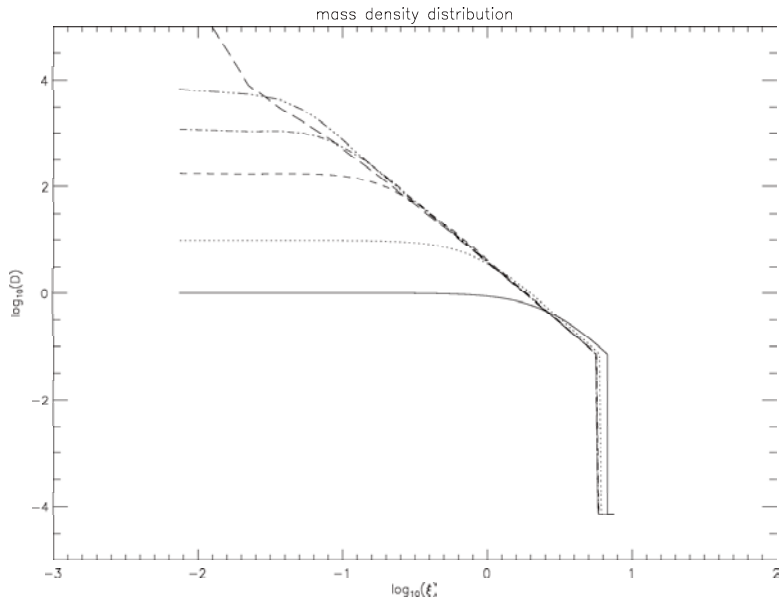

Figure 3.32: Reproduction of the mass density dependence $\rho \sim r^{-2}$ found by Foster&Chevalier, expressed in their dimensionless units (see (3.1)). From bottom to top, the simulation times are $\tau = -7.40$, -0.972, -0.173, -0.0694, -0.0346 and 0.00.

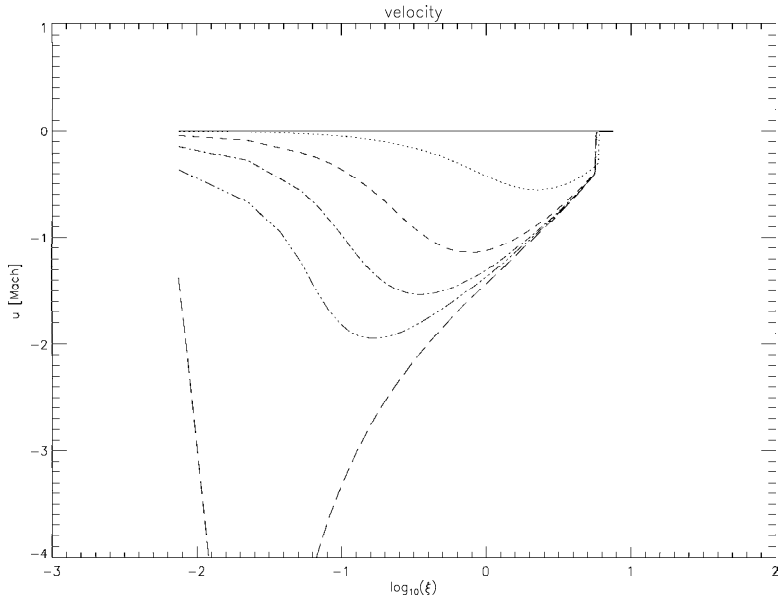

Figure 3.33: Reproduction of the (radially signed) Mach numbers found by Foster&Chevalier, expressed in their dimensionless units (see (3.1)). From top to bottom, the simulation times are $\tau = -7.40$, -0.972, -0.173, -0.0694, -0.0346 and 0.00.

Chapter 4

Discussion

4.1 Summary

Using the general relativistic approach of Eulderink&Mellema [4], the non-relativistic Euler equations for spherical coordinates were derived, including gravity, where the radial distance r was replaced by a general radial coordinate ℓ. This way, it was possible to create a simulation model where the cell width Δr of the spatial grid is variable. This can be applied to increase the number of cells in areas where a higher spatial resolution is required.

These new Euler equations were incorporated in the Roe solver, a numerical method to integrate the Euler equations to second order accuracy. For this method, the eigenvalues and eigenvectors of the Jacobian were determined, as well as the projection coefficients.

The application for the model was the 1-dimensional study of the gravitational collapse of a spherically symmetric, non-rotating cloud of gas. Because the Roe solver uses a fixed grid (fixed in space), extra spatial resolution is required near the origin, where the collapsing mass is expected to generate high gradients for all gas parameters.

Several simulations were performed to test the functionality and accuracy of the model. These included a pressure equilibrium (without gravity), a hydrostatic equilibrium and a supersonic stationary flow.

The evolution of two standard configurations, a top-hat (Larson [8]) and an enhanced hydrostatic equilibrium (Foster&Chevalier [6]), were simulated and compared to literature results.

4.2 Conclusions

The main application of this new Roe solver was the study of gravitationally collapsing clouds of gas in space. For this, a spatial grid was used which covered all space from the origin at $r = 0$ up to some radius outside the cloud. The used radial coordinate transformation was $r = \ell^{1+\alpha}, \quad \alpha \geq 0$, which increases the number of cells on the inner part of the grid when $\alpha > 0$. The test results are summarized in Section 3.1.4. Apart from the artefacts near $r = 0$, the variable grid (grid with variable radial cell widths, $\alpha > 0$) produces similar results as the constant grids (grids with constant radial cell widths, $\alpha = 0$). This suggests

that the observed problems relate to the numerical method itself, rather than the variable grid.

Although it was attempted to reproduce simulation results of Larson [8] and Foster&Chevalier, this only succeeded to a certain level. Both simulations clearly reproduce the $\rho \sim r^{-2}$ dependence that characterises the mass density at the outer part of the collapsing cloud. However, both Larson and Foster&Chevalier were able to get their simulations running much closer to $r = 0$ than the Roe solver could. Verification of the observed Mach -3.3 central infall velocity by Foster&Chevalier was not possible.

Here is a summary of the unexpected behaviour of the computer model:

- At the beginning of each simulation, in the centermost cell of the radial grid, near $r = 0$, an unphysical deviation in the gas state variables appears and maintains. A number of neighbouring cells are also effected.
- The deviation acts as a source of pressure waves, which travel outward on the grid, reflecting on steep density gradients. Hence, the state of the whole grid is affected.
- Repeating the simulation with increased resolution (number of cells) near $r = 0$ enhances the deviation. Decreasing the resolution reduces the deviation, until it disappears.

It is at the moment uncertain what causes this behaviour. Some possible causes are:

- In the numerical calculations, the volume of a cell with its cell centre at ℓ and width $\Delta\ell$ is approximated by $r(\ell)^2 r'(\ell)\Delta\ell$. This approximation becomes worse when ℓ becomes comparable to $\Delta\ell$. This is the case near $r = 0$, where the deviation is observed.
- The gas state at the geometrical cell centre ℓ is chosen to represent the average state of the whole cell (see Section 2.4.2). However, according to Eq. (2.84), the average state is found by integrating the product of the state and the volume term over the whole cell. Therefore, it might be more valid to use the centre of volume (which is equal to the centre of gravity, when assuming a constant mass density within each cell) instead of the geometrical cell centre to approximate the average cell state. Note that the integral in (2.84) cannot be calculated, because the state is not known at every point within the cell.
- The computer model might contain a bug, which induces a deviation at the innermost cell. If true, the bug is most probably related to the calculation of the inner boundary condition, as this explains the local character of the deviation.

Problems as the ones observed, are also described by others using curvilinear grids, such as Blondin&Lufkin (1993). They made use of a specially adapted method to numerically solve the Euler equations near coordinate singularities, developed by Mönchmeyer&Müller (1989). This method focuses on undoing the errors that are made in the approximations when r (or ℓ) is of the same order of magnitude as Δr (or $\Delta\ell$). One improvement is choosing cell centres based on volume rather than geometry.

Before any further attempts are made to simulate gravitational collapse, it is crucial to resolve the problems that persist in the innermost cell of the grid while running simulations at higher resolution. It is only then that a fair comparison can be made between the performance of the constant grids and the variable grids.

Additional testing of the computer model might identify the source(s) of the observed problems. However, this will not be part of this small research project. The two main reasons for prematurely ending this research are:

- For the small research projct in Leiden's curriculum there is only a limited amount of time available.
- The main goal of the small research project is the introduction into astrophysical research, rather than a true research project where results are most important.

Although the small research project did not produce all the anticipated research results, it was successful in giving a good introduction into hydrodynamics and serving as an advancement in numerical techniques.

4.3 Future work

Highest priority is given to resolving the problems near $r = 0$. Before that, the simulation output is not to be trusted. Accuracy of the simulations might be improved by using true stationary extrapolation instead of the the approximation used in this report. Calculation of the gravitational force and potential can also be done more accurately. Furthermore, using the volume centre instead of the geometrical centre might improve accuracy as well.

The following two items are possible ways to continue the research. Some parts of these items were initially subjects of study for this report. Due to the time it took to make the model work like it does now, and the limited scope of the small research project, these subjects were not addressed. However, this might be continued by another student as subject of their small research project. The extended layout of this report was chosen to serve as a guide to quickly get acquainted to the model.

- By conservation of angular momentum, it is certain that rotation of matter plays an important role when a slowly rotating cloud collapses into a fast spinning core. Most likely, the dense core will be surrounded by a disc-like mass density distribution, from which other gravitational collapses might be triggered. This might, to some extent, be possible to simulate in a 2-dimensional axi-symmetric model, but 3-D is necessary when the spinning core is to be studied in any detail.
- The evolution of a collapsed core (e.g. a proto-stellar object) is closely related to all microscopic interactions of gas particles, not only the collisions that are assumed in a perfect gas. Simple chemistry changes the composition and the number density of the cloud. The cloud becomes opaque, because atoms capture electrons and start absorbing light. Dust particles may form, which have an even larger effect on the opacity of the cloud. Radiation from particle interactions gets trapped inside the core and heats

it up. So chemistry, radiative transfer and cooling are related topics that must be included in a serious star formation model.

4.4 Acknowledgements

First, I would like to thank Dr. Garrelt Mellema for originally suggesting this research subject and for many helpful discussions throughout the the course of this small research project. Second, I would like to thank my wife, Joanca, for her ongoing support during my study and her patience during the final stages of this research project.

Additionally, I would like to thank Prof. Dr. Vincent Icke for taking the time to accurately correct my poor English and for suggesting improvements for this report, and Drs. Erik-Jan Rijkhorst for reporting errors in a few equations.

Appendix A

Derivation of the Euler equations

In this section, the Euler equations of motion are derived for a self-gravitating, spherically symmetric cloud of gas. The method is similar to the method in Eulderink & Mellema [4]. The equations are derived by taking the classical, non-relativistic limit of a general relativistic formulation of fluid dynamics. The non-relativistic limit means that it is assumed that at all times at any position in the model:

- the mass velocity v is assumed to be small compared to the speed of light c.
- the gravitational potential Φ is assumed to be weak compared to c^2.
- the pressure P is assumed to be low compared to the rest mass energy density ρc^2.

In short: $|v| \ll c$, $\Phi \ll c^2$ and $P \ll \rho c^2$. For general relativity, we used the sign convention that is defined by Misner et al. [10] as $(-,+,-)$. This is the same as in Foster&Nightingale [5].

A.1 Derivation of the metric tensor

We start with a cartesian coordinate system in special relativity (no gravity). The space-time coordinates are $X^\mu = (ct, x, y, z)$. The metric tensor $\eta_{\mu\nu}$ is defined by:

$$c^2 \mathrm{d}\tau^2 = \eta_{\mu\nu} \mathrm{d}X^\mu \mathrm{d}X^\nu = c^2 \mathrm{d}t^2 - \mathrm{d}x^2 - \mathrm{d}y^2 - \mathrm{d}z^2 \tag{A.1}$$

$$\Rightarrow \quad \eta_{\mu\nu} = \begin{pmatrix} 1 & 0 & 0 & 0 \\ 0 & -1 & 0 & 0 \\ 0 & 0 & -1 & 0 \\ 0 & 0 & 0 & -1 \end{pmatrix} \tag{A.2}$$

Summation over pairs of equal indices is implied. Dividing (A.1) by $\mathrm{d}\tau^2$ gives:

$$\begin{aligned} c^2 &= c^2 \left(\frac{\mathrm{d}t}{\mathrm{d}\tau}\right)^2 - \left(\frac{\mathrm{d}x}{\mathrm{d}\tau}\right)^2 - \left(\frac{\mathrm{d}y}{\mathrm{d}\tau}\right)^2 - \left(\frac{\mathrm{d}z}{\mathrm{d}\tau}\right)^2 \\ &= \left(\frac{\mathrm{d}t}{\mathrm{d}\tau}\right)^2 \left(c^2 - \left[{v_x}^2 + {v_y}^2 + {v_z}^2\right]\right) \\ &\equiv \gamma^2 \left(c^2 - v^2\right) \qquad \text{(A.3)} \\ \Rightarrow \quad \gamma &= \frac{1}{\sqrt{1 \quad \frac{v^2}{c^2}}}, \quad v = \sqrt{{v_x}^2 + {v_y}^2 + {v_z}^2} \qquad \text{(A.4)} \end{aligned}$$

A dot above a variable means the time derivative of this variable. v is the length of the classical velocity vector (v_x, v_y, v_z). In the classical limit $v \ll c$, so $\gamma \approx 1 + \frac{1}{2}(v^2/c^2)$.

Adding gravity changes the geometry of space-time, and therefore the appearance of the metric tensor. In the classical limit (weak-field limit, $\Phi \ll c^2$), the influence of the gravitational field can be written as a first order perturbation $h_{\mu\nu}$ on the special-relativistic metric tensor $\eta_{\mu\nu}$:

$$\begin{aligned} h_{\mu\nu} &= \begin{pmatrix} \frac{2\Phi}{c^2} & 0 & 0 & 0 \\ 0 & \frac{2\Phi}{c^2} & 0 & 0 \\ 0 & 0 & \frac{2\Phi}{c^2} & 0 \\ 0 & 0 & 0 & \frac{2\Phi}{c^2} \end{pmatrix} \\ \Rightarrow \quad g_{\mu\nu} = \eta_{\mu\nu} + h_{\mu\nu} &= \begin{pmatrix} 1 + \frac{2\Phi}{c^2} & 0 & 0 & 0 \\ 0 & -1 + \frac{2\Phi}{c^2} & 0 & 0 \\ 0 & 0 & -1 + \frac{2\Phi}{c^2} & 0 \\ 0 & 0 & 0 & -1 + \frac{2\Phi}{c^2} \end{pmatrix} \qquad \text{(A.5)} \end{aligned}$$

This result is equivalent to [4], Equation (11.3).

Because of spherical symmetry, it is convenient to use spherical spatial coordinates (r, θ, ϕ) instead of cartesian spatial coordinates (x, y, z). In this report, a generic coordinate ℓ is used instead of the radial distance coordinate r. It is required that the transformation $\ell \to r \equiv r(\ell)$ has an inverse transformation $r \to \ell \equiv \ell(r)$. Our new space-time coordinates are given by:

$$\hat{X}^\mu = (ct, \ell, \theta, \phi) \qquad \text{(A.6)}$$

In terms of these coordinates, the cartesian space-time coordinates are given by:

$$X^\mu = (ct, r\sin(\theta)\cos(\phi), r\sin(\theta)\sin(\phi), r\cos(\theta)) \qquad \text{(A.7)}$$

The new metric tensor becomes:

$$\hat{g}_{\mu\nu} = \frac{\partial X^\alpha}{\partial \hat{X}^\mu} \frac{\partial X^\beta}{\partial \hat{X}^\nu} g_{\alpha\beta} \approx \begin{pmatrix} 1 + \frac{2\Phi}{c^2} & 0 & 0 & 0 \\ 0 & -r'^2\left[1 - \frac{2\Phi}{c^2}\right] & 0 & 0 \\ 0 & 0 & -r^2 & 0 \\ 0 & 0 & 0 & -r^2\sin^2(\theta) \end{pmatrix} \qquad \text{(A.8)}$$

We use r' as short notation for $\partial r(\ell)/\partial \ell$. Lorentz-invariance implies:

$$\begin{aligned} c^2\mathrm{d}\tau^2 &= \hat{g}_{\mu\nu}\mathrm{d}\hat{X}^\mu \mathrm{d}\hat{X}^\nu \\ &= \left[1 + \frac{2\Phi}{c^2}\right] c^2\mathrm{d}t^2 - r'^2\left[1 - \frac{2\Phi}{c^2}\right]\mathrm{d}\ell^2 - r^2\mathrm{d}\theta^2 - r^2\sin^2(\theta)\mathrm{d}\phi^2 \qquad \text{(A.9)} \end{aligned}$$

Dividing (A.9) by $\mathrm{d}\tau^2$ gives:

$$\begin{aligned} c^2 &= \left[1+\frac{2\Phi}{c^2}\right] c^2 \left(\frac{\mathrm{d}t}{\mathrm{d}\tau}\right)^2 - r'^2 \left[1-\frac{2\Phi}{c^2}\right] \left(\frac{\mathrm{d}\ell}{\mathrm{d}\tau}\right)^2 \\ &\quad -r^2 \left(\frac{\mathrm{d}\theta}{\mathrm{d}\tau}\right)^2 - r^2 \sin^2(\theta) \left(\frac{\mathrm{d}\phi}{\mathrm{d}\tau}\right)^2 \\ &= \left(\frac{\mathrm{d}t}{\mathrm{d}\tau}\right)^2 \left(\left[1+\frac{2\Phi}{c^2}\right] c^2 - r'^2 \left[1-\frac{2\Phi}{c^2}\right] {v_\ell}^2 - r^2 {v_\theta}^2 - r^2 \sin^2(\theta) {v_\phi}^2 \right) \\ &\equiv \hat{\gamma}^2 \left(c^2 - \hat{q}^2\right) \\ \Rightarrow \quad \hat{\gamma} &= \frac{1}{\sqrt{1-\frac{\hat{q}^2}{c^2}}}, \quad \hat{q} \equiv -2\Phi - r'^2 \frac{2\Phi}{c^2} {v_\ell}^2 + \hat{v}^2 \qquad \text{(A.10)} \\ \Rightarrow \quad \hat{v} &= \sqrt{r'^2 {v_\ell}^2 + r^2 {v_\theta}^2 + r^2 \sin^2(\theta) {v_\phi}^2} \qquad \text{(A.11)} \end{aligned}$$

$\hat{v}$ is the length of the classical velocity vector $(v_r = r'v_\ell, rv_\theta, r\sin(\theta)v_\phi)$ in spherical coordinates. In the classical limit $\hat{v} \ll c$ and $\Phi \ll c^2$, so $\hat{q} \approx -2\Phi + \hat{v}^2$ and $\hat{\gamma} \approx 1 - (\Phi/c^2) + \frac{1}{2}(\hat{v}^2/c^2)$.

A.2 Derivation of the equations of motion

From now on the hats on the tensors are dropped, so X^μ refers to the space-time vector in (A.6) and $g_{\mu\nu}$ refers to the metric tensor in (A.8). Relativity theory allows mass to be converted into other forms of energy and vice versa. For the classical limit it is assumed that mass and energy will not convert into each other, because the energy densities within the model are too low. Because mass is conserved, the general relativistic version of the mass continuity equation is true:

$$J^\mu{}_{,\mu} \equiv \frac{\partial J^\mu}{\partial X^\mu} + \Gamma^\mu_{\mu\nu} J^\nu = 0 \qquad \text{(A.12)}$$

This equation states that the covariant derivative (denoted by ';') of the relativistic mass flux tensor J^μ is zero. J^μ is given by:

$$J^\mu = \rho \frac{\partial X^\mu}{\partial \tau} \equiv \gamma \rho U^\mu \qquad \text{(A.13)}$$

$\Gamma^\mu_{\lambda\nu}$ is the Christoffel symbol, given by:

$$\Gamma^\mu_{\lambda\nu} = \frac{1}{2} g^{\mu\chi} \left(\frac{\partial g_{\chi\nu}}{\partial X^\lambda} + \frac{\partial g_{\lambda\chi}}{\partial X^\nu} - \frac{\partial g_{\lambda\nu}}{\partial X^\chi} \right) \qquad \text{(A.14)}$$

$g^{\mu\nu}$ is the contravariant metric tensor, opposed to the covariant metric tensor $g_{\mu\nu}$. In matrix notation, $g^{\mu\nu}$ is the inverse of $g_{\mu\nu}$. Using the classical limit $\Phi \ll c^2$, it follows that:

$$g^{\mu\nu} = \begin{pmatrix} 1-\frac{2\Phi}{c^2} & 0 & 0 & 0 \\ 0 & -\frac{1}{r'^2}\left[1+\frac{2\Phi}{c^2}\right] & 0 & 0 \\ 0 & 0 & -\frac{1}{r^2} & 0 \\ 0 & 0 & 0 & -\frac{1}{r^2\sin^2(\theta)} \end{pmatrix} \qquad \text{(A.15)}$$

Now the following relation exists (e.g. see Foster&Nightingale [5], (2.38)):

$$\Gamma^{\mu}_{\mu\nu} = \frac{1}{\sqrt{-g}} \frac{\partial}{\partial X^{\nu}} \left(\sqrt{-g}\right) \tag{A.16}$$

Here, g is the determinant of $g_{\mu\nu}$. Using the classical limit and (A.8) it follows that:

$$g = -r^4 r'^2 \sin^2(\theta) \quad \Rightarrow \quad \sqrt{-g} = r^2 r' \sin(\theta) \tag{A.17}$$

$\sqrt{-g}$ is called the volume term. Combining (A.12) and (A.16) gives the Euler equation of mass in relativistic form:

$$\frac{\partial J^{\mu}}{\partial X^{\mu}} + \frac{1}{\sqrt{-g}} \frac{\partial}{\partial X^{\nu}} \left(\sqrt{-g}\right) J^{\nu} = 0 \quad \Leftrightarrow \quad \frac{\partial}{\partial X^{\mu}} \left(\sqrt{-g} J^{\mu}\right) = 0 \tag{A.18}$$

In general relativity, the motion of matter is governed by the energy-momentum-stress (EMS) tensor $T^{\mu\nu}$:

$$\begin{aligned} T^{\mu\nu} &= \frac{e_{rel} + P}{c^2} \frac{\partial X^{\mu}}{\partial \tau} \frac{\partial X^{\nu}}{\partial \tau} - P g^{\mu\nu} = \gamma^2 \frac{e_{rel} + P}{c^2} U^{\mu} U^{\nu} - P g^{\mu\nu} \\ &= \gamma^2 \left(\rho + \frac{\Gamma}{\Gamma - 1} \frac{P}{c^2}\right) U^{\mu} U^{\nu} - P g^{\mu\nu} \end{aligned} \tag{A.19}$$

The EMS tensor describes the energy content of the gas. In relativity theory, mass and energy are equivalent. The relativistic total energy density e_{rel} is the relativistic equivalent of the classical total energy density in (2.9):

$$e_{rel} = \rho c^2 + \frac{P}{\Gamma - 1} \equiv e_{\rho} + e_{int} \tag{A.20}$$

e_{ρ} contains both the rest mass energy and the kinetic energy of the gas (although the last is not so obvious to recognise), while e_{int} is the internal gas energy of (2.5). One of the central theorems of general relativity is that the covariant derivative of the EMS tensor is zero:

$$\begin{aligned} &T^{\mu\nu}{}_{;\mu} \equiv \frac{\partial T^{\mu\nu}}{\partial X^{\mu}} + \Gamma^{\mu}_{\mu\chi} T^{\chi\nu} + \Gamma^{\nu}_{\mu\chi} T^{\mu\chi} = 0 \quad \Leftrightarrow \\ &\frac{\partial}{\partial X^{\mu}} \left(\sqrt{-g} T^{\mu\nu}\right) = -\sqrt{-g} \Gamma^{\nu}_{\mu\chi} T^{\mu\chi} \end{aligned} \tag{A.21}$$

Again, (A.16) was used. The four equations (ν runs from 0 to 3) in (A.21) have a similar appearance as (A.18). The equation with $\nu = 0$ is the Euler equation of energy in relativistic form. The equations with $\nu = 1, 2, 3$ are the Euler equations of momentum in relativistic form for the ℓ-direction, θ-direction and ϕ-direction.

The Euler equation of energy does contain the rest mass energy. However, conservation of rest mass (energy) is incorporated in the Euler equation of mass (Eq. (A.18)). As the rest mass energy overwhelms the other forms of energy (kinetic and internal), it is necessary to remove its contribution from the Euler equation of energy by replacing $T^{\mu 0}$ with $\widetilde{T}^{\mu 0}$:

$$\begin{aligned} T^{\mu 0} \rightarrow \widetilde{T}^{\mu 0} &= T^{\mu 0} - c J^{\mu} \\ &= \gamma^2 \left(\rho + \frac{\Gamma}{\Gamma - 1} \frac{P}{c^2}\right) U^{\mu} U^{0} - P g^{\mu 0} - c \gamma \rho U^{\mu} \\ &= \left(\gamma \left[\gamma - 1\right] \rho c + \gamma^2 \frac{\Gamma}{\Gamma - 1} \frac{P}{c}\right) U^{\mu} - P g^{\mu 0} \end{aligned} \tag{A.22}$$

Subtraction of c times (A.18) from (A.21) with $\nu = 0$ gives the new Euler equation of energy:

$$\begin{aligned}
&\frac{\partial}{\partial X^\mu}\left(\sqrt{-g}\left[T^{\mu 0} - cJ^\mu\right]\right) = -\sqrt{-g}\Gamma^0_{\mu\chi}T^{\mu\chi} \quad \Rightarrow \\
&\frac{\partial}{\partial X^\mu}\left(\sqrt{-g}\widetilde{T}^{\mu 0}\right) = -\sqrt{-g}\Gamma^0_{\mu\chi}T^{\mu\chi}
\end{aligned} \tag{A.23}$$

Note that the EMS tensor on the right of the equation has no tilde. The Euler equations of momentum keep the same form.

Because of spherical symmetry and non-rotation of the model used (see Section 2.2.1), ρ, P and Φ do not depend on θ or ϕ and v_θ and v_ϕ are both zero (or $U^{\mu=2,3} = 0$). From (A.13), it follows directly that $J^{\mu=2,3} = 0$. Using (A.18), the Euler equation of mass becomes:

$$\begin{aligned}
&\frac{\partial}{\partial X^0}\left(\sqrt{-g}J^0\right) + \frac{\partial}{\partial X^1}\left(\sqrt{-g}J^1\right) = 0 \quad \Leftrightarrow \\
&\frac{\partial}{\partial X^0}\left(\sqrt{-g}\gamma\rho U^0\right) + \frac{\partial}{\partial X^1}\left(\sqrt{-g}\gamma\rho U^1\right) = 0 \quad \Leftrightarrow \\
&\frac{\partial}{\partial t}\left(\sqrt{-g}\gamma\rho\right) + \frac{\partial}{\partial \ell}\left(\sqrt{-g}\gamma\rho v_\ell\right) = 0
\end{aligned} \tag{A.24}$$

In the non-relativistic limit, using γ from (A.11) and $\sqrt{-g}$ from (A.17), this becomes:

$$\frac{\partial}{\partial t}\left(r^2 r'\rho\right) + \frac{\partial}{\partial \ell}\left(r^2 r'\rho v_\ell\right) = 0 \tag{A.25}$$

This is the classical (non-relativistic) Euler equation of mass.

Determining the Euler equations of energy and momentum in the non-relativistic limit requires the components of the Christoffel symbol $\Gamma^\mu_{\lambda\nu}$, EMS tensor $T^{\mu\nu}$ and modified EMS tensor $\widetilde{T}^{\mu 0}$ in the non-relativistic limit. Using (A.14), the non-zero components of the Christoffel symbol $\Gamma^\mu_{\lambda\nu}$ in the the non-relativistic limit are:

$$\begin{aligned}
&\Gamma^0_{00} = \frac{1}{c^3}\frac{\partial\Phi}{\partial t}, && \Gamma^0_{01} = \Gamma^0_{10} = \frac{r'}{c^2}\frac{\partial\Phi}{\partial r}, && \Gamma^0_{11} = -\frac{r'^2}{c^3}\frac{\partial\Phi}{\partial t}, \\
&\Gamma^1_{00} = \frac{1}{r'c^2}\frac{\partial\Phi}{\partial r}, && \Gamma^1_{01} = \Gamma^1_{10} = -\frac{1}{c^3}\frac{\partial\Phi}{\partial t}, && \Gamma^1_{11} = \frac{r''}{r'}, \\
&\Gamma^1_{22} = -\frac{r}{r'}, && \Gamma^2_{12} = \Gamma^2_{21} = \frac{r'}{r}, && \Gamma^1_{33} = -\frac{r\sin^2(\theta)}{r'}, \\
&\Gamma^3_{13} = \Gamma^3_{31} = \frac{r'}{r}, && \Gamma^2_{33} = -\sin(\theta)\cos(\theta), && \Gamma^3_{23} = \Gamma^3_{32} = \frac{\cos(\theta)}{\sin(\theta)}
\end{aligned} \tag{A.26}$$

Using (A.19), the non-zero components of the EMS tensor $T^{\mu\nu}$ in the the non-relativistic limit are:

$$\begin{aligned}
&T^{00} = \rho c^2, && T^{01} = T^{10} = \rho c v_\ell, && T^{11} = \rho {v_\ell}^2 + \frac{P}{r'^2} \\
&T^{22} = \frac{P}{r^2}, && T^{33} = \frac{P}{r^2\sin^2(\theta)}
\end{aligned} \tag{A.27}$$

Using (A.22), the non-zero components of the modified EMS tensor $\widetilde{T}^{\mu 0}$ in the the non-relativistic limit are:

$$\begin{aligned}\widetilde{T}^{00} &= \left(\frac{1}{2}r'^2{v_\ell}^2 - \Phi\right)\rho + \frac{\Gamma}{\Gamma-1}P - P \\ &= \frac{1}{2}\rho r'^2{v_\ell}^2 + \frac{P}{\Gamma-1} - \rho\Phi = e - \rho\Phi \end{aligned} \tag{A.28}$$

$$\begin{aligned}\widetilde{T}^{10} &= \left(\left[\frac{1}{2}r'^2{v_\ell}^2 - \Phi\right]\frac{\rho}{c} + \frac{\Gamma}{\Gamma-1}\frac{P}{c}\right)v_\ell \\ &= \left(\frac{1}{2}\rho r'^2{v_\ell}^2 + \frac{\Gamma}{\Gamma-1}P - \rho\Phi\right)\frac{v_\ell}{c} = (e + P - \rho\Phi)\frac{v_\ell}{c} \end{aligned} \tag{A.29}$$

Here, e is the classical total energy density of (2.33):

$$e = \frac{1}{2}\rho r'^2{v_\ell}^2 + \frac{P}{\Gamma-1} = \frac{1}{2}\rho{v_r}^2 + \frac{P}{\Gamma-1} \tag{A.30}$$

With these non-relativistic limits known, the Euler equation of energy (Eq. (A.23)) becomes:

$$\begin{aligned}&\frac{\partial}{\partial X^0}\left(\sqrt{-g}\widetilde{T}^{00}\right) + \frac{\partial}{\partial X^1}\left(\sqrt{-g}\widetilde{T}^{10}\right) \\ &\qquad = -\sqrt{-g}\left[\Gamma^0_{00}T^{00} + \Gamma^0_{01}T^{01} + \Gamma^0_{10}T^{10} + \Gamma^0_{11}T^{11}\right] \quad \Rightarrow \\ &\frac{\partial}{\partial t}\left(r^2r'\left[e - \rho\Phi\right]\right) + \frac{\partial}{\partial \ell}\left(r^2r'\left[e + P - \rho\Phi\right]v_\ell\right) \\ &\qquad = r^2r'\left[-\rho\frac{\partial\Phi}{\partial t} - 2\rho r' v_\ell\frac{\partial\Phi}{\partial r}\right] \end{aligned} \tag{A.31}$$

This is the classical (non-relativistic) Euler equation of energy. Likewise, using (A.21) with $\nu = 1$, the Euler equation of momentum in the ℓ-direction becomes:

$$\begin{aligned}&\frac{\partial}{\partial X^0}\left(\sqrt{-g}T^{01}\right) + \frac{\partial}{\partial X^1}\left(\sqrt{-g}T^{11}\right) = -r^2r'\left[\Gamma^1_{00}T^{00} + \Gamma^1_{01}T^{01}\right. \\ &\qquad \left. + \Gamma^1_{10}T^{10} + \Gamma^1_{11}T^{11} + \Gamma^1_{22}T^{22} + \Gamma^1_{33}T^{33}\right] \quad \Rightarrow \\ &\frac{\partial}{\partial t}\left(r^2r'\rho v_\ell\right) + \frac{\partial}{\partial \ell}\left(r^2r'\left[\rho{v_\ell}^2 + \frac{P}{r'^2}\right]v_\ell\right) \\ &\qquad = r^2r'\left[\frac{2P}{rr'} - \frac{r''}{r'}\left\{\rho{v_\ell}^2 + \frac{P}{r'^2}\right\} - \frac{\rho}{r'}\frac{\partial\Phi}{\partial r}\right] \end{aligned} \tag{A.32}$$

This is the classical (non-relativistic) Euler equation of momentum in the ℓ-direction. Using (A.21) with $\nu = 2$, the Euler equation of momentum in the θ-direction becomes:

$$\begin{aligned}&\frac{\partial}{\partial X^2}\left(\sqrt{-g}T^{22}\right) = \sqrt{-g}\left[\Gamma^2_{33}T^{33}\right] \quad \Rightarrow \\ &\frac{\partial}{\partial\theta}\left(r'\sin(\theta)P\right) = \cos(\theta)r'P \quad \Rightarrow \quad \frac{\partial P}{\partial\theta} = 0 \end{aligned} \tag{A.33}$$

This is a confirmation of the model assumption that P does not depend on θ, meaning P does not change in the θ-direction. Using (A.21) with $\nu = 3$, the

Euler equation of momentum in the ϕ-direction becomes:

$$\frac{\partial}{\partial X^3}\left(\sqrt{-g}T^{33}\right) = 0 \quad \Rightarrow \quad \frac{\partial P}{\partial \phi} = 0 \tag{A.34}$$

This is a confirmation of the model assumption that P does not depend on ϕ either. It is clear that (A.33) and (A.34) are not really momentum equation like (A.32) is, but that was to be expected as there is no mass moving in either the θ- or the ϕ-direction.

A.3 Alternative Euler equation of energy

Summarizing, the classical (non-relativistic) Euler equations of mass, momentum and energy are given by (A.25), (A.32) and (A.31) respectively:

$$\frac{\partial}{\partial t}\left(r^2 r' \rho\right) + \frac{\partial}{\partial \ell}\left(r^2 r' \rho v_\ell\right) = 0 \tag{A.35}$$

$$\frac{\partial}{\partial t}\left(r^2 r' \rho v_\ell\right) + \frac{\partial}{\partial \ell}\left(r^2 r'\left[\rho {v_\ell}^2 + \frac{P}{r'^2}\right] v_\ell\right) = r^2 r'\left[\frac{2P}{r r'} - \frac{r''}{r'}\left\{\rho {v_\ell}^2 + \frac{P}{r'^2}\right\} - \frac{\rho}{r'}\frac{\partial \Phi}{\partial r}\right] \tag{A.36}$$

$$\frac{\partial}{\partial t}\left(r^2 r'\left[e - \rho\Phi\right]\right) + \frac{\partial}{\partial \ell}\left(r^2 r'\left[e + P - \rho\Phi\right] v_\ell\right) = r^2 r'\left[-\rho\frac{\partial \Phi}{\partial t} - 2\rho r' v_\ell \frac{\partial \Phi}{\partial r}\right] \tag{A.37}$$

Here, e is given by (A.30).

Now, a simplification of the energy equation is presented. Using the product rule for differentiation gives:

$$\frac{\partial}{\partial t}\left(r^2 r' \rho\Phi\right) + \frac{\partial}{\partial \ell}\left(r^2 r' \rho\Phi v_\ell\right) = \Phi\frac{\partial}{\partial t}\left(r^2 r' \rho\right) + r^2 r' \rho\frac{\partial \Phi}{\partial t} + \Phi\frac{\partial}{\partial \ell}\left(r^2 r' \rho v_\ell\right) + r^2 r' \rho v_\ell \frac{\partial \Phi}{\partial \ell} \tag{A.38}$$

The first and third term on the right cancel due to (A.35). Rewriting the partial derivative in the fourth term in terms of r gives:

$$\frac{\partial}{\partial t}\left(r^2 r' \rho\Phi\right) + \frac{\partial}{\partial \ell}\left(r^2 r' \rho\Phi v_\ell\right) = r^2 r'\left[\rho\frac{\partial \Phi}{\partial t} + \rho r' v_\ell \frac{\partial \Phi}{\partial r}\right] \tag{A.39}$$

Adding (A.39) twice to (A.37) gives:

$$\frac{\partial}{\partial t}\left(r^2 r'\left[e + \rho\Phi\right]\right) + \frac{\partial}{\partial \ell}\left(r^2 r'\left[e + P + \rho\Phi\right] v_\ell\right) = r^2 r' \rho\frac{\partial \Phi}{\partial t} \tag{A.40}$$

The first term on the left hand side is the time derivative of the (familiar) sum of the total energy density e and the potential energy density $\rho\Phi$. If Φ is assumed to vary very slowly in time compared to ρ, P and v_r, the right hand side of the equation can effectively be set to zero. However, during a gravitational collapse,

this assumption is not likely to hold. Therefore, we look at another possible equation. Adding (A.39) once to (A.37) gives:

$$\frac{\partial}{\partial t}\left(r^2 r' e\right) + \frac{\partial}{\partial \ell}\left(r^2 r' \left[e + P\right] v_\ell\right) = -r^2 r' \rho r' v_\ell \frac{\partial \Phi}{\partial r} \tag{A.41}$$

This is the spherical analogy of Shu [15], (2.32). Using (A.41) instead of (A.37) or (A.40) has several advantages:

- The gravitational force $F = -\frac{\partial \Phi}{\partial r}$ in the right hand side of (A.41) is easy to calculate in a spherically symmetric system (see Section 2.4.6).
- The gravitational force is also used in the right hand side of (A.36) and needs only to be calculated once.
- The gravitational potential Φ itself has disappeared from the energy equation altogether.
- The time derivative of the gravitational potential has also disappeared from the energy equation.

A.4 Summary

In the case of a spherically symmetric, non-rotating cloud of ideal gas, the classical, non-relativistic Euler equations of motion are given by (A.25), (A.32) and (A.41):

$$\frac{\partial}{\partial t}\left(r^2 r' \rho\right) + \frac{\partial}{\partial \ell}\left(r^2 r' \rho v_\ell\right) = 0 \tag{A.42}$$

$$\frac{\partial}{\partial t}\left(r^2 r' \rho v_\ell\right) + \frac{\partial}{\partial \ell}\left(r^2 r' \left[\rho {v_\ell}^2 + \frac{P}{r'^2}\right] v_\ell\right) = r^2 r' \left[\frac{2P}{r r'} - \frac{r''}{r'}\left\{\rho {v_\ell}^2 + \frac{P}{r'^2}\right\} - \frac{\rho}{r'}\frac{\partial \Phi}{\partial r}\right] \tag{A.43}$$

$$\frac{\partial}{\partial t}\left(r^2 r' e\right) + \frac{\partial}{\partial \ell}\left(r^2 r' \left[e + P\right] v_\ell\right) = -r^2 r' \rho r' v_\ell \frac{\partial \Phi}{\partial r} \tag{A.44}$$

Here, $r = r(\ell)$ is the radial distance as a function of a new radial coordinate ℓ, $r' = \partial r / \partial \ell$, $r'' = \partial^2 r / \partial \ell^2$ and e is the total energy density of the gas, given by (A.30):

$$e = \frac{1}{2}\rho r'^2 {v_\ell}^2 + \frac{P}{\Gamma - 1} \tag{A.45}$$

In the simple case that $r = \ell$, the Euler equations reduce to:

$$\frac{\partial}{\partial t}\left(r^2 \rho\right) + \frac{\partial}{\partial r}\left(r^2 \rho v_r\right) = 0 \tag{A.46}$$

$$\frac{\partial}{\partial t}\left(r^2 \rho v_r\right) + \frac{\partial}{\partial r}\left(r^2 \left[\rho {v_r}^2 + P\right]\right) = r^2 \left[\frac{2P}{r} - \rho \frac{\partial \Phi}{\partial r}\right] \tag{A.47}$$

$$\frac{\partial}{\partial t}\left(r^2 e\right) + \frac{\partial}{\partial r}\left(r^2 \left[e + P\right] v_r\right) = -r^2 \rho v_r \frac{\partial \Phi}{\partial r} \tag{A.48}$$

$$e = \frac{1}{2}\rho {v_r}^2 + \frac{P}{\Gamma - 1} \tag{A.49}$$

Appendix B

Other derivations

B.1 Eigenvalues and eigenvectors of the Jacobian

In this section, the eigenvalues and eigenvectors of the Jacobian of the Euler equations are derived. The Euler equations are given by (A.42)-(A.44). In Section A.3 it was shown that the Euler equation of energy is not uniquely determined, because (A.39) can be added (or subtracted) multiple times to (or from) (A.44). A more general formulation is the case where (A.39) is added K times to (A.44), where K can be any real number:

$$\frac{\partial}{\partial t}\left(r^2 r'\left[e+K\rho\Phi\right]\right)+\frac{\partial}{\partial \ell}\left(r^2 r'\left[e+P+K\rho\Phi\right]v_\ell\right) = r^2 r'\left[K\rho\frac{\partial\Phi}{\partial t}+(K-1)\rho r' v_\ell\frac{\partial\Phi}{\partial r}\right] \tag{B.1}$$

When using the vector notation of (2.51), the state vector $\mathbf{W}$, flux vector $\mathbf{F}$ and source vector $\mathbf{S}$ become:

$$\mathbf{W}=r^2 r'\begin{pmatrix}\rho\\ \rho v_\ell\\ e+K\rho\Phi\end{pmatrix}=r^2 r'\begin{pmatrix}\rho\\ \rho v_\ell\\ \frac{1}{2}\rho r'^2 {v_\ell}^2+\frac{P}{\Gamma-1}+K\rho\Phi\end{pmatrix} \tag{B.2}$$

$$\mathbf{F}=r^2 r'\begin{pmatrix}\rho v_\ell\\ \rho {v_\ell}^2+\frac{P}{r'^2}\\ \left[e+P+K\rho\Phi\right]v_\ell\end{pmatrix}=r^2 r'\begin{pmatrix}\rho v_\ell\\ \rho {v_\ell}^2+\frac{P}{r'^2}\\ \frac{1}{2}\rho r'^2 {v_\ell}^3+\frac{\Gamma P}{\Gamma-1}v_\ell+K\rho\Phi v_\ell\end{pmatrix} \tag{B.3}$$

$$\mathbf{S}=r^2 r'\begin{pmatrix}0\\ \frac{2P}{r}-\rho\frac{\partial\Phi}{\partial r}\\ K\rho\frac{\partial\Phi}{\partial t}+(K-1)\rho r' v_\ell\frac{\partial\Phi}{\partial r}\end{pmatrix} \tag{B.4}$$

The Jacobian $\mathbb{A}$ is given by $\mathbb{A}=\partial\mathbf{F}/\partial\mathbf{W}$. Naming the elements of the vector $\mathbf{W}$ (W_1,W_2,W_3) and the elements of $\mathbf{F}$ (F_1,F_2,F_3), it follows that $\mathbb{A}$ is a Jacobian matrix with elements $A_{ab}=\partial F_a/\partial F_b$ with $a,b\in\{1,2,3\}$. To calculate

this matrix, $\mathbf{F}$ needs to be expressed in terms of $\mathbf{W}$:

$$\mathbf{F} = \begin{pmatrix} W_2 \\ (\Gamma+1)\frac{{W_2}^2}{2W_1} + (\Gamma-1)\frac{W_3 - KW_1\Phi}{{r'}^2} \\ \Gamma\frac{W_2 W_3}{W_1} - (\Gamma-1)\left(\frac{{r'}^2{W_2}^3}{2{W_1}^2} + KW_2\Phi\right) \end{pmatrix} \tag{B.5}$$

The Jacobian matrix $\mathbb{A}$ becomes:

$$\begin{aligned} \mathbb{A} &= \begin{pmatrix} 0 & 1 & 0 \\ (\Gamma-3)\frac{{W_2}^2}{2W_1} - (\Gamma-1)\frac{K\Phi}{{r'}^2} & -(\Gamma-3)\frac{W_2}{W_1} & (\Gamma-1)\frac{1}{{r'}^2} \\ (\Gamma-1)\frac{{r'}^2{W_2}^3}{{W_1}^3} - \Gamma\frac{W_2 W_3}{{W_1}^2} & -(\Gamma-1)\left(\frac{3{r'}^2{W_2}^2}{2{W_1}^2} + K\Phi\right) + \Gamma\frac{W_3}{W_1} & \Gamma\frac{W_2}{W_1} \end{pmatrix} \\ &= \begin{pmatrix} 0 & 1 & 0 \\ (\Gamma-3)\frac{{v_\ell}^2}{2} - (\Gamma-1)\frac{K\Phi}{{r'}^2} & -(\Gamma-3)v_\ell & (\Gamma-1)\frac{1}{{r'}^2} \\ \left((\Gamma-2)\frac{1}{2}{r'}^2{v_\ell}^2 - \Gamma K\Phi - \frac{\Gamma}{\Gamma-1}\frac{P}{\rho}\right)v_\ell & -(\Gamma+3)\frac{1}{2}{r'}^2{v_\ell}^2 + K\Phi + \frac{\Gamma}{\Gamma-1}\frac{P}{\rho} & \Gamma v_\ell \end{pmatrix} \end{aligned} \tag{B.6}$$

The eigenvalues λ_a of $\mathbb{A}$ are found by solving the characteristic equation:

$$\begin{aligned} &\det(\mathbb{A} - \lambda_a\mathbb{I}) = 0 \quad \Rightarrow \\ &{\lambda_a}^3 + 3v_\ell{\lambda_a}^2 + \left(\frac{\Gamma P}{{r'}^2\rho} - 3{v_\ell}^2\right)\lambda_a + \left({v_\ell}^2 - \frac{\Gamma P}{{r'}^2\rho}\right)v_\ell = 0 \quad \Rightarrow \\ &\lambda_1 = v_\ell \\ &\lambda_2 = v_\ell + \frac{1}{r'}\sqrt{\frac{\Gamma P}{\rho}} = v_\ell + \frac{c_s}{r'} \\ &\lambda_3 = v_\ell - \frac{1}{r'}\sqrt{\frac{\Gamma P}{\rho}} = v_\ell - \frac{c_s}{r'} \end{aligned} \tag{B.7}$$

Here, det() is the determinant and $\mathbb{I}$ is the identity matrix. In the last step the sound speed c_s (2.10) was used. Note that both K and Φ do not appear in the eigenvalues. The eigenvectors $\mathbf{e}_a$ are found by solving:

$$\begin{aligned} &(\mathbb{A} - \lambda_a\mathbb{I})\,\mathbf{e}_a = \mathbf{0} \quad \Rightarrow \\ &\mathbf{e}_1 = \begin{pmatrix} 1 \\ v_\ell \\ \frac{1}{2}{r'}^2{v_\ell}^2 + K\Phi \end{pmatrix} = \begin{pmatrix} 1 \\ \lambda_1 \\ \frac{1}{2}{r'}^2{v_\ell}^2 + K\Phi \end{pmatrix} \\ &\mathbf{e}_2 = \begin{pmatrix} 1 \\ v_\ell + \frac{1}{r'}\sqrt{\frac{\Gamma P}{\rho}} \\ \frac{1}{2}{r'}^2{v_\ell}^2 + \frac{\Gamma}{\Gamma-1}\frac{P}{\rho} + K\Phi + r'v_\ell\sqrt{\frac{\Gamma P}{\rho}} \end{pmatrix} = \begin{pmatrix} 1 \\ \lambda_2 \\ \frac{e+P}{\rho} + K\Phi + r'v_\ell c_s \end{pmatrix} \\ &\mathbf{e}_3 = \begin{pmatrix} 1 \\ v_\ell - \frac{1}{r'}\sqrt{\frac{\Gamma P}{\rho}} \\ \frac{1}{2}{r'}^2{v_\ell}^2 + \frac{\Gamma}{\Gamma-1}\frac{P}{\rho} + K\Phi - r'v_\ell\sqrt{\frac{\Gamma P}{\rho}} \end{pmatrix} = \begin{pmatrix} 1 \\ \lambda_3 \\ \frac{e+P}{\rho} + K\Phi - r'v_\ell c_s \end{pmatrix} \end{aligned} \tag{B.8}$$

In this report $K = 0$ is used, so the eigenvectors reduce to:

$$\mathbf{e}_1 = \begin{pmatrix} 1 \\ \lambda_1 \\ \frac{1}{2}r'^2{v_\ell}^2 \end{pmatrix}, \quad \mathbf{e}_2 = \begin{pmatrix} 1 \\ \lambda_2 \\ \frac{e+P}{\rho} + r' v_\ell c_s \end{pmatrix}, \quad \mathbf{e}_3 = \begin{pmatrix} 1 \\ \lambda_3 \\ \frac{e+P}{\rho} - r' v_\ell c_s \end{pmatrix} \tag{B.9}$$

In the special case that $\ell = r$, the results become:

$$\lambda_1 = v_r, \qquad \lambda_2 = v_r + c_s, \qquad \lambda_3 = v_r - c_s \tag{B.10}$$

$$\mathbf{e}_1 = \begin{pmatrix} 1 \\ \lambda_1 \\ \frac{1}{2}{v_r}^2 \end{pmatrix}, \quad \mathbf{e}_2 = \begin{pmatrix} 1 \\ \lambda_2 \\ \frac{e+P}{\rho} + v_r c_s \end{pmatrix}, \quad \mathbf{e}_3 = \begin{pmatrix} 1 \\ \lambda_3 \\ \frac{e+P}{\rho} - v_r c_s \end{pmatrix} \tag{B.11}$$

B.2 Stationary solutions to the Euler equations

In this section, stationary solutions are derived for the Euler equations of motion in Section A.4. Stationary solutions represent physical configurations in which all macroscopic gas parameters are constant in time. As a result, all (partial) time derivatives of the macroscopic gas parameters are zero. Applying this to (A.42), (A.43) and (A.44) gives:

$$\frac{\partial}{\partial \ell}\left(r^2 r' \rho v_\ell\right) = 0 \tag{B.12}$$

$$\frac{\partial}{\partial \ell}\left(r^2 r'\left[\rho {v_\ell}^2 + \frac{P}{r'^2}\right]\right) = r^2 r'\left[\frac{2P}{r r'} - \frac{r''}{r'}\left\{\rho {v_\ell}^2 + \frac{P}{r'^2}\right\} - \frac{\rho}{r'}\frac{\partial \Phi}{\partial r}\right] \tag{B.13}$$

$$\frac{\partial}{\partial \ell}\left(r^2 r'\left[e + P + \rho\Phi\right] v_\ell\right) = \frac{\partial}{\partial \ell}\left(r^2 r'\left[\frac{1}{2}\rho r'^2 {v_\ell}^2 + \frac{\Gamma P}{\Gamma - 1} + \rho\Phi\right] v_\ell\right) = 0 \tag{B.14}$$

From (B.12) it follows that $r^2 r' \rho v_\ell = \textit{constant} \equiv D$ for all ℓ. This means that the mass flux $\rho v_r = \rho r' v_\ell$ through any spherical shell surface area $4\pi r^2 \sim r^2$ is conserved. From dividing (B.14) by (B.12) it follows that $\frac{1}{2}r'^2{v_\ell}^2 + \frac{\Gamma}{\Gamma-1}\frac{P}{\rho} + \Phi = \textit{constant} \equiv B$ for all ℓ. By definition of the enthalpy $II = \frac{e+P}{\rho}$ with e the total energy density from (A.45), it follows that $H + \Phi$ is a conserved quantity. Expanding the left side of (B.13) gives:

$$\begin{aligned} \frac{\partial}{\partial \ell}\left(r^2 r'\left[\rho {v_\ell}^2 + \frac{P}{r'^2}\right]\right) &= \frac{\partial}{\partial \ell}\left(\left(r^2 r' \rho v_\ell\right) v_\ell\right) + \frac{\partial}{\partial \ell}\left(\frac{r^2 P}{r'}\right) \\ &= r^2 r' \rho v_\ell \frac{\partial v_\ell}{\partial \ell} + 2rP - \frac{r^2 r'' P}{r'^2} + \frac{r^2}{r'}\frac{\partial P}{\partial \ell} \\ &= r^2 r' \rho \frac{\partial}{\partial \ell}\left(\frac{1}{2}{v_\ell}^2\right) + 2rP - \frac{r^2 r'' P}{r'^2} + \frac{r^2}{r'}\frac{\partial P}{\partial \ell} \end{aligned} \tag{B.15}$$

In the second step (B.12) is used. Expanding the right side of (B.13) gives:

$$\begin{aligned} &r^2 r'\left[\frac{2P}{r r'} - \frac{r''}{r'}\left\{\rho {v_\ell}^2 + \frac{P}{r'^2}\right\} - \frac{\rho}{r'}\frac{\partial \Phi}{\partial r}\right] \\ &\qquad = 2rP - r^2 r'' \rho {v_\ell}^2 - \frac{r^2 r'' P}{r'^2} - \frac{r^2 \rho}{r'}\frac{\partial \Phi}{\partial \ell} \end{aligned} \tag{B.16}$$

Equalizing (B.15) and (B.16) gives:

$$
\begin{aligned}
& r^2 r' \rho \frac{\partial}{\partial \ell}\left(\frac{1}{2} {v_\ell}^2\right) + \frac{r^2}{r'}\frac{\partial P}{\partial \ell} = -r^2 r'' \rho {v_\ell}^2 - \frac{r^2 \rho}{r'}\frac{\partial \Phi}{\partial \ell} \quad \Leftrightarrow \\
& \frac{\partial}{\partial \ell}\left(\frac{1}{2} r'^2 {v_\ell}^2 + \Phi\right) + \frac{1}{\rho}\frac{\partial P}{\partial \ell} = 0 \quad \Rightarrow \quad \frac{\partial}{\partial \ell}\left(-\frac{\Gamma}{\Gamma - 1}\frac{P}{\rho}\right) + \frac{1}{\rho}\frac{\partial P}{\partial \ell} = 0 \quad \Leftrightarrow \\
& \frac{\Gamma}{\rho}\frac{\partial \rho}{\partial \ell} - \frac{1}{P}\frac{\partial P}{\partial \ell} = 0 \quad \Leftrightarrow \quad \frac{\partial}{\partial \ell}\left(\ln\left(\rho^\Gamma\right) - \ln\left(P\right)\right) = 0
\end{aligned}
\tag{B.17}
$$

In the third step the conservation of B is used. From (B.17) it follows that $P/\rho^\Gamma = constant \equiv \kappa$ for all ℓ. This result is equal to (2.2), which shows that stationary solutions conserve entropy and shocks are absent.

Bibliography

[1] Binney, J. & Tremaine, S. (1987), *Galactic Dynamics*, Princeton University Press ISBN 0-691-08445

[2] Boily, C.M. & Lynden-Bell, D. (1995), *Self-similar Collapse and Accretion of Radiative Gas*, Monthly Notices of the Royal Astronomical Society, Volume 276, Pages 133-166

[3] Bradley, B.W. & Ostlie, D.A. (1996), *An Introduction to Modern Astrophysics*, Addison-Wesley Publishing Company, Inc. ISBN 0-201-54730-9

[4] Eulderink, F. & Mellema, G. (1995), *General Relativistic Hydrodynamics with a Roe Solver*, Astronomy & Astrophysics Supplement Series, Volume 110, Pages 587-623

[5] Foster, J. & Nightingale, J.D. (1995), *A Short Course in General Relativity*, Second Edition, Springer-Verlag, New York, Inc. ISBN 0-387-94295-5

[6] Foster, P.N. & Chevalier, R.A. (1993), *Gravitational Collapse of an Isothermal Sphere*, Astrophysical Journal, Volume 416, Pages 303-311

[7] Hunter, C. (1977), *The Collapse of Unstable Isothermal Spheres*, Astrophysical Journal, Volume 218, Pages 834-845

[8] Larson, R.B. (1969), *Numerical Calculations of the Dynamics of a Collapsing Proto-star*, Monthly Notices of the Royal Astronomical Society, Volume 145, Pages 271-295

[9] Mellema, G., et al. (1991), *Hydrodynamic Models of Aspherical Planetary Nebulae*, Astronomy & Astrophysics, Volume 252, Pages 718-732

[10] Misner, C.W., Thorne, K.S. & Wheeler, J.A. (1973), *Gravitation*, Freeman & Co., New York ISBN 0-716-70344-0

[11] Paardekooper, S.J., (2002), *Planets in Disks, a New Method for Hydrodynamic Disc Simulations*, Master thesis, Sterrewacht Leiden, The Netherlands

[12] Press, W.H., et al. (2002), *Numerical Recipes in C*, Second Edition, Cambridge University Press, ISBN 0-521-43108-5

[13] Roe, P.L. (1986), *Characteristic-based Schemes for the Euler Equations*, Annual Review of Fluid Mechanics, Volume 18, Pages 337-365

[14] Shu, F.H. (1977), *Self-similar Collapse of Isothermal Spheres and Star Formation*, Astrophysical Journal, Volume 214, Pages 488-497

[15] Shu, F.H. (1992), *Gas Dynamics*, The Physics of Astrophysics, Volume II, University Science Books, ISBN 0-935702-65-2